Hybrid-Monte-Carlo Simulations of strongly interacting fermions at finite density on the hexagonal lattice

JUSTUS-LIEBIG-
UNIVERSITÄT
GIESSEN

Institut für Theoretische Physik

Zur Erlangung des Grades
eines Doktors der Naturwissenschaften
vorgelegte Dissertation von

M.Sc. Michael Körner

Referent: Prof. Dr. Lorenz von Smekal
Koreferent: Prof. Dr. Christian Fischer

Selbstständigkeitserklärung

Ich erkläre: Ich habe die vorgelegte Dissertation selbstständig und ohne unerlaubte fremde Hilfe und nur mit den Hilfen angefertigt, die ich in der Dissertation angegeben habe. Alle Textstellen, die wörtlich oder sinngemäß aus veröffentlichten Schriften entnommen sind, und alle Angaben, die auf mündlichen Auskünften beruhen, sind als solche kenntlich gemacht. Ich stimme einer evtl. Überprüfung meiner Dissertation durch eine Antiplagiat-Software zu. Bei den von mir durchgeführten und in der Dissertation erwähnten Untersuchungen habe ich die Grundsätze guter wissenschaftlicher Praxis, wie sie in der "Satzung der Justus-Liebig-Universität Gießen zur Sicherung guter wissenschaftlicher Praxis" niedergelegt sind, eingehalten.

Gießen, den 25.06.2020

_____

(Michael Körner)

Zusammenfassung

In dieser Arbeit werden zwei verschiedene Strategien zum Umgang mit dem Vorzeichenproblem im Kontext von Hybrid-Monte-Carlo Simulationen des hexagonalen Graphengitters behandelt. Der erste Ansatz besteht darin, eine vorzeichenproblemfreie Theorie zu simulieren, indem die Teilchen-Loch Symmetrie der Bandstruktur von Graphen ausgenutzt wird. Im Speziellen verwenden ein spinabhängiges chemisches Potential, das aus genannten Gründen im nicht wechselwirkenden Fall identisch mit einem tatsächlichen Ladungsträgerpotential ist. In diesem Teil der Arbeit modellieren wir die Vielteilchenwechselwirkung durch ein langreichweitiges Coulomb Potential welches Abschirmungseffekte der σ-Bandelektronen berücksichtigt und untersuchen dessen Einfluss auf die Bandstruktur. Insbesondere konzentrieren wir uns auf die Veränderung der Bandstruktur und das Verhalten des topologischen Lifshitz Übergangs, welcher an der van Hove Singularität verortet ist. Hierbei konnten wir Hinweise darauf finden, dass die Bandbreite durch Vielteilchenwechselwirkungen verringert wird, was mit experimentellen Beobachtungen aus der winkelaufgelösten Photoemissionsspektroskopie übereinstimmt. Darüber hinaus weisen unsere Ergebnisse darauf hin, dass der Lifshitz Übergang durch die Vielteilchenwechselwirkung tendenziell zu einem echten Quantenphasenübergang wird. Im zweiten Teil der Arbeit behandeln wir einen Ansatz welcher direkt mit dem chemischen Potential arbeitet. Hierbei wenden wir die Linear-Logarithmic-Relaxation Methode an, um eine verallgemeinerte Zustandsdichte zu berechnen und nutzen diese für eine Rekonstruktion der Teilchendichte. Wir vergleichen diesen Ansatz mit reinem Brute-Force-Reweithing und zeigen, dass sich der relative Vorteil der Methode mit zunehmender Wechselwirkungsstärke verbessert. Der Einfachheit halber verwenden in diesem Teil das Hubbard Modell. Abschließend diskutieren wir beide Varianten und geben einen Überblick über mögliche weitere Untersuchungen oder denkbare Verbesserungen der Methoden.

Abstract

In this work we report on two different strategies to deal with the fermion sign problem in context of Hybrid-Monte-Carlo simulations on the hexagonal graphene lattice. The first approach is to simulate a theory, which have no sign problem, by taking advantage of the particle-hole symmetry of the band structure of graphene and applying a spin dependent chemical potential which is in the non interacting case equal to charge carrier density. There we take a realistic screened Coulomb potential into account and investigate the influence of it on the band structure. In particular, we focus on the deviation on the band structure and the behavior of topological Lifshitz transition taking place at the van Hove singularity. Within this part we find evidence that the bandwidth is reduced by many-body interactions, which is in-line with experimental observations from angle resolved photoemission spectroscopy. Furthermore, our results indicate that the Lifshitz transition tend to become a true quantum phase transition in presence of interactions. In the second approach, we are dealing with an charge carrier chemical potential directly. Here, we use the Linear-Logarithmic-Relaxation method to compute a generalized density of states and use this as an input for a reconstruction of the particle density. We compare this approach with pure brute-force reweighting and show that the relative advantage of the method grows with increasing interaction strength. For the sake of simplicity we use the Hubbard model with only on-site interactions in this case. Finally, we discuss both variants and give an overview of possible further investigations or thinkable improvements of the methods.

Contents

The results, produced by the author of this thesis, which are presented in this work are already partially published in [1–5].

1. Introduction

The 2-dimensional allotrope of carbon, graphene, is a basic ingredient for carbon structures (Fig. 1.1) and has become more and more prominent since the publications of Novoselov and Geim on their experimental results on the electronic properties of single layer graphite in 2004. These studies opened an experimental approach to physics of two dimensional solid states and thus to a new world of physics [6]. Although small graphene flakes were already realized in experiments in the 1960s by Boehm et al. [7] hardly anyone really paid attention to it because 2-dimensional crystals supposedly should not exist due to several theoretical works of Landau [8], Peierls [9] and later Mermin [10]. In recent decades on the one hand the theory was reconciled with experiment by showing that a wrinkling in the third dimension suppresses thermal vibrations by an increase in elastic energy which lead to an intrinsic stability of mono-layer structures. On the other hand, the award of the Nobel Prize to Novoselov and Geim in 2010 brought the topic of two dimensional materials and their unique properties further into the public eye and the focus of further research efforts [11]. Meanwhile there are numerous studies on properties, manufacturing processes and possible applications for various 2d-structures for example graphene, silicene or hexagonal boron nitride. Thus we can only give a short and brief overview here. Detailed reviews of experimental work as well as fabrication strategies can be found in [12–14] and theory in [15, 16]. Focusing on graphene, it was found experimentally to be a conductor [17–19], which can be explained by the screening effects of the lower σ-band electrons and the carrier material. Nevertheless the predicted coupling for shifting graphene into an insulating phase lies slightly above the value of suspended graphene, in other words a small increase of electron interaction is needed to realize a gap opening [20–24]. It should also be mentioned that due to phononic dispersion properties, graphene is a very good thermal conductor, too [25–27]. The mechanical properties are also quite unique, mentioning for example the very high modulus of elasticity [28]. Furthermore, the Quantum Hall effect were realized at room temperature in graphene [29] as well as superconductivity in Ca-doped graphene structures [30], to mention only a few more interesting effects found. The possible applications range from semiconductor components, water- and air-purification, energy storage systems, coatings for mechanical purposes to biomedical applications, which is not meant to be a complete list [31].

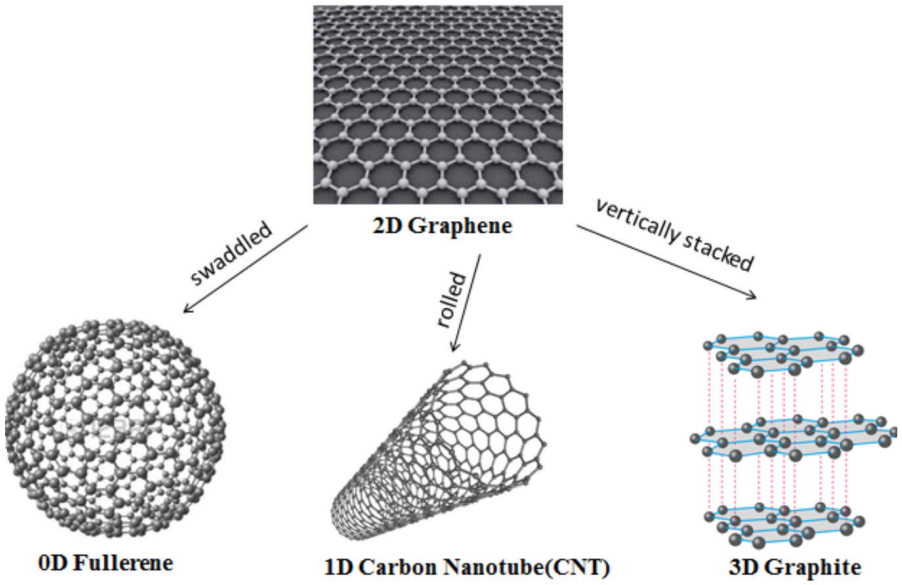

Figure 1.1.: Overview of Carbon structures, where graphene is seen as the basis of fullerenes (0d), nanotubes (1d) and graphite (3d). Taken from [32]

Besides the manifold fields of application, 2d-hexagonal structures also offer a wide range of possible theoretical questions. This is mainly due to the band structure, which was first derived by Wallace in 1946 [33]. In this study was shown that the valence band touches the conductance band at two independent points K and K^* in the first Brillouin zone. At these so-called Dirac points the valence band changes linearly into the conduction band and by this quasi-particles on the graphene lattice can be described by the relativistic Dirac equation around these K-points. Thus the charge carriers on the hexagonal lattice act like Dirac fermions with an effective speed of light defined by the Fermi velocity and experimentally determined as $v_F \approx c/300$ for the graphene lattice [15, 34]. This leads to the fact that the system is strongly coupled, because the resulting fine structure constant which indicates the ratio of interaction strength to kinetic energy becomes $\alpha_{eff} = \alpha\, c/v_f \approx 2.2$. Furthermore, the fact that the Dirac equation is used to describe the charge carriers in the so-called Dirac cone offers the possibility to use graphene as a sample for QED in 2+1 dimensions [35]. In the context of this analogy several phenomena such as electronic chirality, Berry phases, Quantum Hall effects and corresponding phases or the Klein paradox [15, 16, 35–40] have been studied. Graphene was also studied away from the Dirac cone where an extended van Hove singularity (eVHS) was found experimentally [41] and d-wave superconducting phases [42–45], in context of the van Hove scenario [46] have been proposed.

For theoretical investigations apart from single-particle effects, non-pertubative methods are needed due to the strong effective coupling. Here, functional methods are a common way to approach problems. Work with Dyson-Schwinger equations [24,47–51] and functional renormalization group [45, 52–54] should be mentioned here. Another approach are Quantum Monte Carlo methods which are widely used for ab initio simulations of strongly correlated systems. So hexagonal systems have been studied via the in solid state physics frequently used BSS-Monte-Carlo technique [55, 56] within the standard and extended Hubbard model [22, 23, 57]. However, the Hybrid-Monte-Carlo (HMC) method, which is more popular in high energy physics, became more important in the graphene research in recent years [4, 58–60]. This is mainly because HMC's update method offers the advantage of simulating more complex interaction structures and scales better with increasing volume [60]. Today it is possible to simulate lattices up to 102x102 unit cells with 64 time-slices, using advanced solvers and integrators [61]. Unfortunately Monte-Carlo techniques are restricted to systems with vanishing chemical potential due to the fermion sign problem [62] which can be seen as noise in which the signal is lost. Thus this problem excludes simulations in fermionic systems away from half filling, unless the complex parts of the measure cancel exactly due to anti-unitary symmetry as it would be the case with a spin-dependent potential. To circumvent this problem several methods was proposed in the past which were only partially successful. A general and applicable procedure to solve the problem in polynomial time is not yet in sight. Furthermore, it is unclear whether such a procedure exists at all since there is evidence that this problem is NP-hard [63]. A more recent approach to deal with the problem is the Linear-Logarithmic-Relaxation (LLR) method, proposed by Langfeld, Lucini and Rago in 2012 [64], which is based on Wang-Landau methods [65] and provides the possibility to measure an observable with exponential error suppression and brought promising results in different exemplary models [66–72].

In this work we use the Hybrid-Monte-Carlo framework to investigate the implications of a spin-dependent chemical potential with long-range interactions on the one hand and combine the LLR framework with HMC and data evaluation via canonical ensembles in order to benchmark the gain from this method in comparison to brute-force reweighting on the other hand. Hereby we use for the sake of simplicity the on-site Hubbard model at finite charge density which has also a sign problem. We first give a theoretical introduction in chapter 2, where the theoretical basics, which we need for the later simulations and results part, are presented. First the hexagonal graphene lattice and the tight-binding formulation is presented and within this single-particle theory we derive some approximations which will be used as a baseline for comparison with HMC results later. Additionally, we give an introduction in topological transitions on the hexagonal lattice and the used observable for spin-dependent

chemical potential. After that we show the details of our path integral formulation used for HMC and briefly review the used potentials. Then we introduce the LLR method and provide the evaluation procedure for obtaining the particle density. In chapter 3 we briefly review the HMC method and discuss details of the application on the hexagonal lattice. Then we discuss the fermion sign problem before we show how the HMC is used for studying the spin-dependent system and how HMC is combined with the LLR algorithm. After that, we first show in chapter 4 the results from spin-dependent chemical potential with respect to parameters which come up with the usage of HMC, like lattice discretization and also discuss the influence of physical parameters. In the end we focus on the behavior of Lifshitz transition in an interacting system and summarize the obtained results. Afterwards, we will present the results for the LLR part of the work in chapter 5 and also discuss the influences of the corresponding parameters. Finally, we will make a comparison with brute-force reweighting and summarize the results of the chapter. The whole work is then finally concluded in chapter 6, where also an outlook of interesting questions further investigations is given.

2. Theory

In the following chapter we first present the particularities of a 2d-hexagonal system and give a brief introduction in the used theoretical models. Here we begin with the definition of the hexagonal lattice and the tight-binding formalism where we focus also on the topological Lifshitz transition. This is followed by the introduction of the path integral formulation used for applying the HMC algorithm. Within this section we briefly review two different potentials used in this work. Finally we give an overview of the LLR method and how we use it in our reconstructing scheme for the particle density.

2.1. Hexagonal lattice

In order to generate a hexagonal lattice one needs two triangular sub-lattices A and B which are shifted by a vector $\vec{c}$

$$\vec{a} = a \cdot \begin{pmatrix} \sqrt{3} \\ 0 \end{pmatrix} \qquad \vec{b} = \frac{a}{2} \cdot \begin{pmatrix} \sqrt{3} \\ 3 \end{pmatrix} \qquad \vec{c} = \begin{pmatrix} 0 \\ a \end{pmatrix} \tag{2.1}$$

with $a = 1,42\,\mathring{A}$ as lattice constant for graphene. All the lattice points are then reachable by linear combination of

$$\vec{R}_A = n_1\,\vec{a} + n_2\,\vec{b} \qquad \vec{R}_B = n_1\,\vec{a} + n_2\,\vec{b} + \vec{c} \tag{2.2}$$

with n_1 respectively $n_2 \in \mathbb{Z}$, see fig. 2.1.
The area of the unit cell for graphene lattice thus is $A_c = \frac{3}{2}\sqrt{3}a^2$. [15, 73] We use Born-von-Karman boundary conditions for all finite lattices in this work.

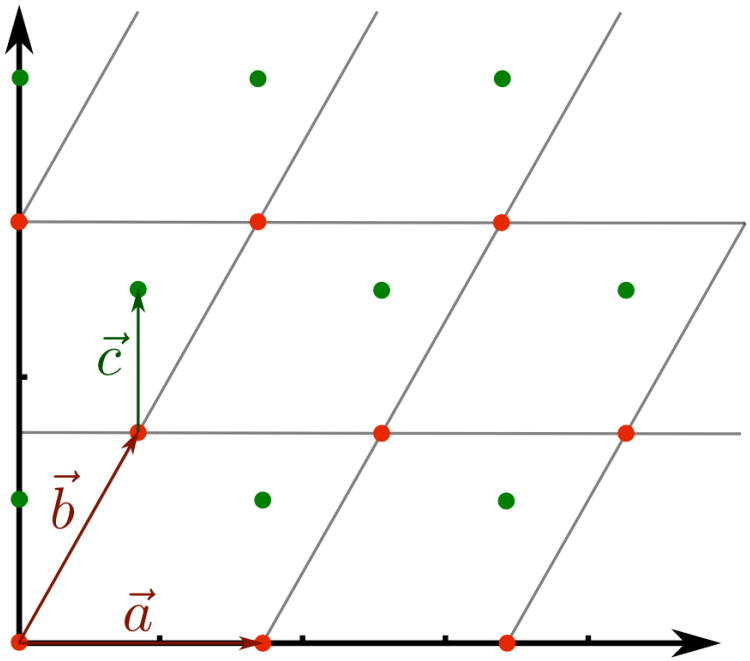

Figure 2.1.: Graphene lattice with marked unit cells (gray) and also sub-lattice A (red) and B (green).

2.2. Single-particle description

The tight-binding description of the hexagonal lattice, first derived by Wallace already in 1947 [33], shows the typical band structure which has produced much interest in graphene over last decades. One finds, in the simple nearest-neighbor formulation for example the linear dispersion around the K-Points which leads to massless electronic excitations in the so-called Dirac cone area. When the contributions of the second and third orders are also taken into account one gets a very good agreement with ab-initio calculations like self consistent density functional methods [74]. In the following, the results of these calculations are briefly presented and necessary approximations with focus on HMC observables used in this work were outlined.

2.2.1. Electronic structure from Tight-Binding model

Carbon atoms arranged in a graphene sheet have three electrons in sp^2-hybrid orbitals which form a covalent σ-bond system. The remaining valence electron is located in a $2p_z$-orbital perpendicular to the 2d sheet and builds a π-binding system above and below the lattice [15]. Since hexagonal lattice is build out of two sub-lattices A and B (see. 2.1), one finds two π-electrons per unit cell. In order to derive the single-particle

band structure we start with a Bloch Ansatz

$$\psi_{\vec{k}}(\vec{r}) = \frac{1}{\sqrt{N}} \sum_n e^{i\vec{k}\vec{R}_n} \left(c_1 \, \phi_A(\vec{r} - \vec{R}_n) + c_2 \, \phi_B(\vec{r} - \vec{R}_n) \right) \tag{2.3}$$

where N denotes the number of lattice points. Assume both wave functions are strongly localized so that

$$\langle \phi_A | \phi_B \rangle = 0 \tag{2.4}$$

holds. By projecting stationary Schrödinger equation to each wave function we find for sub-lattice A

$$\begin{aligned} \langle \phi_A | H | \psi_{\vec{k}} \rangle = \frac{1}{N} \Bigg(& c_1 \int dr^2 \phi_A^*(\vec{r}) H \phi_A(\vec{r}) \\ & + c_2 \int dr^2 \phi_A^*(\vec{r}) H \sum_{R_n \in n.N.} e^{i\vec{k}\vec{R}_n} \phi_B(\vec{r} - \vec{R}_n) \Bigg) \end{aligned} \tag{2.5}$$

when only nearest-neighbor interactions are taken. By putting the corresponding lattice vectors in the eq. 2.5 we find

$$\begin{aligned} \langle \phi_A | H | \psi_{\vec{k}} \rangle = \frac{1}{N} \Bigg[& c_1 \epsilon + c_2 \Bigg(e^{iak_y} \int dr^2 \phi_A^*(\vec{r}) H \phi_B(\vec{r} - \vec{v}_1) \\ & + e^{-i(\frac{\sqrt{3}a}{2} k_x + \frac{a}{2} k_y)} \int dr^2 \phi_A^*(\vec{r}) H \phi_B(\vec{r} - \vec{v}_2) \\ & + e^{i(\frac{\sqrt{3}a}{2} k_x - \frac{a}{2} k_y)} \int dr^2 \phi_A^*(\vec{r}) H \phi_B(\vec{r} - \vec{v}_3) \Bigg) \Bigg] \end{aligned} \tag{2.6}$$

with ϵ as self energy, which can be set to zero in the next step. This means that we shift the zero energy value to half filling of the π-bands. The remaining integrals can be approximated by a constant κ, the so-called hopping parameter, due to the equal distance of nearest neighbors.

$$\int dr^2 \phi_A^*(\vec{r}) H \phi_B(\vec{r} - \vec{v}_i) = \kappa \quad \mathrm{i} \in \{1, 2, 3\} \tag{2.7}$$

Applying this procedure analogously to the sub-lattice B, one obtains the following system of equations:

$$\begin{pmatrix} -E & \kappa \left(e^{i\vec{k}\vec{v}_{1,B}} + e^{i\vec{k}\vec{v}_{2,B}} + e^{i\vec{k}\vec{v}_{3,B}} \right) \\ \kappa \left(e^{i\vec{k}\vec{v}_{1,A}} + e^{i\vec{k}\vec{v}_{2,A}} + e^{i\vec{k}\vec{v}_{3,A}} \right) & -E \end{pmatrix} \cdot \begin{pmatrix} c_1 \\ c_2 \end{pmatrix} = 0 \tag{2.8}$$

By taking the determinant of the matrix and some simple transformations we can write down the tight-binding band structure in nearest-neighbor approximation as

follows

$$E(\vec{k}_x, \vec{k}_y) = \pm\kappa\sqrt{3 + 4\cos\left(\frac{\sqrt{3}a}{2}k_x\right)\cos\left(\frac{3a}{2}k_y\right) + 2\cos\left(\sqrt{3}ak_x\right)} \tag{2.9}$$

with $\kappa \approx 2,7\,eV$ (see [15]).

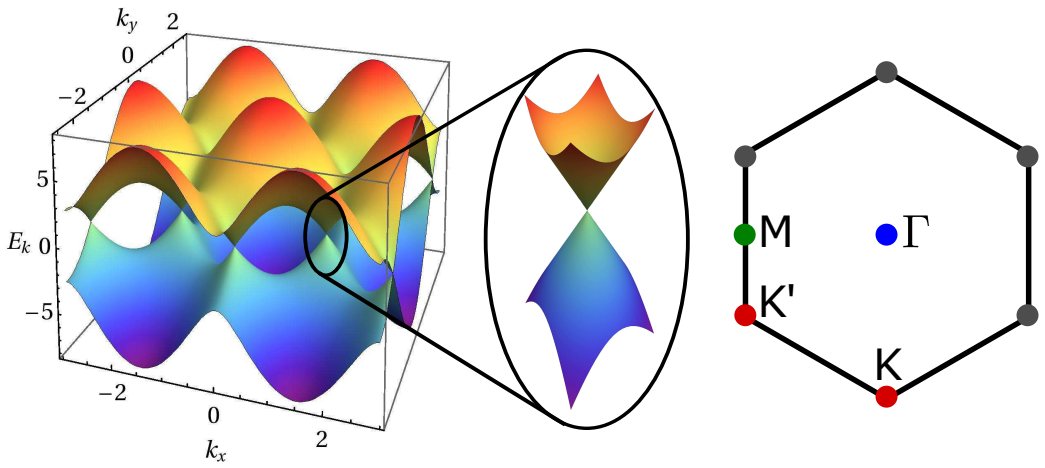

Figure 2.2.: Left: Valence (blue) and conductance (orange) band in nearest-neighbor tight-binding description with focus on the Dirac cones. Right: Schematic presentation of the special points in the first Brillouin zone. (taken from [2])

In Figure 2.2 one can see eq. 2.9 plotted over the first Brillouin zone. This illustrates that the band structure in this approximation has a particle-hole symmetry and thus by shifting the Fermi energy through a chemical potential μ to higher or lower values one will generate the same Fermi surface, which is a line in 2d-systems. Through summation of all the possible states per unit cell at one corresponding energy we find the density of states (DOS) of the system which reflects also the symmetry of the bands (see fig. 2.3). For the hexagonal lattice this was done first by Hobson and Nierenberg in 1952. They showed that the density of states per unit cell $\rho(E)$ can be written as:

$$\rho(E) = \frac{4\,|E|}{\pi^2\,\kappa^2}\frac{1}{\sqrt{Z_0}}\mathbf{F}\left(\frac{\pi}{2}, \sqrt{\frac{Z_1}{Z_0}}\right) \tag{2.10}$$

with

$$Z_0 = \left(1 + \left|\frac{E}{\kappa}\right|\right)^2 - \frac{\left[\left(\frac{E}{\kappa}\right)^2 - 1\right]^2}{4} \quad \text{and} \quad Z_1 = 4\left|\frac{E}{\kappa}\right| \qquad \text{for} \qquad |E| \leq \kappa \tag{2.11}$$

and

$$Z_0 = 4\left|\frac{E}{\kappa}\right| \quad \text{and} \quad Z_1 = \left(1 + \left|\frac{E}{\kappa}\right|\right)^2 - \frac{\left[\left(\frac{E}{\kappa}\right)^2 - 1\right]^2}{4} \qquad \text{for} \qquad \kappa \leq |E| \leq 3\kappa \tag{2.12}$$

where $\mathbf{F}(\pi/2, x)$ means the complete elliptic integral of the first kind [75].

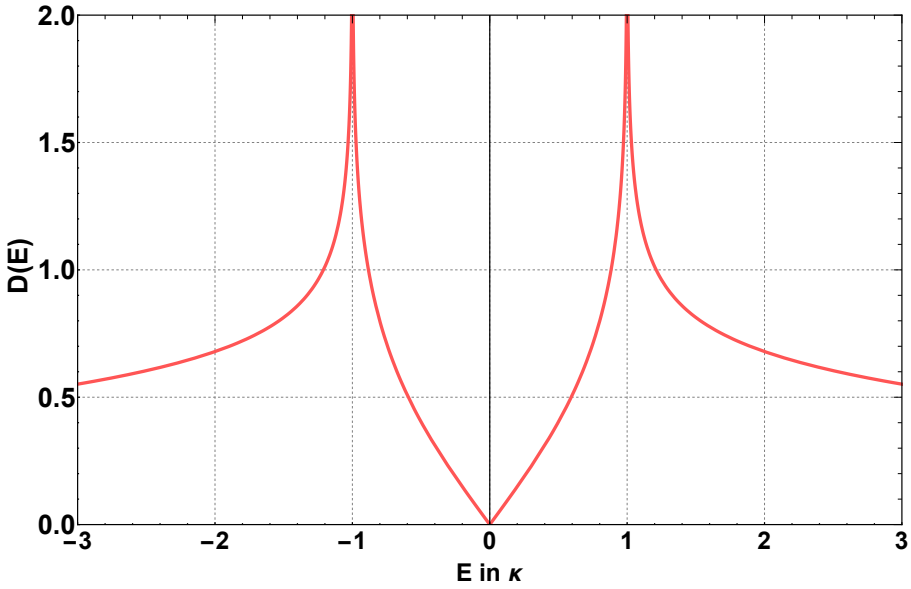

Figure 2.3.: Density of states of the nearest-neighbor tight-binding model of the hexagonal lattice

2.2.2. Lifshitz transition and Thomas-Fermi Susceptibility

Transitions of topology in the Fermi surface are called Lifshitz transitions and were first described by I.M. Lifshitz in the 1960s in the context of zero temperature behavior of electrons in metals [76]. These electronic topological transitions always occur when the Fermi energy crosses an extremum of the dispersion function $E(\vec{k})$. So it can be shown that depending on the effective dimensionality d of the system, $d+1$ different transition types that can be found. In two dimensions, depending on the type of extremum, only void formation (minimum point), void disappearance (maximum point) or neck disruption (saddle point) transitions occur. Obviously, these transitions have a close connection to van Hove singularities (VHS), since they are accompanied by a singularity in the density of states (which is the definition of a VHS) at the transition point. This connection is the also the reason why Lifshitz

transitions has received more and more attention in the field of high temperature superconductivity in cuprates [77–79], thin films [80,81] as well as 2-dimensional carbon structures [82, 83]. So the so-called "van Hove scenario" reflects that in most high-T_c superconducting cuprates a van Hove singularity can be found close to the Fermi level. However, this topic is still subject of active research and a final answer to high-T_c Superconductivity theory is still missing. For a detailed review of electronic topological transitions see [84].

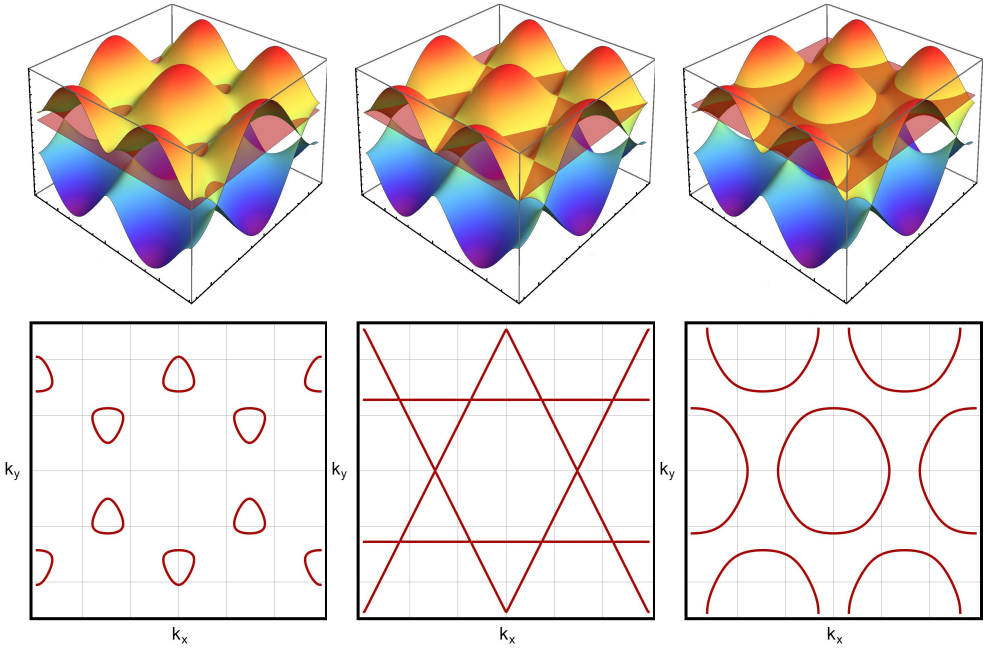

Figure 2.4.: Illustration of Lifshitz transition in nearest-neighbor tight-binding band structure of graphene. *Left:* Fermi level below VHS, *Middle:* Fermi level at VHS *Right:* Fermi level above VHS. (taken from [2])

As already indicated in the tight-binding band structure of graphene shown in sec. 2.2.1 a van Hove singularity is located at the M-point (see Fig. 2.4) and therefore also a neck disrupting Lifshitz transition. The Fermi surface in the Dirac cone region is parted in deformed triangles which are located around the K-points, when the Fermi level reaches the VHS these triangles connect each other and build a system of lines which split up again in the region above the VHS to one circle around the Γ-point.

More details about the transition can be obtained by expanding the energy dispersion around the VHS. In appropriate coordinates $E(\vec{k})$ can be written as

$$E(\vec{k})\Big|_{\mu=\kappa} = \frac{k_x^2}{2} - \frac{k_y^2}{2} + \kappa \tag{2.13}$$

in the vicinity of the VHS and by putting in the definition of density of states

$$\rho(\mu) = g_\sigma A_c \int_{\mathrm{BZ}} \frac{d^2k}{(2\pi)^2}\, \delta(E(\vec{k}) - |\mu|) \tag{2.14}$$

with $g_\sigma = 2$ here for spin degeneracy, a logarithmic divergence

$$\rho_{VHS}(z) = -\frac{3g_\sigma}{2\pi^2\kappa} \ln|z| \tag{2.15}$$

with reduced Fermi energy parameter $z = (|\mu| - \kappa)/\kappa$, at the VHS can be obtained (cf. [84], [3]). This topological transition in the pure tight-binding model and the corresponding logarithmic divergence were also found experimentally by measuring the resonance spectra of microwaves in superconducting microwave billiard in the form that it can be used as an analog system of 2d-hexagonal lattice [85]. There it was pointed out that the topological transition separates the relativistic Dirac cone area from the non-relativistic Fermi liquid regime above the VHS. Within this study it was also shown, that the Thomas-Fermi susceptibility $\chi(\epsilon)$, which is the static limit of no momentum transfer of the Lindhard screening function $\Pi(\omega, \vec{p}, \mu, T)$ shows also logarithmic divergences, since it is in the limit of $T = 0$ equal to the DOS.
In order to illustrate the connections between Lifshitz transition, DOS and the Thomas-Fermi susceptibility in the hexagonal carbon system we start as mentioned above with the particle-hole polarization function $\Pi(\omega, \vec{p}, \mu, T)$ with excitation frequency ω, momentum $\vec{p}$, chemical potential μ (with $\mu = 0$ at half filling) and temperature T:

$$\begin{aligned}\Pi(\omega, \vec{p}; \mu, T) = &- g_\sigma \int_{\mathrm{BZ}} \frac{d^2k}{(2\pi)^2} \sum_{s,s'=\pm1} \left(1 + ss' \frac{\mathrm{Re}\left(\phi^*_{\vec{k}}\, \phi_{\vec{k}+\vec{p}}\right)}{|\phi_{\vec{k}}||\phi_{\vec{k}+\vec{p}}|}\right) \\ &\times \frac{f(s'\epsilon_{\vec{k}+\vec{p}} - \mu) - f(s\epsilon_{\vec{k}} - \mu)}{s'\epsilon_{\vec{k}+\vec{p}} - s\epsilon_{\vec{k}} - \omega - i\epsilon}\end{aligned}$$

where the terms $s' = s$ describes intraband particle-hole excitations, whereas $s' = -s$ terms stands for interband excitations, $\phi_{\vec{k}} = \sum_n e^{i\vec{k}\vec{\delta}_n}$ denotes the structure factor with nearest-neighbor vectors $\vec{\delta}_n$, $n = 1, 2, 3$, single-particle energies are $\epsilon_{\vec{k}} = \kappa|\phi_{\vec{k}}|$ and the Fermi-Dirac distribution $f(x) = 1/(e^{x/T} + 1)$. We then get the Thomas-Fermi susceptibility, normalized per unit cell of area $A_c = 3^{\frac{3}{2}}a^2/2$, by taking the static limit

of no momentum transfer

$$\chi_\mu = A_c \lim_{\vec{p}\to 0} \lim_{\vec{\omega}\to 0} \Pi(\omega, \vec{p}, \mu, T) \tag{2.16}$$

and thus only taking intraband excitations into account. After short calculation (see Appendix A) we finally find

$$\chi(\mu) = \frac{g_\sigma A_c}{4T} \int_{1.BZ} \frac{d^2k}{4\pi^2} \left[\operatorname{sech}^2\left(\frac{\mu - \epsilon_{\vec{k}}}{2T}\right) + \operatorname{sech}^2\left(\frac{\mu + \epsilon_{\vec{k}}}{2T}\right) \right] \tag{2.17}$$

which is equal to the density of states per unit cell $\rho(\epsilon)$ in the $T = 0$ limit for a Fermi energy $\epsilon = \mu$:

$$\lim_{T\to 0} \chi(\mu) = g_\sigma A_c \int_{\mathrm{BZ}} \frac{d^2k}{(2\pi)^2} \delta(\epsilon_{\vec{k}} - |\mu|) \equiv \rho(\mu) \tag{2.18}$$

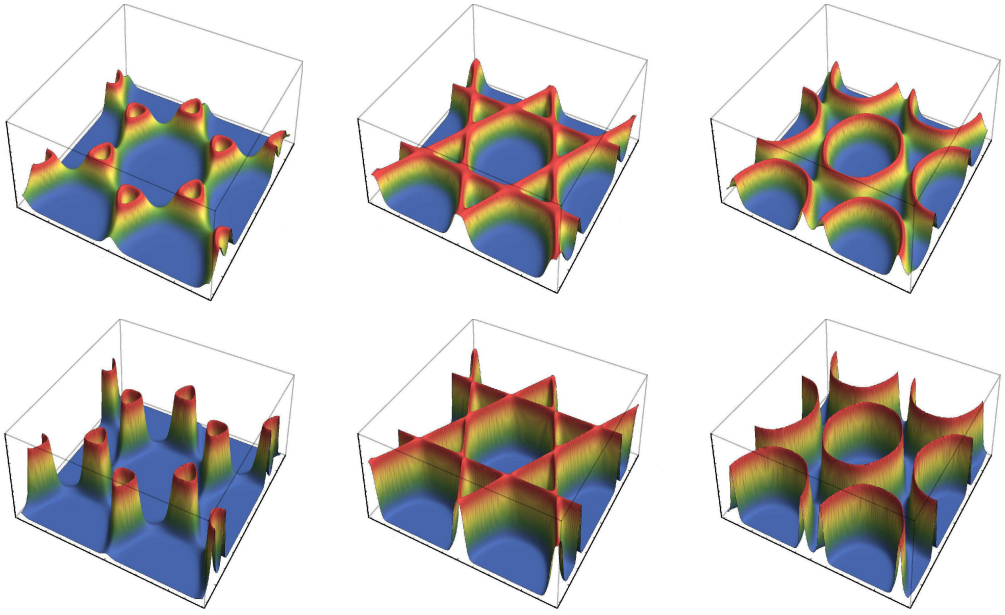

Figure 2.5.: Integrand of eq. 2.17 for μ below *(right)* \at*(middle)* \above*(left)* the van Hove singularity for $T = \frac{1}{2k_B}$ (*upper figures*) and $T = \frac{1}{4k_B}$ (*lower figures*) (taken from [2])

By focusing on the integrand of eq. 2.17 and by varying temperature in addition to μ according to Fig. 2.4 we see that the topological transition takes also place in the susceptibility but the sharp Fermi lines are smeared out. This broadening reveals the possible excitation ranges induced by temperature effects. In Fig. 2.5 the integrand is plotted for two different temperature values showing that the width of

the distribution around the $T = 0$ lines becomes smaller when the temperature is lowered and finally turn into a delta distribution when $T \to 0$ which makes the figure equal to the lower row in Fig. 2.4. Thus the transition takes place at the VHS even for finite temperatures and it is necessary to have a formulation for the susceptibility at the saddle points. The relation should contain the typical logarithmic divergences for a Lifshitz transition. We find

$$\chi_{\max} = \frac{3g_\sigma}{2\pi^2\kappa}\Big\{ -\ln\left(\pi T/\kappa\right) + \gamma_E + 3\ln 2 + \mathcal{O}(T)\Big\} \tag{2.19}$$

where γ_E is the Euler-Mascheroni constant. This approximation was derived in detail for the DOS in [85] and for Thomas-Fermi susceptibility in [2] by inserting unity in the form of an integral over a Delta distribution in eq. 2.17 and then using the explicit representation of the DOS from [75] and finally realize a Taylor expansion of the arising terms (see Appendix A).

Besides the temperature scaling, it is of interest with a view to simulations, to understand the interplay between volume and temperature dependence of the susceptibility. For this we use again eq. 2.17 but the integral becomes a sum over the allowed momentum states which fulfill the Laue equation $e^{i\vec{k}\vec{R}} = 1$. After short calculation we end up with

$$\chi(\mu) = \frac{g_\sigma}{4TN_c}\sum_{n,m}\left[\operatorname{sech}^2\left(\frac{\epsilon_{mn}-\mu}{2T}\right) + \operatorname{sech}^2\left(\frac{\epsilon_{mn}+\mu}{2T}\right)\right] \tag{2.20}$$

where $N_c = N_x N_y$ denotes the number of unit cells of the finite hexagonal lattice and ϵ_{mn} means eq. 2.9 evaluated at the points allowed by the Laue equation. Now we carry out eq. 2.20 numerically for different lattice sizes and temperatures and on the one hand verify the approximation in eq. 2.19 numerically and on the other hand show that square lattices with even or odd number of unit cells in one direction behave in fundamentally different manner. The even lattices decrease in the peak height with increasing volume, since the M-point is located in the center of the Brillouin zone and in finite systems the singularity contributes in every lattice size and with increasing N_c only values which are nearly zero are added. In the odd case the inverse effect takes place, meaning the singularity is only reached in the finite volume limit. Figure 2.7 shows this effect for different inverse temperatures $\beta = 1/T$. The horizontal lines show the predictions from eq 2.19 and the data points were generated by the sum formula (eq. 2.20). We find a good agreement between the two formulations in the infinite volume limit. The deviations at low β come from the linear order contribution in eq. 2.19.

Furthermore, eq. 2.20 allows us to study the finite temperature and volume behavior of the Thomas-Fermi susceptibility not only at the van Hove point but also in the whole possible range of chemical potential μ. These considerations serve as a

benchmark for comparisons with the results from HMC simulations with finite interaction strength. Since the tight-binding band structure is symmetric around half filling $\mu = 0$ we only consider the conductance band from here on. Figure 2.6 shows the temperature dependence of $\chi(\mu)$ for the whole band (red lines) which goes from the Dirac points ($\mu = 0$) up to the Γ-point ($\mu = 3\kappa$) and the corresponding density of states (blue line). Hereby, the lattice size was always chosen large enough to avoid finite volume effects. As expected, the finite temperature smears out the typical shape of the DOS but still contains the already mentioned general structure. The volume dependence of $\chi(\mu)$ for an inverse temperature $\beta = 10.8\,\kappa^{-1}$ is shown in Figure 2.6 as well. On the one hand we can show there, that the susceptibility for small lattices is dominated by volume effects and on the other hand we obtain a phase shift in the leading wave structure between even and odd lattices.

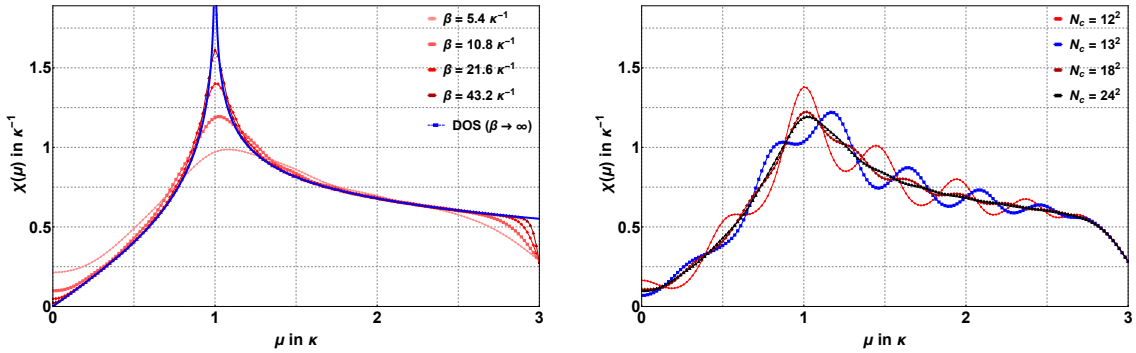

Figure 2.6.: Temperature (*left*) and Volume (*right*) behavior of $\chi(\mu)$ for hexagonal lattices in finite volume limit. The red lines show data generated with eq. 2.20 in comparison with the density of states per unit cell in blue.

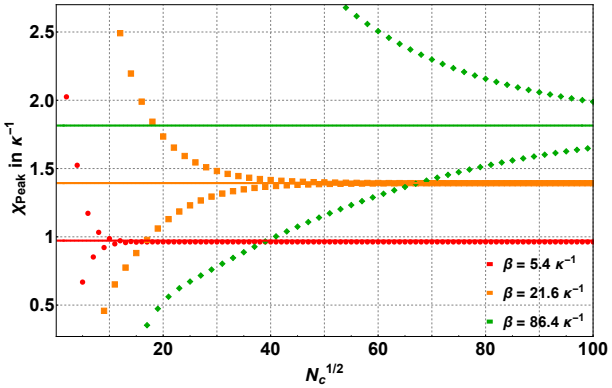

Figure 2.7.: Finite-size scaling of χ_{max} for different temperatures. The horizontal lines are the predictions calculated with eq 2.19. The data points were generated with eq. 2.20.

2.3. Interacting system

In this section we present our formulation of the standard path integral representation which is needed for HMC simulations and highlight important details within our formulation. After that we briefly review the Hubbard model which we use for applying LLR algorithm on our HMC framework and discuss the more realistic partially screened long-range potential which is used for the investigations around the spin-dependent chemical potential.

2.3.1. Path integral formulation

We start with the tight-binding Hamiltonian extended by an interaction potential V_{xy} and a chemical potential μ. More details about shape and kind of the used potentials can be found in section 2.3.2.

$$\begin{aligned} H =& H_{tb} + H_{coul} + H_{ms} + H_{\mu} \\ =& -\kappa \sum_{\langle x,y\rangle,\sigma} \left(\hat{c}^{\dagger}_{y,\sigma} \hat{c}_{x,\sigma} + \text{h.c.} \right) + \frac{1}{2} \sum_{x,y} \hat{q}_x V_{xy} \hat{q}_y \\ &+ m_s \sum_x \hat{c}^{\dagger}_{x,1} \hat{c}_{x,1} + \hat{c}_{x,-1} \hat{c}^{\dagger}_{x,-1} - \mu \sum_{x,\sigma} \hat{c}^{\dagger}_{x,\sigma} \hat{c}_{x,\sigma} \end{aligned} \tag{2.21}$$

with $q_x = c^{\dagger}_{x,1} c_{x,1} - c_{x,-1} c^{\dagger}_{x,-1}$ as the charge operator, κ is the hopping parameter, $\langle x, y\rangle$ that means we sum only over nearest-neighbor sites and $\sigma = \pm 1$ labels spin along some quantization axis. The mass m_s of the term H_{ms} introduces an explicit sub-lattice staggering, which is needed to cancel zero modes out of the fermion matrix and by that make sure that no ergodicity problems in HMC simulations arise. Details of H_{ms} are discussed in chapter 3.1.2 and 4.1.1 in more detail.
We now construct the partition function of the grand canonical ensemble in path integral representation in order to have a formulation which is usable for Hybrid-Monte-Carlo simulations. For the hexagonal lattice this was first proposed by Brower et al. [86] and in more detail outlined by Smith and von Smekal in [20]. The basics of the method can be found in [87] as well as in [88]. The following derivation is based on the mentioned publications and textbooks (for more detail see there) and follow the common procedure of rewriting a partition function into a path integral representation by introducing appropriate base and approximate the resulting matrix element of the evolution operator by introducing finite time slices with a discretization parameter δ, taking then only the normal ordered part of the operator and accepting therefore an error of the order $\mathcal{O}(\delta^2)$. This error vanishes again by taking the limit $\delta \to 0$. After that, an auxiliary bosonic field ϕ is introduced via Hubbard-Stratonovich transformation and fermion determinant is derived via integrating out Gassmannlike Gaussian integrals. By that only an integral over the bosonic field is left in the final

representation.

We start by replacing creation and annihilation operators of electron-kind (a) to hole-kind (b) for one spin component

$$\begin{aligned} c^\dagger_{x,1} &\to a^\dagger_x \qquad c_{x,1} \quad \to a_x \\ c^\dagger_{x,-1} &\to b_x \qquad c_{x,-1} \quad \to b^\dagger_x \end{aligned} \tag{2.22}$$

and thus the charge operator becomes

$$q_x = a^\dagger_x a_x - b^\dagger_x b_x \tag{2.23}$$

Through shifting the sign of the tight-binding term, which is possible due to anti-commutator relations, we find

$$\begin{aligned} H = &\kappa \sum_{x,y \in n.N.} (a^\dagger_x a_y + b^\dagger_x b_y + \text{h.c.}) + \frac{1}{2} \sum_{x,y} q_x V_{xy} q_y \\ &+ m_s \sum_x (a^\dagger_x a_x + b^\dagger_x b_x) - \mu \sum_x (a^\dagger_x a_x - b^\dagger_x b_x) \ . \end{aligned} \tag{2.24}$$

Now we write the grand-canonical partition function, which is given by

$$Z = \text{Tr} e^{-\beta H} \ , \tag{2.25}$$

as an integral over anti-commuting fermionic fields, represented through elements of a Grassmann algebra. Therefore we introduce coherent fermion states as follows

$$|\xi\rangle = e^{-\sum_\alpha \xi_\alpha a^\dagger_\alpha} |0\rangle \quad \text{resp.} \quad \langle \xi| = \langle 0| e^{-\sum_\alpha a^*_\alpha \xi_\alpha} \tag{2.26}$$

where α denotes the single-particle states of the system, ξ_α, ξ^*_α are Grassmann variables and $a_\alpha, a^\dagger_\alpha$ the creation and annihilation operators. These coherent states are eigenstates of the annihilation operators. By writing a trace of a bosonic operator A in the following form

$$\text{Tr}\, A = \int \left[\prod_\alpha d\xi^*_\alpha \, d\xi_\alpha \right] \ e^{-\sum_\alpha \xi^*_\alpha \xi_\alpha} \langle -\xi | A | \xi \rangle \tag{2.27}$$

we can write the partition function as

$$Z = \text{Tr}\, e^{-\beta H} = \int \left[\prod_x d\psi^*_x \, d\psi_x \, d\eta^*_x \, d\eta_x \right] \ e^{-\sum_x (\psi^*_x \psi_x + \eta^*_x \eta_x)} \langle -\psi, -\eta | e^{-\beta H} | \psi, \eta \rangle \tag{2.28}$$

If eq. 2.28 would be normal ordered we could use

$$\langle \xi | F(a_\alpha^\dagger, a_\alpha) | \xi' \rangle = F(\xi_\alpha^*, \xi_\alpha') e^{\sum_\alpha \xi_\alpha^* \xi_\alpha'} \tag{2.29}$$

and we would be done. Unfortunately, the interacting part of the Hamiltonian doesn't fulfill this criteria and thus we have to rewrite the Hamiltonian in an adequate way. Therefore we split up the partition function in N_t slices

$$e^{-\beta H} = \prod_n^{N_t} e^{-\delta H} \tag{2.30}$$

and inserting unity between every slice using the completeness relation

$$\int \left[\prod_\alpha d\xi_\alpha^* \, d\xi_\alpha \right] e^{-\sum_\alpha \xi_\alpha^* \xi_\alpha} |\xi\rangle\langle\xi| = 1 \tag{2.31}$$

of the chosen base. By this, we find

$$\begin{aligned} \operatorname{Tr} e^{-\beta H} = \int \prod_{t=0}^{N_t - 1} \left[\prod_x d\psi_{x,t}^* \, d\psi_{x,t} \, d\eta_{x,t}^* \, d\eta_{x,t} \right] e^{-\sum_x (\psi_{x,t+1}^* \psi_{x,t} + \eta_{x,t+1}^* \eta_{x,t})} \\ \langle \psi_{t+1}, \eta_{t+1} | e^{-\delta H} | \psi_t, \eta_t \rangle \end{aligned} \tag{2.32}$$

with $\delta = \frac{\beta}{N_t}$ as the discretization of the time axis. By this it is necessary to have anti-periodic boundary conditions in time direction:

$$\psi_{x,N_t} = -\psi_{x,0} \qquad \eta_{x,N_t} = -\eta_{x,0} \tag{2.33}$$

Now we take the first element of an expansion of $e^{-\delta H}$ and rewrite this part in a normal ordered form. Through this an error arises which is of the order $\mathcal{O}(\delta^2)$, but vanishes again by taking the continuum limit $\delta \to 0$. For the diagonal elements of H_{coul}, which is the only non trivial step, we find:

$$q_x V_{xx} q_x = V_{xx} \left(a_x^\dagger a_x + b_x^\dagger b_x - 2 a_x^\dagger a_x b_x^\dagger b_x \right) \tag{2.34}$$

Using eq. 2.29, we can write the partition function as

$$\begin{aligned}\operatorname{Tr} e^{-\beta H} = \int \prod_{t=0}^{N_t-1} \left[\prod_x d\psi^*_{x,t}\, d\psi_{x,t}\, d\eta^*_{x,t}\, d\eta_{x,t}\right] \exp\Bigg\{-\delta \Bigg[\frac{1}{2}\sum_{x,y} Q_{x,t+1,t} V_{xy} Q_{y,t+1,t} \\ - \sum_{\langle x,y\rangle} \kappa \left(\psi^*_{x,t+1}\psi_{y,t} + \psi^*_{y,t+1}\psi_{x,t} + \eta^*_{x,t+1}\eta_{y,t} + \eta^*_{y,t+1}\eta_{x,t}\right) \\ + \sum_x m_s \left(\psi^*_{x,t+1}\psi_{x,t} + \eta^*_{x,t+1}\eta_{x,t}\right) + \frac{1}{2}\sum_x V_{xx}\left(\psi^*_{x,t+1}\psi_{x,t} + \eta^*_{x,t+1}\eta_{x,t}\right) \\ - \sum_x \mu(\psi^*_{x,t+1}\psi_{x,t} - \eta^*_{x,t+1}\eta_{x,t})\Bigg] \\ - \sum_x \left[\psi^*_{x,t+1}\left(\psi_{x,t+1} - \psi_{x,t}\right) + \eta^*_{x,t+1}\left(\eta_{x,t+1} - \eta_{x,t}\right)\right]\Bigg\}\end{aligned} \tag{2.35}$$

with $Q_{x,t,t'} = \psi^*_{x,t}\psi_{x,t'} - \eta^*_{x,t}\eta_{x,t'}$.
The next step is to introduce an external scalar field via Hubbard-Stratonovich transformation as follows

$$\begin{aligned}\exp\left\{-\frac{\delta}{2}\sum_{t=0}^{N_t-1}\sum_{x,y} Q_{x,t+1,t} V_{xy} Q_{y,t+1,t}\right\} \approx \int D\phi \exp\Bigg\{-\frac{\delta}{2}\sum_{t=0}^{N_t-1}\sum_{x,y}\phi_{x,t} V^{-1}_{xy}\phi_{y,t} \\ -i\delta\sum_{t=0}^{N_t-1}\sum_x \phi_{x,t} Q_{x,t+1,t}\Bigg\}\end{aligned} \tag{2.36}$$

with

$$D\phi = \prod_{t=0}^{N_t-1}\prod_x d\phi_{x,t} \tag{2.37}$$

and thus rewrite eq. 2.35 as:

$$\begin{aligned}\operatorname{Tr} e^{-\beta H} = \int D\psi D\psi^* D\eta D\eta^* D\phi \exp\Bigg\{-\delta\sum_{t=0}^{N_t-1}\Bigg[\frac{1}{2}\sum_{x,y}\phi_{x,t}V^{-1}_{xy}\phi_{y,t} + \sum_x i\phi_{x,t}Q_{x,t+1,t} \\ - \sum_{\langle x,y\rangle}\kappa\left(\psi^*_{x,t+1}\psi_{y,t} + \psi^*_{y,t+1}\psi_{x,t} + \eta^*_{x,t+1}\eta_{y,t} + \eta^*_{y,t+1}\eta_{x,t}\right) \\ + \sum_x m_s\left(\psi^*_{x,t+1}\psi_{x,t} + \eta^*_{x,t+1}\eta_{x,t}\right) + \frac{1}{2}\sum_x V_{xx}\left(\psi^*_{x,t+1}\psi_{x,t} + \eta^*_{x,t+1}\eta_{x,t}\right) \\ - \sum_x \mu(\psi^*_{x,t+1}\psi_{x,t} - \eta^*_{x,t+1}\eta_{x,t})\Bigg] \\ - \sum_x \left[\psi^*_{x,t+1}\left(\psi_{x,t+1} - \psi_{x,t}\right) + \eta^*_{x,t+1}\left(\eta_{x,t+1} - \eta_{x,t}\right)\right]\Bigg\}\end{aligned} \tag{2.38}$$

The fermion matrix can than be introduced as

$$\begin{aligned} M_{(x,t)(y,t')} =& \delta_{x,y}\left(\delta_{t,t'} - \delta_{t-1,t'}\right) - \kappa\frac{\beta}{N_t}\sum_{\vec{n}}\delta_{y,x+\vec{n}}\delta_{t-1,t'} + m_s\frac{\beta}{N_t}\delta_{x,y}\delta_{t-1,t'} \\ & - \mu\frac{\beta}{N_t}\delta_{x,y}\delta_{t-1,t'} + \frac{V_{xx}}{2}\frac{\beta}{N_t}\delta_{x,y}\delta_{t-1,t'} + i\phi_{x,t}\frac{\beta}{N_t}\delta_{x,y}\delta_{t-1,t'} \end{aligned} \tag{2.39}$$

respectively

$$\begin{aligned} M'_{(x,t)(y,t')} =& \delta_{x,y}\left(\delta_{t,t'} - \delta_{t-1,t'}\right) - \kappa\frac{\beta}{N_t}\sum_{\vec{n}}\delta_{y,x+\vec{n}}\delta_{t-1,t'} + m_s\frac{\beta}{N_t}\delta_{x,y}\delta_{t-1,t'} \\ & + \mu\frac{\beta}{N_t}\delta_{x,y}\delta_{t-1,t'} + \frac{V_{xx}}{2}\frac{\beta}{N_t}\delta_{x,y}\delta_{t-1,t'} + i\phi_{x,t}\frac{\beta}{N_t}\delta_{x,y}\delta_{t-1,t'} \end{aligned} \tag{2.40}$$

and by this we can write the partition function in Gaussian integral form:

$$\begin{aligned} Z = \int D\psi D\psi^* D\eta D\eta^* D\phi \exp\Bigg\{ & -\frac{\delta}{2}\sum_{t=0}^{N_t-1}\sum_{x,y}\phi_{x,t}V_{xy}^{-1}\phi_{y,t} \\ & - \sum_{t,t'=0}^{N_t-1}\sum_{x,x'}\left[\psi^*_{x,t}M_{(x,t)(x',t')}\psi_{x',t'} + \eta^*_{x,t}M'_{(x,t)(x',t')}\eta_{x',t'}\right]\Bigg\} \end{aligned} \tag{2.41}$$

These Gaussian integrals can then be integrated out so that we find

$$Z = \mathrm{Tr}\, e^{-\beta(H-\mu N)} = \int D\phi\ \det M(\phi)\ \det M'(\phi)\ \exp\left\{-\frac{\delta}{2}\sum_{t=0}^{N_t-1}\sum_{x,y}\phi_{x,t}V_{xy}^{-1}\phi_{y,t}\right\} \tag{2.42}$$

If we set $\mu = 0$ we can write

$$Z = \int D\phi\ \det\left(M(\phi)M^\dagger(\phi)\right)\ \exp\left\{-\frac{\delta}{2}\sum_{t=0}^{N_t-1}\sum_{x,y}\phi_{x,t}V_{xy}^{-1}\phi_{y,t}\right\} \tag{2.43}$$

and therefore get the final representation of the partition function which can be used for HMC simulations, without a sign problem due to a real and positive fermion determinant. In actual application, there is the problem that rounding errors add up, produced by products of ϕ in size of the number of lattice sites [89]. To ensure numerical stability of the algorithm we make a convenient replacement of the field in the fermion matrix. More precisely we introduce a compact field through

$$\frac{\beta}{N_t}\,\delta_{xy}\delta_{t-1,t'}\left(\frac{N_t}{\beta} - \frac{V_{xx}}{2} - i\phi_{x,t}\right) \to e^{-i\delta\phi}\delta_{xy}\delta_{t-1,t'} \tag{2.44}$$

which was in detail shown in [86].

2.3.2. Potentials

In this work we use two different potentials which were presented here. We briefly review the Hubbard model first with focus on 2d-hexagonal lattice and then present the long-range interaction and discuss differences between them. A more comprehensive summary with regard to the hexagonal grid can be found in [4].

Hubbard model of the hexagonal lattice

The model named after John Hubbard was proposed by J. Hubbard [90], J. Kanamori [91] and M.C. Gutzwiller [92] in 1963, independently from each other for different issues related to correlated electrons in solids. It is the simplest and archetypical quantum many-body model thinkable and the first theoretical model which was able to describe an insulating as well as a metallic state in solid state physics. Thereby, it advanced the field of strongly correlated systems [93] and is still subject of active research. It extends the tight-binding model by introducing an energy amount U for particles on the same lattice site which represents Coulomb repulsion. Thus the Hamiltonian is

$$H_{Hubbard} = H_{tb} + H_{int} = -\kappa \sum_{\langle x,y \rangle} c^{\dagger}_{y,\sigma} c_{x,\sigma} + U \sum_{x} c^{\dagger}_{x,\uparrow} c_{x,\uparrow} c^{\dagger}_{x,\downarrow} c_{x,\downarrow} \ . \tag{2.45}$$

Although the model is quite simple, it contains a wide range of physical phenomena, such as magnetic ordering or superconductivity. Note that the model only defines a system by three effective parameters if translational invariance and only nearest-neighbor hopping is assumed. These are the ratio U/κ, the topology of the lattice and the number of particles on the lattice. This is both the strength and the weakness of the model. On the one hand it captures diverse phenomena and on the other hand it only models the shortest interaction of electrons possible in the view of solid state physics. For this reason it is only a good approximation in systems with no long-range interactions. Thus it can be seen as a good test case for qualitative studies but to obtain more details specific systems additional terms are needed.
Focusing on the 2d-hexagonal lattice it has been found that the second order semimetal-insulator transition takes place at $U/\kappa \approx 3.8$ by using Quantum Monte-Carlo methods [22,23] which was in accordance with previous studies which ruled out the possibility of a spin-liquid phase [94] and confirmed by calculations using the Dyson-Schwinger framework [24]. It has also been found out within this and further studies [95–97] that the transition is of the universality class of the chiral Heisenberg Gross-Neveu model in 2+1 dimensions with $N_f = 2$. An extended model with a nearest-neighbor interacting term V is supposed to favor a charge density wave phase. It was shown that the SM-SDW transition meets with the SM-CDW line and form a triple point

in the U-V phase diagram [24, 58, 98]. The question whether the extended Hubbard model is an appropriate description of graphene and the corresponding transitions or not is still under discussion [58]. In this work we use the Hubbard model as a test case potential for applying the LLR algorithm in order to simulate at finite charge density while keeping the system as simple as possible.

Long-range interactions in graphene

Besides the studies of the hexagonal Hubbard model, one can consider a realistic potential that addresses the long-range interactions which plays a major role at least in pristine graphene [99]. As mentioned above the influence of the long-range Coulomb tail is still being discussed. Recently it was found evidence through HMC simulations, that the long-range Coulomb tail indeed changes the universality class of the hexagonal system from $N_f = 2$ chiral Heisenberg Gross-Neveu model in three space-time dimensions which describes the graphene Hubbard model to an exponential 'Miransky'-scaling [58,59]. This scaling was primarily predicted by a study within the Dyson-Schwinger framework [100]. Nevertheless, there are several renormalization group studies which reaffirm Gross-Neveu scenario by the observations that Coulomb tail interaction is marginally irrelevant [95, 101, 102].
In this work we use the realistic long-range interaction for simulations with spin-dependent chemical potential in order to investigate the influence of it on the band structure and specifically on the neck disrupting Lifshitz transition. The potential is composed of values from cRPA calculations until 3th-nearest-neighbor interaction from [99] extended by a partially screened Coulomb tail proposed in [99] and applied in [20]. Hence the combined potential is

$$V(r) = \begin{cases} U_{00}, U_{01}, U_{02}, U_{03} & \text{for } r \leq 2a \\ e^2 \left(m_0 \exp\left[-m_1 r^{1-\gamma} \right] + m_2 \right) & \text{for } r > 2a \end{cases} \tag{2.46}$$

with

$$U_{0x} = \begin{cases} 9,3\, eV & \text{for } x = 0 \\ 5,5\, eV & \text{for } x = 1 \\ 4,1\, eV & \text{for } x = 2 \\ 3,6\, eV & \text{for } x = 3 \end{cases} . \tag{2.47}$$

The parameters m_i of the Coulomb tail were obtained by interpolating between the first four values and an unscreened Coulomb potential and can be found in Tab. 2.1

distance r	γ	m_0 [eV]	m_1 [eV]	m_2 [eV]
$2a < r \leq 8a$	0,632469	9,0380311	144,354	62,41496
$8a < r \leq 30a$	0,862664	2,0561977	27,8362	15,29088
$30a < r \leq 120a$	0,990975	1,0334789	0,0	-0,1345020
$120a < r$	1,0	1,0	0,0	0,0

Table 2.1.: Distance dependent parameter values of the partially shielded Coulomb potential for the HMC simulation in units of the lattice spacing a [20].

Additionally, it should be mentioned that we absorb $e^2 = \alpha = \frac{1}{137}$ in the matrix V in our notation and introduce a parameter $\lambda \in [0; 1]$ which rescales the potential in a way such that we find the non-interacting theory for $\lambda = 0$ and suspended graphene potential for $\lambda = 1$. Figure 2.8 shows the used potential in comparison with an unscreened pure Coulomb potential.

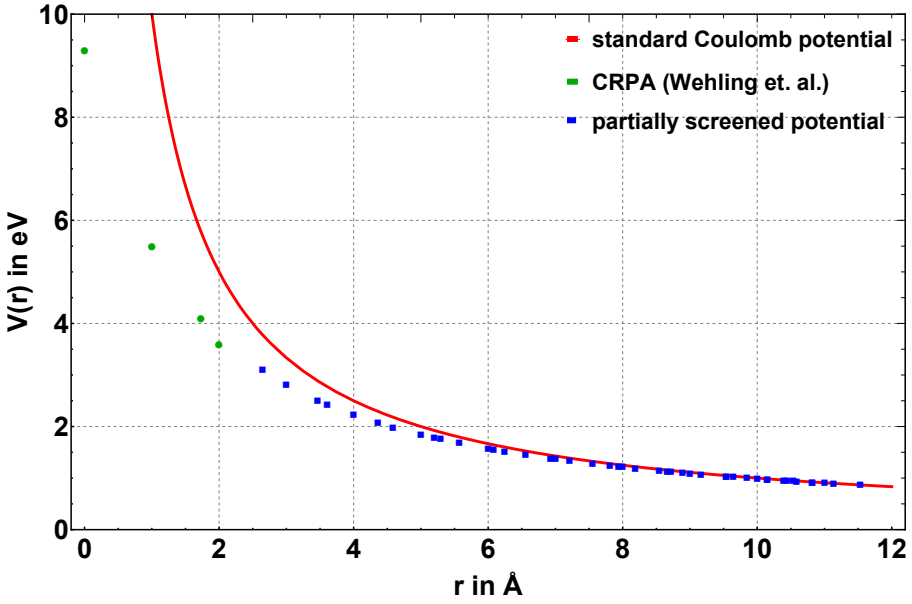

Figure 2.8.: Comparison of the standard Coulomb potential (red) with the partially screened potential given by eq. 2.3.2. The first four points are exact cRPA results of Ref. [99] (green), while remaining ones are obtained from interpolation based on thin-film model from the same reference (blue) (taken from [3])

2.4. Linear Logarithmic Relaxation method

The *Linear Logarithmic Relaxation* method, first described in [64] is based on the density of states approach introduced by Wang and Landau in 2001 [65] which basically uses independent random walks with a probability corresponding to the inverse density of states in different bounded energy intervals in order to produce flat histograms over the allowed range of energy for the purpose of sampling the density of states. The advantage of this method is that one can efficiently sample areas with a very low probability measure and at the same time avoid the problem of a non-positive probability measure as it occurs with finite densities in HMC sampling. However, this Wang-Landau method was designed for systems with discrete degrees of freedom. The LLR method takes up the basic idea and thus extends this method to theories with continuous degrees of freedom. Thus the limited energy interval is reduced to one point of a "generalized density of states" (gDOS) $\rho(X)$ which depends on some variable X. Then the logarithmic derivative $a(X) = \frac{d}{dX} \ln \rho(X)$ is estimated by stochastic approximation via the Robins-Monro algorithm. So one can step by step sample the whole area one is interested in with arbitrarily small step sizes and then reconstruct the gDOS by numerical integration. Using bootstrapping methods, the error can be kept constant over this whole range.
The method can be used to estimate the imaginary part of the Euclidean action $\rho(S_{im})$ or some related variable, which was done already for a Z_3 spin model at finite charge density [67] and for QCD in the heavy-dense limit [70]. Furthermore, there are studies in which the method has been used to calculate $\rho(E)$ in gauge theories (SU(2), U(1) see [64] and SU(3) see [69]) and was shown in q = 20 state Potts model [71] and U(1) gauge theory [68] that is algorithm is effective in dealing with ergodicity issues arising from first order phase transition in that systems. Additionally, the method was applied in a two-color QCD system with heavy quarks at finite densities in order to estimate the Polyakov-loop distribution [66]. Nevertheless, the method has not yet been applied in systems with fully dynamical fermions.

In the following, the details of the method in combination with HMC framework and the application on the hexagonal lattice with on-site Hubbard interaction will be presented. Furthermore, we show how to extract the particle density out of the generalized density of states. Details of the algorithm itself and the simulations can be found in chapter 3.4.

2.4.1. Generalized density of states

As already mentioned the generalized density of states $\rho(s)$ is the key element of the method and will be derived here. We start with the partition function (see eq. 2.42) and on-site Hubbard interaction which leads to

$$Z(\mu) = \int D\phi \det M(\phi, \mu) \det M^\dagger(\phi, -\mu) \exp\left\{-\frac{\delta_\tau}{2U} \sum_{x,t} \phi_{x,t}^2\right\} \tag{2.48}$$

Through making the replacement

$$\phi_{x,t} \to \phi_{x,t} - i\mu \tag{2.49}$$

which basically means that we absorb the chemical potential in the Hubbard field, we can shift the complex part of the action completely to the bosonic sector and get

$$Z(\mu) = \int D\phi \det M(\phi, 0) \det M^\dagger(\phi, 0) \exp\left\{-\frac{\delta_\tau}{2U} \sum_{x,t} (\phi_{x,t} - i\mu)^2\right\} \ . \tag{2.50}$$

By introducing the average Hubbard field as

$$\Phi = \frac{1}{V} \sum_{x,t} \phi_{x,t} \qquad \text{with } V = 2N_c N_t \tag{2.51}$$

and some rearranging we find

$$Z(\mu) = \int D\phi \left|\det M(\phi, 0)\right|^2 \exp\left\{-\frac{\delta_\tau}{2U} \sum_{x,t} (\phi_{x,t} - \Phi)^2 - \frac{\delta_\tau V}{2U} (\Phi - i\mu)\right\} \ . \tag{2.52}$$

Now we can introduce the generalized density of states $\rho(s)$ as

$$\rho(s) = \int D\phi \left|\det M(\phi, 0)\right|^2 \delta(\Phi - s) \exp\left\{-\frac{\delta_\tau}{2U} \sum_{x,t} (\phi_{x,t} - s)^2\right\} \tag{2.53}$$

and by that write the partition function as

$$Z(\mu) = \int ds \rho(s) \exp\left\{-\frac{\delta_\tau V}{2U} (s - i\mu)^2\right\} \ . \tag{2.54}$$

The goal for simulations in the LLR method is now to calculate derivatives of $\ln \rho(s)$ for the desired number of points s with high precision. From this set of data we can reconstruct the gDOS $\rho(s)$ by numerical integration [103].

2.4.2. Reconstructing the particle density

At this point we assume that we have determined the logarithmic derivation of the generalized density with statistical error. In the following we describe how to reconstruct the particle density out of this set of data from $a(s)$, which is

$$a(s) = \frac{d}{ds} \ln \rho(s) \ . \tag{2.55}$$

Due to the fact that $\rho(s)$ is in our case a periodic function with the period $P = \frac{2\pi}{\beta}$ (cf. sec. 3.4) we only need to sample an interval $\{s \in \mathbb{R} \,|\, 0 \leq s < P\}$ to get all the information we need for further calculations. For the sake of simplicity we choose N_s sampling points in the interval, which are equally distributed with a distance from each other of $\frac{2\pi}{\beta N_s}$. If one has this data set, there are several methods to reconstruct the particle density (or other observables of interest), but they all try to approximate the integral from equation 2.54. A promising strategy is to express the gDOS via its Fourier transform and to rewrite the grand canonical partition function $Z(T, V, \mu)$ in such a way that in the end it can be represented as a Laplace transform of the canonical partition function $Z(T, V, N)$. Thus, a fugacity expansion is carried out. The canonical partition functions can then be identified as the Fourier coefficients of the gDOS. Therefore, we start here with formulating the corresponding Fourier series

$$\rho(s) = \sum_{n \in \mathbb{Z}} \rho_k e^{i \frac{2\pi}{P} k s} = \sum_{n \in \mathbb{Z}} \rho_k e^{i \beta k s} \tag{2.56}$$

and use them to rewrite the partition function eq. 2.54 as

$$Z(\mu) = \int ds \sum_{n \in \mathbb{Z}} \tilde{\rho}_k e^{-ik\beta s} \exp\left\{ -\frac{\delta_\tau V}{2U} (s - i\mu)^2 \right\} \ . \tag{2.57}$$

Thus we have only a finite sampling the coefficients are equal to the discrete Fourier transform

$$\tilde{\rho}_k = \frac{1}{N_s} \sum_{n=0}^{N_s - 1} \rho_{s_n} e^{2\pi i \frac{kn}{N_s}} \tag{2.58}$$

and eq. 2.57 becomes

$$Z(\mu) = \int ds \sum_{k=0}^{N_s - 1} \tilde{\rho}_k e^{-ik\beta s} \exp\left\{ -\frac{\delta_\tau V}{2U} (s - i\mu)^2 \right\} \ . \tag{2.59}$$

With some rearranging we find the following shifted Gaussian function

$$Z(\mu) = \int ds \sum_{k=0}^{N_s-1} \tilde{\rho}_k \exp\left\{-\frac{\delta_\tau V}{2U}\left(s^2 - 2is(\mu + k\frac{\beta U}{\delta_\tau V}) + \mu^2\right)\right\} \tag{2.60}$$

and can carry out the integral. This way we get

$$Z(\mu) = \sqrt{\frac{\pi U}{\beta N_c}} \sum_{k=0}^{N_s-1} \tilde{\rho}_k \exp\left\{-\frac{U\beta}{4N_c}k^2 - \beta\mu k\right\} \ . \tag{2.61}$$

Note that this representation can be identified as the fugacity expansion and therefore we can also identify

$$Z(T, V, k) = \tilde{\rho}_k \exp\left\{-\frac{U\beta}{4N_c}k^2\right\} \tag{2.62}$$

as a pseudo-canonical ensemble with $k = N \bmod N_s$. Then we can obtain the chemical potential μ from

$$\begin{aligned} \mu(N \bmod N_s) &= -\frac{d}{dN}\frac{1}{\beta}\ln Z(T, V, N \bmod N_s) \\ &\approx \frac{1}{\beta}\left[\ln\tilde{\rho}_k - \ln\tilde{\rho}_{k+1} + \frac{U\beta}{N_c}(2k+1)\right] \ . \end{aligned} \tag{2.63}$$

The particle density $n(\mu)$ can now be found through inversion of eq. 2.63.

2.4.3. Reconstructing via compressed sensing

In section 2.4.2 we have described the gDOS $\rho(s)$ in the form of a Fourier series where the number of coefficients is equal to the number of sampling points N_s. However, one can first fit the function with other sets of orthogonal functions and by that interpolate between two sampling points. Then additional points can be generated in between and this new set of data can then be used instead as input to determine the particle density $n(\mu)$. In doing so, one assumes that the sampling was chosen so dense that no large jumps would be expected within the non-sampled area. This procedure is called Compressed Sensing in context of the LLR literature [70, 104]. The principal hope is that a wisely chosen set of functions, which contains the true physics of the theory will suppress noise in the numerical data for $\ln\rho(s)$ by interpolating between the supporting points. However, the correct set of functions cannot be determined without information about the physics of the system, and therefore they usually have to be guessed. In section 5.3 one finds results of this procedure with fits through Taylor series as well as with Chebyshev polynomials of the first kind for one set of parameters exemplary to show the degree of improvement in our system.

3. Simulation

In this chapter we present the algorithms used in this work. All simulations are based on the Hybrid-Monte-Carlo framework which is presented first. Then we explain the fermion sign problem and introduce the observable for spin-dependent chemical potential and the method of data analysis. Afterwards, the LLR algorithm is explained in detail, whereby we first formulate the truncated and reweighted expectation value and then discuss the Robins-Monro algorithm and the corresponding data analysis.

3.1. The Hybrid Monte Carlo method

The basic idea of Monte Carlo simulations is to estimate a selected observable by executing a large number of random experiments of a system. The observable marks an area of the configuration space defined by the system. In high dimensional systems, however, this relevant area will become smaller and smaller, so it is necessary to restrict the sampling of the random space by known properties of the system. This is known as *importance sampling*. The sampling, which defines the Hybrid-Monte-Carlo method (HMC) is a combination of molecular dynamics and Metropolis acceptance step [105]. More precise, one performs updates by integrating out trajectories in the phase space using the Hamilton equations and checking the result by an acceptance step weighted by the Boltzmann distribution. For more details about the basic methodology used in this work see [20, 86, 106] or standard textbooks [88, 107].
In this section we present the necessary details of the method applied on the hexagonal lattice. First, we briefly describe the HMC algorithm and after that we will go into the details of the application on the hexagonal lattice such as thermalization and ergodicity issues coming from numerical integration.

3.1.1. Algorithm

The following derivations are based on [20, 86, 106]. We start with the basic and general idea of measuring an observable in Monte-Carlo methods by estimating

$$\langle O \rangle = \int D\phi O(\phi) P(\phi) \tag{3.1}$$

with $P(\phi)$ as a probability density and $O(\phi)$ is some function of the field variable ϕ. The remaining function $O(\phi)$ represents the function of some observable. The respective used observables are discussed separately in the corresponding chapters (see 3.3 and 3.4). In the case of 2+1 dimensional hexagonal lattice we identify ϕ with the Hubbard-Coulomb field introduced in chapter 2.3.1 and the probability distribution

$$P(\phi) = \frac{1}{Z} \det \left[M^\dagger(\phi) M\phi \right] e^{-S(\phi)} \ . \tag{3.2}$$

Besides the general presentation of an estimator for the observable $\langle O \rangle$, we will now go into more detail about the update mechanism that gives HMC its name. We want to generate representative configurations to approximate a thermodynamic ensemble. This is done by integration of Hamilton equations over a fictitious time axis τ to move from one configuration to the next. In order to describe one update step, we have to rewrite our formulation of the probability distribution $P(\phi)$. First, it is necessary to write the fermion determinant again as a Gaussian integral over pseudo-fermions so that we find

$$\begin{aligned} \mathrm{Tr}\, e^{-\beta H} = \int D\phi D\chi D\chi^* \exp \Bigg\{ -\frac{\delta}{2} \sum_{t=0}^{N_t-1} \sum_{x,y} \phi_{x,t} V_{xy}^{-1} \phi_{y,t} \\ - \sum_{t=0}^{N_t-1} \sum_{x,y} \chi^*_{x,t} \left(M M^\dagger \right)^{-1} \chi_{x',t'} \Bigg\} \ . \end{aligned} \tag{3.3}$$

We can split the action accordingly into a ϕ and a χ part and get

$$P(\phi, \chi) = \frac{1}{Z} e^{-S(\phi) - S'(\chi)} \ . \tag{3.4}$$

Now it is possible to update the two parts of a separately, starting with $S(\chi)$. Note that for updating $S'(\chi)$ the term $A = \left(M M^\dagger \right)$ has to be inverted in every update step. So performing fast matrix inversions are an essential ingredient for using the HMC algorithm properly. Since the number of flops for a direct inversion of a square matrix A scales with $\mathcal{O}(N^3)$ (with $N = \mathrm{rank}(A)$) and we deal with large matrices of the $\mathrm{rank}(A) = 2N_c N_t$ it is necessary to use a faster algorithm for performing HMC updates. An appropriate method for finding a solution of $Ax = b$ for symmetric and positive definite sparse matrices is the Conjugate-Gradient algorithm (CG). This algorithm converges to the exact result within N steps, assuming exact arithmetic. The idea of CG is to find the minimum of the quadratic form $\frac{1}{2} x^T A x - x^T b$ which is equivalent to solve the mentioned linear equation. Therefore, a succession of search directions and improved minimizers is generated with respect to directions which were already taken and converge towards the minimum. A detailed and precise introduction in the algorithm can be found in [108] as well as in [109]. We use this algorithm to

solve $M(\phi)^{-1}_{ini}\chi = \rho_{ini}$ where ρ_{ini} is a random chosen Gaussian-distributed complex field. The energy difference of the fermionic part is then calculated by obtaining $M(\phi)_{end}\chi = \rho_{end}$ and taking $\Delta H_F = (\rho^\dagger\rho)_{end} - (\rho^\dagger\rho)_{ini}$. This last step can only be taken after ϕ is updated,of course
For updating the Hubbard field ϕ a fictitious momentum field π with $P(\phi) \propto e^{-\frac{1}{2}\pi^2}$ is introduced. Then the Hamiltonian and corresponding equations are defined as

$$\begin{aligned} H_B =& S(\phi) + S'(\chi) + \frac{\pi^2}{2} = \frac{\delta}{2}\phi^{-T}V^{-1}\phi + \frac{1}{2}\pi^T\pi \\ \text{with} \quad & \left[\frac{d\phi}{d\tau}\right]^T = \frac{\partial H_B}{\partial \pi} \quad \text{and} \quad \left[\frac{d\pi}{d\tau}\right]^T = -\frac{\partial H_B}{\partial \phi} \end{aligned} \tag{3.5}$$

with a fictitious time τ. A new configuration of the field can then be found by integrating this system of equations. The forces required for integration can be looked up in [20]. For the numerical integration we use the leapfrog integrator. The advantage of this method is that it provides time-reversal invariance, momentum conservation and symplecticity. The numerical integration error ΔH is of order $\mathcal{O}(\epsilon^2)$ where ϵ denotes the step-size. After an integration of n steps with step-size ϵ a new configuration is obtained and can be used to obtain the total energy difference $\Delta H = \Delta H_F + \Delta H_B + \Delta H_\pi$ for a final Metropolis Check [110], which accepts a new configuration with the probability $\min(1, e^{-\Delta H})$. This step is performed at the end of an update to compensate the numerical errors and ensure that each configuration can be considered as an element of a Markov chain and our resulting ensemble of configurations are distributed with correct Boltzmann weights . In summary, an update step runs as follows (cf. [20]):

- Create momentum field π via Gaussian noise $P(\pi) \propto e^{-\frac{1}{2}\pi^2}$
- Update pseudo-fermion fields by generating a Gaussian distributed complex field $P(\chi) \propto e^{-\chi^\dagger - \chi}$ and obtain χ via CG
- Generate a molecular dynamics trajectory through integration of Hamilton's equations
- Calculate energy difference ΔH with new configuration of ϕ
- Perform a Metropolis check to correct step-size error. Accept a new configuration with $P = \min(1, \exp -\Delta H)$

3.1.2. Details in the application of HMC

Besides the general introduction of the HMC for 2d-hexagonal lattice it is useful to point out some important details of the application. Here we give an overview of useful choice of simulation parameters regarding to a efficiently working algorithm and discuss problems and a possible solution arising from numerical integration. For the whole set of parameters used for simulations see Appendix D and E.

Thermalization

To simulate a quantum system using HMC it must first be brought into thermodynamic equilibrium. This process is called thermalization. The choice of the start distribution and the combination of step-size and trajectory length has a great influence on the speed of the process and once an equilibrium is reached also on the auto-correlation of the configurations. We therefore try to save computing time and keep the thermalization process as short as possible and the update mechanism efficient by cleverly choosing the simulation parameters. In other words, we want to ensure that the algorithm can reach an appropriate area of the configuration space as quick as possible. Let us first look at the choice of the trajectory length and take advantage of the fact that we have chosen a compact formulation of the Hubbard field (cf. eq. 2.44). The factor $e^{-i\delta\phi}$ which occurs in the fermion matrix has a significant influence, due to forcing the possible values of the fermion determinant in a periodic interval. We have found that a length of order $\frac{1}{\delta}$, which means that the values of ϕ can evolve within the order of the interval length, is a good choice for fast thermalization. Furthermore, it was found that an ordered start, meaning $\phi_i = const.$ leads to a faster convergence than a start with random distributed values of ϕ_i. If this choice is taken into account, the system reaches equilibrium within a few steps and the auto-correlation is small. Additionally, it should be mentioned that we always chose combinations of step-size and step-number that the Metropolis acceptance rate was above 50%.

Domain Walls

A problem that arises when implementing the HMC algorithm is that so-called exceptional configurations can occur due to the structure of the fermion determinant [111]. These are configurations in which $\det MM^\dagger = 0$ and hence have no contribution in the probability weights but generate barriers in the fermion force since the inverse of the fermion matrix contributes there. This phenomenon parts the whole configuration space in sub-domains in which an integrator can get stuck and by this can generate ergodicity problems since the whole space is not reachable any more [20,86]. A method to avoid this ergodicity issue is to implement an additional sub-lattice staggered mass term that makes the barrier height finite and by this enables the integrator to move through different sub-domains. Physical results can then be obtained by successively reducing the mass m_s and extrapolating it to zero staggered mass. Another possible options are to complexify the Hubbard field and by this circumvent the barriers [60] or to use sophisticated integrators which are able to tunnel through the barrier [112]. Furthermore, it was recently shown that it is possible to formulate the fermion operator in a way that these ergodicity issues do not occur [113]. In this work we go the way of adding the sub-lattice staggered mass term m_s and discuss its impact on the

results in the corresponding chapters.

3.2. The fermion sign problem

One major restriction of the Hybrid-Monte-Carlo method is that an interpretation as probability density of $P(\phi)$ is only possible if the functional values of $P(\phi)$ are real and positive definite over the whole space. The introduction of a chemical potential violates this condition due to breaking particle-hole symmetry and is widely known as the fermion sign problem [62]. Mathematically speaking, the problem is caused by precision errors when numerically integrating a strongly oscillating function, whereby positive and negative contributions can no longer cancel each other out exactly. This way of looking at the problem is discussed in the LLR-part of this study. Looking at the HMC formulation, the problem manifests itself by the fact that by introducing the chemical potential the fermion matrices of particle and holes $M(\phi)$ and $M^\dagger(\phi)$ can no longer be written as adjoint matrices (cf. chapter 2.3.1) because:

$$\begin{aligned} M(\phi,\mu)_{(x,t)(y,t')} =& M(\phi,0)_{(x,t)(y,t')} - \mu\frac{\beta}{N_t}\delta_{x,y}\delta_{t-1,t'} \\ \tilde{M}(\phi,\mu)_{(x,t)(y,t')} =& M^\dagger(\phi,0)_{(x,t)(y,t')} + \mu\frac{\beta}{N_t}\delta_{x,y}\delta_{t-1,t'} = M^\dagger(\phi,-\mu)_{(x,t)(y,t')} \end{aligned} \tag{3.6}$$

However, if the chemical potential is nevertheless introduced, the fermion determinant is becoming a complex number. If one now insert unity in the resulting partition function as follows

$$\begin{aligned} Z &= \int D\phi \ \det M(\phi,\mu) \det \tilde{M}(\phi,\mu) \frac{\det \tilde{M}(\phi,-\mu)}{\det \tilde{M}(\phi,-\mu)} \ \exp\left\{-\frac{\delta}{2}\sum_{t=0}^{N_t-1}\sum_{x,y}\phi_{x,t}V_{xy}^{-1}\phi_{y,t}\right\} \\ &= \int D\phi \ \left|\det M(\phi,\mu)\right|^2 \frac{\det \tilde{M}(\phi,\mu)}{\det \tilde{M}(\phi,-\mu)} \ \exp\left\{-\frac{\delta}{2}\sum_{t=0}^{N_t-1}\sum_{x,y}\phi_{x,t}V_{xy}^{-1}\phi_{y,t}\right\} \end{aligned} \tag{3.7}$$

one can treat the resulting ratio as an observable of a HMC simulation and thus measure the expectation value of the ratio of the phase of the determinants in the "phase-quenched" theory.

$$\frac{Z(\mu)}{Z_{pq}(\mu)} = \left\langle \frac{\det \tilde{M}(\phi,\mu)}{\det \tilde{M}(\phi,-\mu)} \right\rangle_{pq} \tag{3.8}$$

Thereby it is possible to measure the severity of the sign problem and find the area in which simple reweighting of the partition function leads to physical results. In Figure 3.1 one finds exemplary histograms of the phase for different values of μ for long-range potential and on-site Hubbard potential respectively. There one can see that this reweighting method fails at very low values of chemical potential for both

kinds of potential. As a measure of severity, we have used the quality of agreement with a constant fit. This is expressed via the adjusted-R-squared, which is zero for a strictly non-linear relation between the data and the fitted curve and one for a perfect linear dependence [3].
Since the sign-problem is a very crucial problem of numerical methods in physics several methods have been proposed in the last decades to reduce the problem for special cases. Among them are for example Lefshetz thimbles [114–116] or attempts to reach higher μ via Taylor expansion [117]. Nevertheless, it is still unclear whether there is a general solution in polynomial time to this problem [63]. As already mentioned, in this thesis two methods are used to reduce or avoid the sign-problem. By introducing a spin-dependent potential, the problem is circumvented in so far as a similar theory is simulated (see chapter 3.3). In the case of graphene this "phase-quenched" theory is actually physical and is equivalent to simulating an in-plane magnetic field. With the other method, known as LLR algorithm, we deal with a real charge chemical potential and calculating the electron density as a function of μ from HMC results directly (see chapter 2.4 and 3.4).

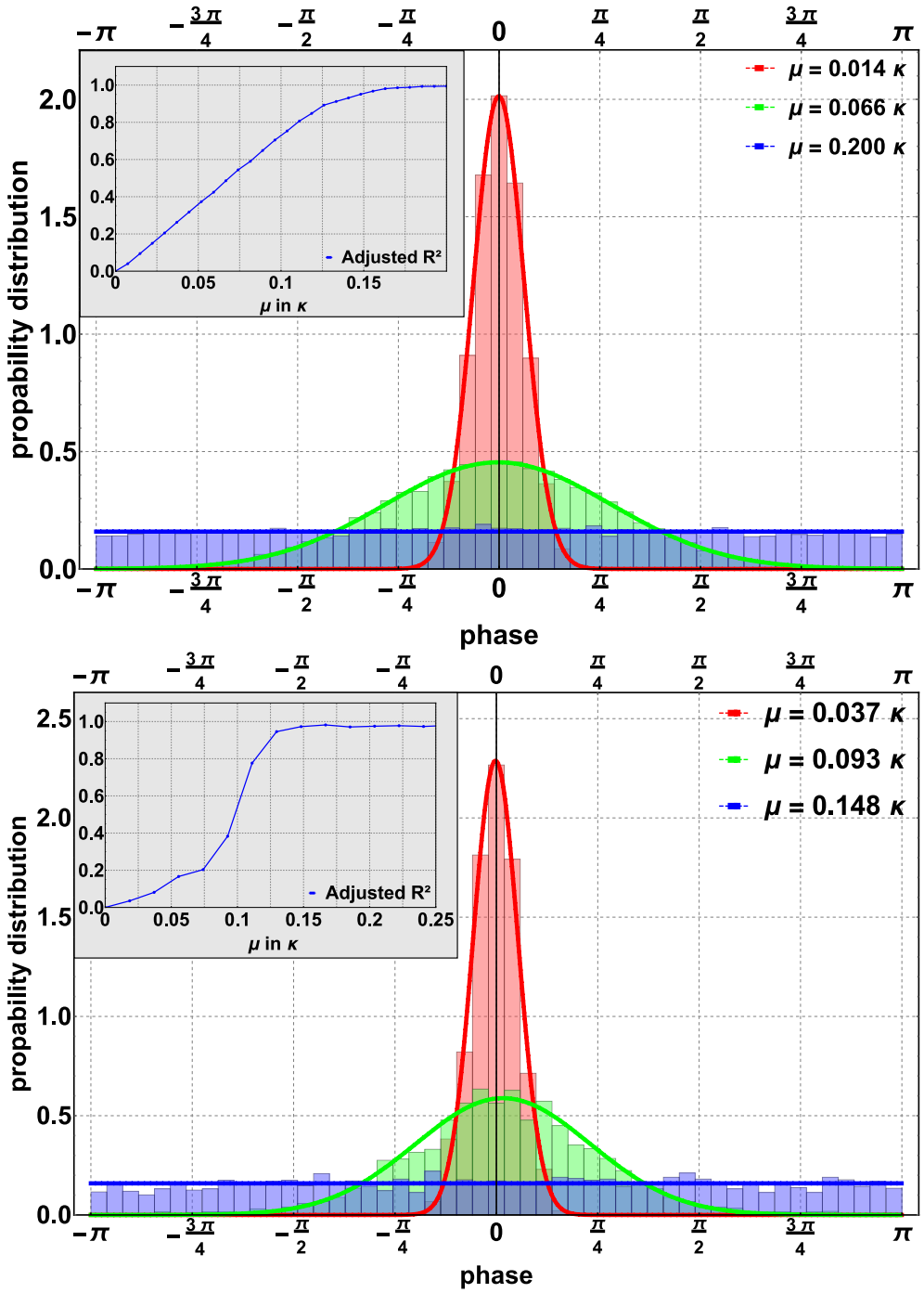

Figure 3.1.: Illustration of the fermion sign problem through showing the ratio from eq. 3.8 measured in a 6x6x6 lattice at $\beta = 5.4\kappa^{-}1$ with on-site Hubbard potential (above) / long-range potential (below) at an interaction strength of of $U = 0.1\kappa$ / 10% of suspended graphene. The signal is lost at $\mu \approx 0.2\kappa$ / $\mu \approx 0.15\kappa$ meaning the data can be fitted by a uniform distribution what indicates a hard sign problem.

3.3. Application of HMC on spin-dependent chemical potential

For studying spin-dependent chemical potential we focus on the particle-hole susceptibility due to their relation to the density of states and the Lifshitz transition as shown in the chapter 2.2.2 and also their good accessibility within HMC simulations. The common number susceptibility (per unit cell) is given by

$$\frac{1}{\beta N_c}\frac{d^2}{d\mu^2}\ln Z = \frac{1}{\beta N_c}\left[\frac{1}{Z}\frac{d^2}{d\mu^2}Z - \frac{1}{Z^2}\left(\frac{d}{d\mu}Z\right)^2\right] \tag{3.9}$$

and agrees with particle-hole susceptibility up to a factor of β. With the path-integral representation of the grand-canonical partition function Z from eq. 2.42 we can write $\chi(\mu)$ and thus the derivatives of Z in terms of $M(\phi)$ since only the fermion matrix part of Z contains the chemical potential μ. Hence we find

$$\frac{d}{d\mu}\det\left(MM^\dagger\right) = 2\det\left(MM^\dagger\right)\mathrm{Re}\,\mathrm{Tr}\left(M^{-1}\frac{dM}{d\mu}\right) \tag{3.10}$$

and

$$\begin{aligned}\frac{d^2}{d\mu^2}\det\left(MM^\dagger\right) = 4\det\left(MM^\dagger\right)\Bigg\{&\left[\mathrm{Re}\,\mathrm{Tr}\left(M^{-1}\frac{dM}{d\mu}\right)\right]^2\\ &-\frac{1}{2}\mathrm{Re}\,\mathrm{Tr}\left(M^{-1}\frac{dM}{d\mu}M^{-1}\frac{dM}{d\mu}\right)\Bigg\}\ .\end{aligned} \tag{3.11}$$

With these derivatives we find for the full susceptibility

$$\begin{aligned}\chi(\mu) = &\frac{4}{N_c\beta}\frac{1}{Z}\int D\phi\det\left(MM^\dagger\right)\mathrm{Re}\,\mathrm{Tr}\left(M^{-1}\frac{dM}{d\mu}\right)e^{-S(\phi)}\\ &-\frac{2}{N_c\beta}\frac{1}{Z}\int D\phi\det\left(MM^\dagger\right)\mathrm{Re}\,\mathrm{Tr}\left(M^{-1}\frac{dM}{d\mu}M^{-1}\frac{dM}{d\mu}\right)e^{-S(\phi)}\\ &-\frac{4}{N_c\beta}\frac{1}{Z^2}\left[\int D\phi\det\left(MM^\dagger\right)\mathrm{Re}\,\mathrm{Tr}\left(M^{-1}\frac{dM}{d\mu}\right)e^{-S(\phi)}\right]^2\ .\end{aligned} \tag{3.12}$$

For further analysis it makes sense to look at connected χ_{con} and disconnected χ_{dis} contributions of the susceptibility separately. By this, the full susceptibility can be written as $\chi = \chi_{con} + \chi_{dis}$ with

$$\chi_{con} = -\frac{2}{N_c\beta}\left\langle\mathrm{Re}\,\mathrm{Tr}\left(M^{-1}\frac{dM}{d\mu}M^{-1}\frac{dM}{d\mu}\right)\right\rangle \tag{3.13}$$

and

$$\chi_{dis} = -\frac{4}{N_c\beta}\left\{\left\langle\left[\mathrm{Re}\,\mathrm{Tr}\,\left(M^{-1}\frac{dM}{d\mu}\right)\right]^2\right\rangle - \left\langle\mathrm{Re}\,\mathrm{Tr}\,\left(M^{-1}\frac{dM}{d\mu}\right)\right\rangle^2\right\} \tag{3.14}$$

where we already have used eq. 3.1, meaning that brackets $\langle\rangle$ are understood as averages over a representative set of field configurations. For the explicit measurement of $\chi(\mu)$ we use noisy estimators and approximate

$$\begin{aligned} Tr(M^{-1}\tilde{M}) &\approx \frac{1}{N}\sum_{n=1}^{N}\xi_n^\dagger M^{-1}\tilde{M}\xi_n \\ Tr(M^{-1}\tilde{M})^2 &\approx \frac{1}{N(N-1)}\sum_{\substack{n,m=1,\\ n\neq m}}^{N}(\xi_n^\dagger M^{-1}\tilde{M}\xi_n)(\xi_m^\dagger M^{-1}\tilde{M}\xi_m) \end{aligned} \tag{3.15}$$

where ξ_n are randomly chosen from a Gaussian distribution. For canceling auto-correlation effects we use the binning method, which means that the set of data is divided into N blocks and taking the mean value of each block and use them as a new set of uncorrelated data. The ideal block size is defined by the integrated auto-correlation time

$$\tau_{int} = \frac{\sigma_N(X)}{\sigma 1(X)} \tag{3.16}$$

with $\sigma(X)$is the variance of the mean value X of each block. This value grows with increasing N, once it saturates the ideal block size is reached and the set of data can be treated as nearly uncorrelated data. The errors of the data are obtained via Gaussian error propagation for correlated data.

3.4. The LLR algorithm

The general idea of LLR was already discussed in sec. 2.4. Here we focus on the explicit implementation of LLR with respect to the generalized density of states derived in sec. 2.4.1. We first discuss the periodicity of the gDOS and introduce the truncated and reweighted expectation value, then focus on the Robins-Monro algorithm and finally going into details from data analysis.

3.4.1. Periodicity of the gDOS

As already mentioned we want to obtain the logarithmic slope of the generalized density of states $\rho(s)$ through evaluating $a_n = \frac{d}{ds} \ln \rho(s)\big|_s = s_n$ at a sufficiently dense set of supporting points with high precision. Then we can reconstruct the gDOS by numerical integration and use it to obtain the particle density from its Fourier transform. Before going into detail of the method it makes sense to focus on the properties of $\rho(s)$ first for selecting an adequate range for possible s_n. By introducing the compact Hubbard field (cf. eq. 2.44) we obtain products of complex exponential functions in the fermion determinant. This makes $\rho(s)$ periodic with a wavelength of $\lambda_{\rho(s)} = \beta$. Therefore, we only have to sample one period of $\rho(s)$ in order to get all information we need. In Appendix B we show explicitly how the period emerges in an example with no tight-binding contribution. This period dominates $\rho(s)$ for a case with finite κ, too.

3.4.2. Truncated and reweighted expectation value and Robins-Monro algorithm

We will now focus on the LLR method [64] and as starting point we define the truncated and reweighted expectation value as

$$\langle\langle W(\Phi)\rangle\rangle_n(\tilde{a}) = \frac{1}{Z_{LLR}} \int D\phi\, \theta_{[s_n,\delta_s]}(\Phi)\, |\mathrm{det}M(\phi)|^2\, W(\Phi)\, e^{-\beta S(\phi)}\, e^{-\tilde{a}\Phi} \tag{3.17}$$

with Z_{LLR} as normalization constant, Φ as average Hubbard field introduced in sec. 2.4.1, $\theta_{[s_n,\delta_s]}$ as window function around s_n of width δ_s and $\tilde{a}$ as an external parameter. If the chosen window is small enough we can approximate the logarithm of the generalized density of states in the interval $[s_n - \delta_s/2, s_n + \delta_s/2]$ with linear terms. We can write

$$\ln \rho(s) = \ln \rho(s_n) + a_n(s - s_n)\ . \tag{3.18}$$

and reconstruct $\ln \rho(s)$ via numerical integration (see sec. 3.4.3).
According to [64] the principal idea is to solve equation 3.17 through stochastic approximation in order to obtain values for the slope a_n. In 1951, H. Robbins and S.

Monro provided a procedure for finding roots in functions represented as an expectation value [118]. Using this method for eq. 3.17 means that an under-relaxed fixed point iteration

$$\tilde{a}_{j+1} = \tilde{a}_j + \alpha_j \frac{1}{\delta_s^2} \langle\langle W(\Phi)\rangle\rangle_n (\tilde{a}_j) \tag{3.19}$$

with

$$\sum_j \alpha_j \to \infty \qquad \text{and} \qquad \sum_j \alpha_j < \infty \tag{3.20}$$

converges to the right limit $\tilde{a}_{(\infty)} = a_n$ if we choose $W(\Phi) = \Phi - s_n$ in a way that

$$\langle\langle W(\Phi)\rangle\rangle_n(a_n) = 0 \ . \tag{3.21}$$

In the picture of Wang-Landau methods this means that we find a flat histogram by putting $\tilde{a}_{(\infty)}$ in eq. 3.17. Furthermore, a set of final values $\tilde{a}_{j_{cut},i}$ from a series truncated at j_{cut} are normal distributed around the true slope as mean value. Thus we obtain

$$\langle a_n \rangle = \frac{1}{N_a} \sum_{i=1}^{N_a} \tilde{a}_{j_{cut},i} \tag{3.22}$$

Once a dense set of a_n is obtained for one period of logarithmic gDOS we find

$$\ln \rho(s_n) = \delta_s \left(\sum_{n=1}^{m-1} \langle a_n \rangle + \frac{\langle a_m \rangle}{2} \right) \tag{3.23}$$

for s such that $s_m \leq s < s_{m+1}$. The errors of the corresponding mean values depend only on the width of the Gaussian distribution and remain in the same order of magnitude over the entire range. [64, 70]

3.4.3. Application of the LLR algorithm

In this section we want to provide deeper insights about how to apply LLR on the HMC framework described in sec. 3.1. According to the previous section we want to estimate $W(\Phi)$ on ensembles restricted to a specific interval. Therefore, we use HMC for generating configurations to measure on and first have to choose an appropriate window function. Intuitively one would choose a combination of Heaviside-theta functions here, but this would not work with HMC due to the nature of the updating mechanism which needs continuous functions. Thus we use a Gaussian distribution $\theta_{[s_n,\delta_s]}(\Phi) = \exp\left\{-(s-\Phi)^2/(\delta_s^2)\right\}$ as window function. The resulting force in the HMC update always pushes the system towards the mean $s = s_n$ of the distribution.

Hereby, the variance of the distribution is chosen in a way that the interval is small enough to obtain the slope properly but high enough to avoid integrator instabilities from high forces in the HMC update arising at very small δ_s (cf. 3.26). An optimal value for δ_s can be estimated by successively decreasing δ_s for a given s_n which increases $|a_n|$. If a_n no longer changes noticeably a good choice for δ_s has been found and can be transferred to other parameter values. Note that this works since we deal with periodic functions and therefore the estimated slope a_{s_n} numerically goes to zero for very large windows. Putting all chosen functions together we find for the observable

$$\begin{aligned}\langle\langle \Phi - s \rangle\rangle(\tilde{a}_j) = \frac{1}{Z_{LLR}} \int D\phi \, \det M(\phi) M^\dagger(\phi) \, (\Phi - s_n) \\ \times \exp\left\{ -\frac{\delta_\tau}{2U} \sum_{x,t} (\phi_{x,t} - s)^2 - \frac{1}{\delta_s^2} (s - \Phi)^2 - \tilde{a}_j \Phi \right\}\end{aligned} \tag{3.24}$$

with

$$\begin{aligned}Z_{LLR} = \int D\phi \, \det M(\phi) M^\dagger(\phi) \exp\left\{ -\frac{\delta_\tau}{2U} \sum_{x,t} (\phi_{x,t} - s)^2 \right. \\ \left. -\frac{1}{\delta_s^2} (s - \Phi)^2 - \tilde{a}_j \Phi \right\}\end{aligned} \tag{3.25}$$

and an additional force for HMC updates

$$F_{LLR} = \frac{2(s_n - \Phi)}{\delta_s^2} - \tilde{a}_j \ . \tag{3.26}$$

For the under relaxation parameter α_j we set

$$\alpha_j = \begin{cases} 1 & \text{for } 0 \leq j < j_t \\ \frac{1}{j - j_t} & \text{for } j > j_t \end{cases} \ . \tag{3.27}$$

which is the optimal choice for error suppression [70]. The parameter j_t denotes the number of thermalization steps of the LLR algorithm. Thermalisation means in this context to evolve j_t iteration steps without under relaxation in order to avoid correlations with respect to the start value of $\tilde{a}_j$. Additionally, we have to thermalize the HMC algorithm after each update of a_j before measuring the observable. It turned out that a constant value which minimizes the LLR-Force is a suitable choice

as initialization value of the Hubbard field for an efficiently working HMC algorithm. As an illustration of the method we show in Figure 3.2 an example of a set of Robbin-Monro iterations up to $j_{cut} = 105$ with $j_t = 15$ for a $N_x = N_y = N_t = 6$ lattice at $\beta = 2.7\kappa$, $m_s = 0.185\kappa$, $U = \kappa$ for $s = 1.33\kappa$. The expectation value of the slope a_n for this specific set of data is shown, too.

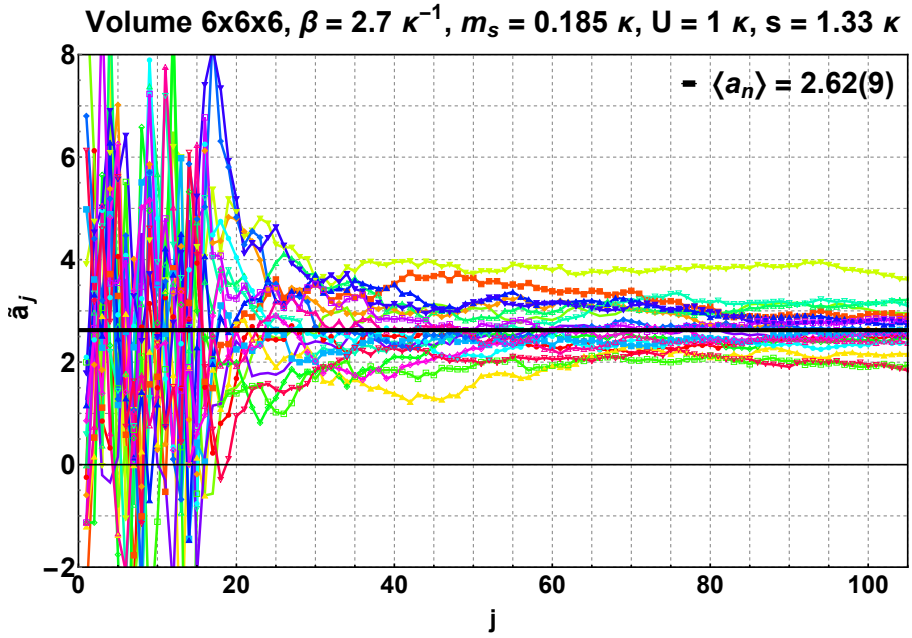

Figure 3.2.: Illustration of stochastic Robbins-Monro iteration. A set of 20 final values $\tilde{a}_{j_{cut}}$ are generated via updating according to eq. (3.19). Under-relaxation is switched on at $j_t = 15$. The black line shows $\langle a_n \rangle$ according to eq. 3.22.

Summarized, for a given set of lattice parameters and fixed s_n we perform the following procedure:

1. Set $\tilde{a}_0 = 0$ and thermalize Hubbard field via HMC.
2. Measure $\langle\langle W(\Phi)\rangle\rangle(a_j)_i$ on lattice configurations using HMC updates.
3. Calculate $\tilde{a}_{j+1}$ via eq. 3.19 with respect to eq. 3.27.
4. Use $\tilde{a}_{j+1}$ as new external parameter in eq. 3.24.
5. Thermalize the Hubbard field via HMC and repeat from 2 until $j = j_{cut}$.
6. Repeat from 1 until sufficiently many j_{cut} are generated.
7. Estimate $\langle a_n \rangle$ or $\ln \rho(s_n)$ from set of j_{cuts}, respectively.

The final step in the LLR-procedure is to treat the results from simulations in the right way to obtain $\rho(s)$ or in our case directly $\tilde{\rho}_k$ (see 2.4.2). The basic idea is to

use a simple form of numerical integration as described in eq. 3.23. Thereby, we only obtain a small set of $a_{j_{cut}}$ via simulations and improve the estimation of the mean values and corresponding error bars through the bootstrapping method [108,119]. We use bootstrapping to directly generate distributions of ρ_{s_n} or $\tilde{\rho}_k$, respectively. This means that we input randomly chosen values $a_{j_{cut}}, i$ from their corresponding data set for every used n, m in eq. 3.23 instead of the averages as written there. By repeating this procedure we generate a distribution of $\ln(\rho_{s_n})$ which we then use for calculating their mean and corresponding error. The same procedure is used for obtaining the Fourier coefficients in eq. 2.58.

4. Results for spin-dependent chemical potential

First we show results for parameters which only arise due to methodology of HMC in order to get an understanding of these more artificial parameters. The influence of the staggered mass m_s which was introduced in our system to avoid ergodicity problems and the finite discretization of the time axis δ_τ will be discussed and their implications on physical results will be shown. Afterwards, we concentrate on the influence of long-range interaction and temperature on the whole susceptibility. In the end of this chapter we concentrate on the behavior of the Lifshitz transition for a suspended graphene sheet. Finally the results of simulations with spin-dependent chemical potential and screened long-range potential are summarized and discussed.

4.1. Behavior of the Thomas-Fermi susceptibility

In the following we show the results for simulations with respect to staggered mass m_s, Euclidean-time discretization δ_τ, inverse temperature β and long-range interaction, which is, as already mentioned, rescaled by the parameter λ so that we simulate for $\lambda = 0.0$ the pure tight-binding theory and for $\lambda = 1.0$ suspended graphene. We discuss the implications of each parameter briefly, highlight important steps or assumptions within the simulations and compare the results to pure tight-binding theory.

4.1.1. Influence of the staggered mass m_s

In the non-interacting limit one can show easily that the staggered mass opens up a gap between the bands in the size of their specific value (see. fig. 4.1). This behavior is preserved in the interacting system by the reason that this effect arises within the tight-binding formulation and isn't much influenced by the interacting potential. Focusing on the susceptibility $\chi(\mu)$ one finds that small m_s change the shape significantly only in the Dirac cone area. Since, the main interest of this study lies in the change of whole bands through long-range interaction and the influence on the neck-disrupting Lifshitz transition at the VHS we can accept deviations in the Dirac cone area. Fortunately, for fast and stable simulations we need only small m_s which does not affect the shape of $\chi(\mu)$ at the VHS or at higher values of μ apart from statistical fluctuations. In Figure 4.1 the influence on the susceptibility both

for non-interacting and long-range interactions is shown. In order to have a good balance between accuracy and computational time all further results in this chapter were obtained for $m_s = 0.185\,\kappa$.

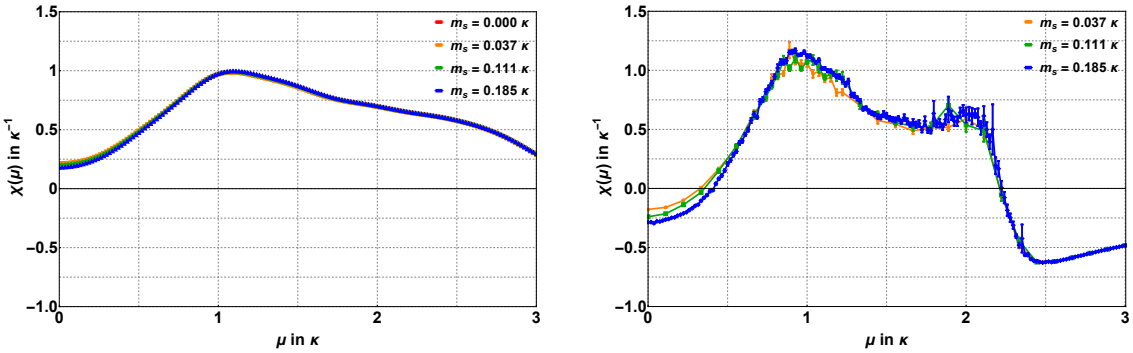

Figure 4.1.: Susceptibility $\chi(\mu_s)$ of a $N_c = 12^2$ hexagonal lattice at $\beta = 5.4\,\kappa^{-1}$ for pure tight-binding theory $\lambda = 0.0$ generated via eq. 2.20 [*left*] and for suspended graphene $\lambda = 1.0$ and $\delta = 2.7/6\,\kappa^{-1}$ generated via HMC. Shown are three different values of staggered mass, each.

4.1.2. Influence of the Euclidean-time discretization δ_τ

Controlling the effects induced by finite Euclidean time-discretization $\delta_\tau = \frac{\beta}{N_t}$, which occurs through Suzzuki-Trotter decomposition, is essential for using HMC methods in general. Since one obtains physical results only in the limit $\delta_\tau \to 0$ and this is computationally very expensive for low temperatures, large lattices or strong interactions we have to get a general understanding of the principle influence of δ_τ. If we find a well describable connection between $\chi(\mu)$ and δ_τ this can be used to investigate larger parameter ranges. So we carried out several simulations for high temperatures and small lattices for the whole range of interaction strength λ and fortunately found a general behavior which is shown and discussed in the following. Figure 4.2 shows the influence of δ_τ on the full susceptibility $\chi(\mu)$ for the non-interacting limit $\lambda = 0.0$, which implies that the Hubbard field is equal to zero on all lattice sites. This means that we can solve the system exactly without HMC updates.
The influence of discretization on $\chi(\mu)$ in the non-interacting limit can be largely described by a constant shift of the entire curve without changing its shape. The continuum limit, meaning the point-wise $\delta_\tau \to 0$ extrapolations, has a good agreement with the analytical form of the susceptibility calculated with eq. 2.20. An example for an continuum extrapolation the fit for $\mu = 0.0\kappa$ is shown in Figure 4.2, too. The behavior of the finite lattice discretization, which can be mainly expressed with a constant shift, continues with increasing interaction strength up to suspended

graphene $\lambda = 1.0$ except for statistical noise. Figure 4.3 shows HMC results for different discretization values and their continuum extrapolation for a set of four interaction strengths λ and shows the continuation of the behavior from the non-interacting case. Because of the described behavior we have chosen a rough discretization for qualitative investigations of further parameters like temperature and interaction strength in order to reduce simulation time. A more detailed analysis, whit focus on connected and disconnected part underlines this observation. In Figure 4.4 we compare $\lambda = 0.4$ with $\lambda = 1.0$ case for the full susceptibility and the connected and disconnected part, separately. Thereby we find that the disconnected part χ_{dis} is barely not affected by finite time discretization at all. Within our statistical error we obtain only noise distorting the constant shift coming from the connected part when both parts are added.

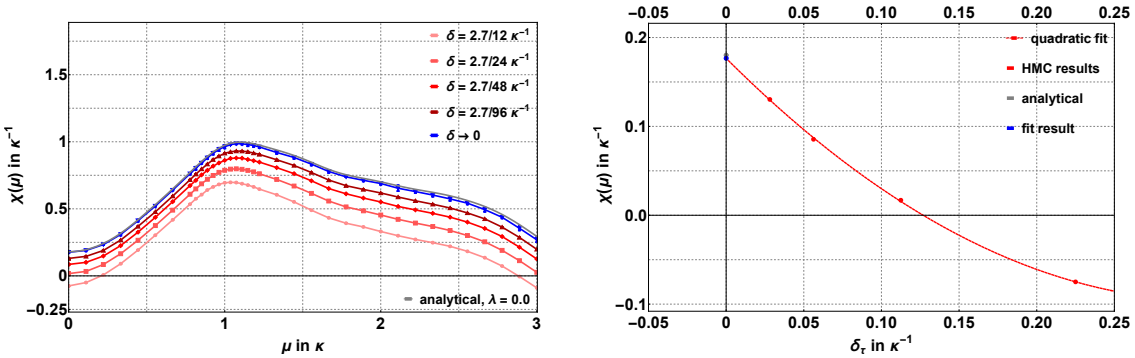

Figure 4.2.: Susceptibility $\chi(\mu_s)$ of a $N_c = 12^2$ hexagonal lattice at $\beta = 5.4\kappa^{-1}$ for pure tight-binding theory $\lambda = 0.0$. Shown are HMC results for different discretizations *(red)*, point-wise quadratic continuum extrapolation *(blue)* and analytically calculated ($\lambda = 0.0$) via eq. 2.20 *(gray)*. [*left*] / Quadratic continuum extrapolation for a 12x12 hexagonal lattice at $\beta = 5.4\kappa^{-1}$ for pure tight-binding theory $\lambda = 0.0$ at $\mu = 0.0\,\kappa$. [*right*]

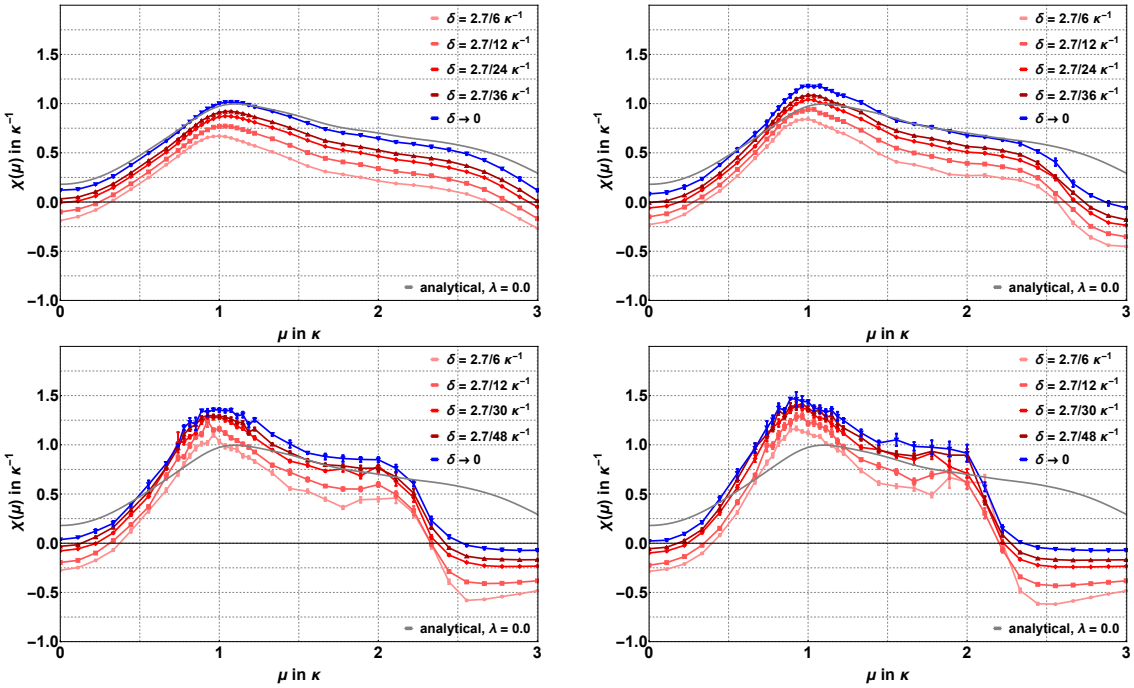

Figure 4.3.: Susceptibility $\chi(\mu_s)$ of a $N_c = 12^2$ hexagonal lattice at $\beta = 5.4\,\kappa^{-1}$ for different interaction strengths $\lambda = 0.1$ [*top, left*], $\lambda = 0.4$ [*top, right*], $\lambda = 0.8$ [*bottom, left*] and $\lambda = 1.0$ [*bottom, right*]. Shown are HMC results for different discretizations *(red)*, point-wise quadratic continuum extrapolation *(blue)* and analytically calculated ($\lambda = 0.0$) via eq. 2.20 *(gray)*.

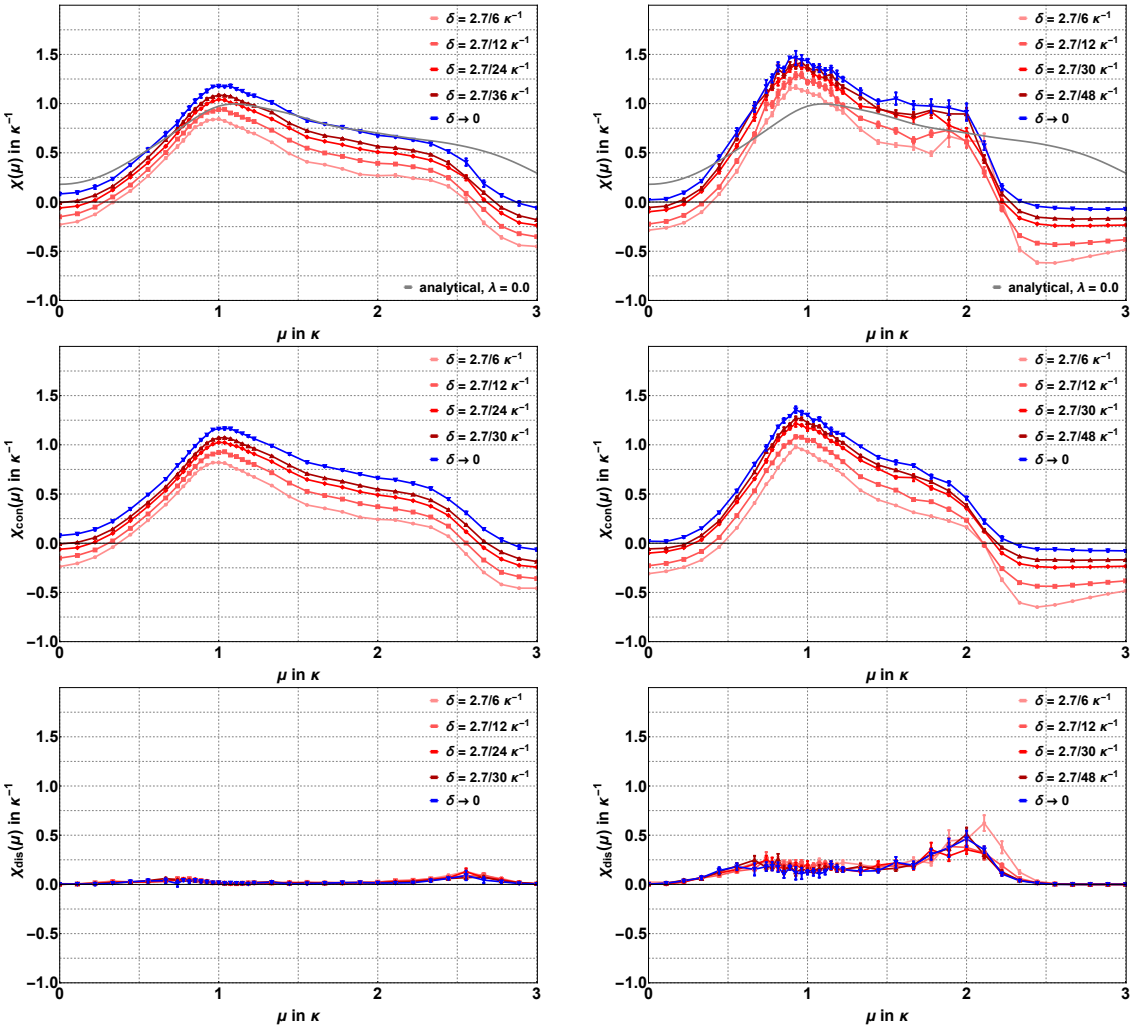

Figure 4.4.: Full susceptibility $\chi(\mu_s)$ [*top*] with corresponding connected χ_{con} [*middle*] and disconnected χ_{dis} [*bottom*] parts of a $N_c = 12^2$ hexagonal lattice at $\beta = 5.4\,\kappa^{-1}$ for interaction strength $\lambda = 0.4$ [*left*] and $\lambda = 1.0$ [*right*] in comparison. Shown are HMC results for different discretizations *(red)*, the point-wise quadratic continuum extrapolation *(blue)* and analytically calculated ($\lambda = 0.0$) via eq. 2.20 *(gray)*.

4.1.3. Influence of the inverse temperature β

Due to a fixed lattice we focus on the electron temperature here, meaning we have no phonon interaction implemented. As already discussed in section 2.2.2 the susceptibility in the non-interacting limit $\lambda = 0.0$ for $\beta \to \infty$ is equal to the density of states (cf. Fig. 2.6) and the Lifshitz transition is indicated in $\chi(\mu)$ through a logarithmic divergence of the peak height at the van Hove singularity. Here we show the results for the system with full long-range interaction $\lambda = 1.0$. All results were obtained for a lattice discretization $\delta = 2.7/6\,\kappa^{-1}$ and staggered mass $m_s = 0.185\,\kappa$. The rough discretization leads to a negative shift of the whole curve, which was explained in detail in section 4.1.2. Because of the context described in sec. 2.2.2 (cf. Fig. 2.6) the lattice has been chosen big enough to avoid finite size effects.
Figure 4.5 shows the full susceptibility for different inverse temperatures β and the corresponding connected and disconnected parts. The connected part behaves essentially as in the non-interacting scenario, while in the disconnected part two peaks are formed by lowering the temperature. The peak at the VHS is examined and explained in section 4.2. The peak at the Γ-point was not studied in detail due to limited computational resources but is discussed briefly in section 4.1.4 and 4.3.

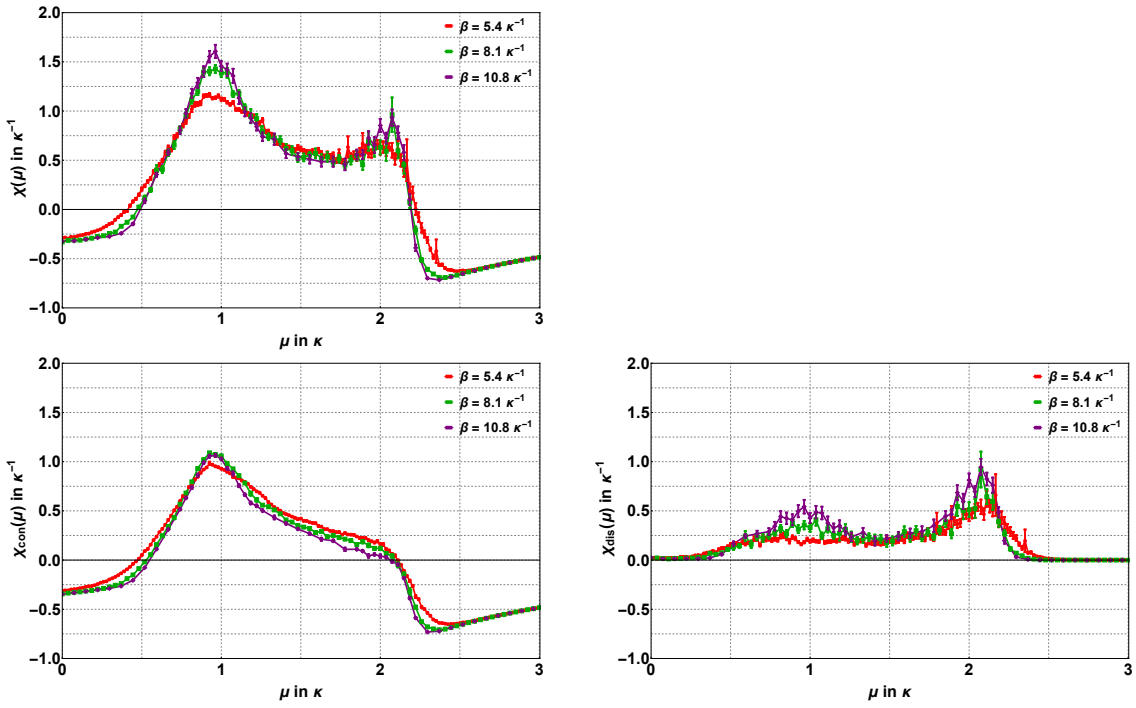

Figure 4.5.: Temperature dependence of $\chi(\mu)$ for suspended graphene $\lambda = 1.0$ at a lattice discretization $\delta = 2.7/6\,\kappa^{-1}$ and staggered mass $m_s = 0.185\,\kappa$. The corresponding lattice sizes are $N_c \in \{12^2, 18^2, 24^2\}$ for $\beta \in \{5.4\,\kappa^{-1}, 8.1\,\kappa^{-1}, 10.8\,\kappa^{-1}\}$ (*top*) and for the corresponding connected (*bottom, left*) and disconnected parts (*bottom, right*)

4.1.4. Influence of the long-range interaction strength

Here we present the general influence of inter-electron interactions on the particle-hole susceptibility. Therefore, we have chosen a high temperature $\beta = 5.4\,\kappa^{-1}$ and small lattice $N_c = 12^2$, which is not influenced by finite size effects. We also have carried out quadratic continuum extrapolations as described in 4.1.2 for each chosen value of the rescaled interaction parameter λ. The used values for lattice discretization δ can be taken from the Table D.3 in Appendix D. Figure 4.6 shows the full susceptibility as well as connected and disconnected parts. We still have a systematic discretization error which can be identified as the negative shift at high μ-values, due to the expectation that at high enough μ the susceptibility should fall to zero. By assuming this we find an additional systematic discretization error of around $0.08\,\kappa^{-1}$.

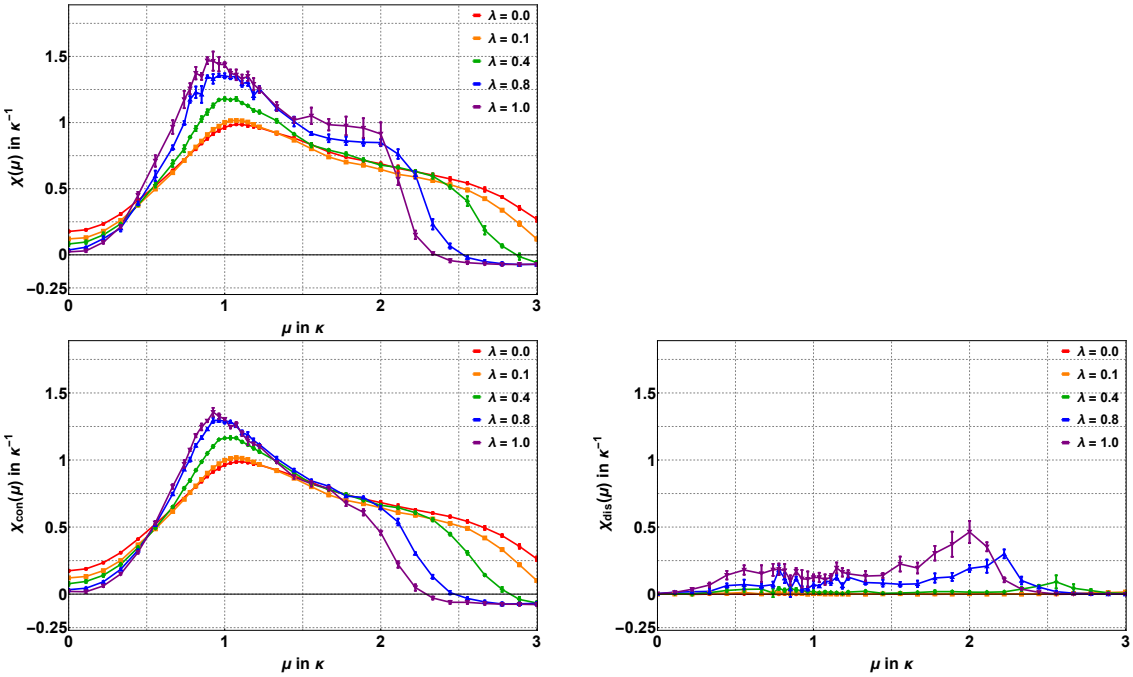

Figure 4.6.: Dependence of rescaled interaction strength λ on the susceptibility $\chi(\mu)$ for a $N_c = 12^2$ hexagonal lattice at $\beta = 5.4\,\kappa^{-1}$. Plotted are the quadratic continuum extrapolations for each set of parameters. Dependence of rescaled interaction strength λ on the connected *top* and disconnected *bottom* part of $\chi(\mu)$ for a $N_c = 12^2$ hexagonal lattice at $\beta = 2\,\kappa^{-1}$. Plotted are the quadratic continuum extrapolations for each set of parameterχ_{con} and χ_{dis}.

The disconnected part is exact zero in the non-interacting case because the expectation value of $\langle \mathrm{Re\,Tr}\,(...)^2 \rangle$ factorizes. So this part of the susceptibility comes entirely from many-body interactions. At high temperatures we find with increasing λ that a peak at high chemical potential is generated. This peak at the Γ-point indicates the end of the upper band which moves to lower values. This behavior is reflected

in a flattening of the dispersion relation around the Γ-point and in combination with the decrease in connected part at lower μ values we find a general compression of the whole conductance band, induced by electron interactions. However, we can not untangle effects from doping and interactions here but the combined effect is qualitatively in line with experimental observations [120]. This general compression effect from interactions also leads to a shift of the van Hove peak towards lower values, which is in line with experimental observations [41]. Another implication of increasing λ is the lowering of $\chi(\mu)$ near $\mu = 0.0\,\kappa$, which indicates, as expected, a gap opening for unphysical high values of interaction strength. Additionally, going to lower temperatures at fixed interaction strength, a peak in the disconnected part at the VHS is formed as it was described in section 4.1.3. The implications of this peak are highlighted in more detail in section 4.2.

4.2. Behavior at the van Hove singularity

As already mentioned in section 4.1.3, we find the formation of a peak in the disconnected part of the susceptibility at the VHS induced by electron interactions. We now focus on this phenomenon for graphene lattices at $\lambda = 1.0$. Since simulations at high β enlarge the required computing time drastically we generated the results only for high temperatures directly. At low temperatures we used the systematic of the finite volume effects at the VHS. According to the fact that odd lattices underestimate the real value of $\chi\mu$ and even lattices overestimate it (cf. sec. 2.2.2) we can simulate small lattices and can generate a series of mean values of χ_{peak} from subsequent lattices with them, which converges faster to the infinite volume value than a series of lattices with equal parity (cf. Fig. 4.7). For this method it is necessary to determine the position of the peak in the interacting system as accurately as possible. So we have carried out a series of simulations for even and odd lattices in the area where the peak is supposed to be, then added these values separately and made a quadratic fit to estimate the position and the corresponding value of χ_{peak} as accurately as possible. This procedure was then repeated until the value converged. In order to verify this method we used both, the described method with $N_c = 12^2$ and 13^2 lattices and simulations direct with converged large N for $\beta = 10.8\,\kappa^{-1}$ and $12.15\,\kappa^{-1}$. Then we used this method to obtain χ_{peak} up to $\beta = 16.2\,\kappa^{-1}$ with averages from lattice sizes $N_c \in \{10^2, 11^2, 12^2, 13^2\}$. In the near vicinity of a true thermodynamic phase transition this method should break down due to the normal finite-size scaling expected there.

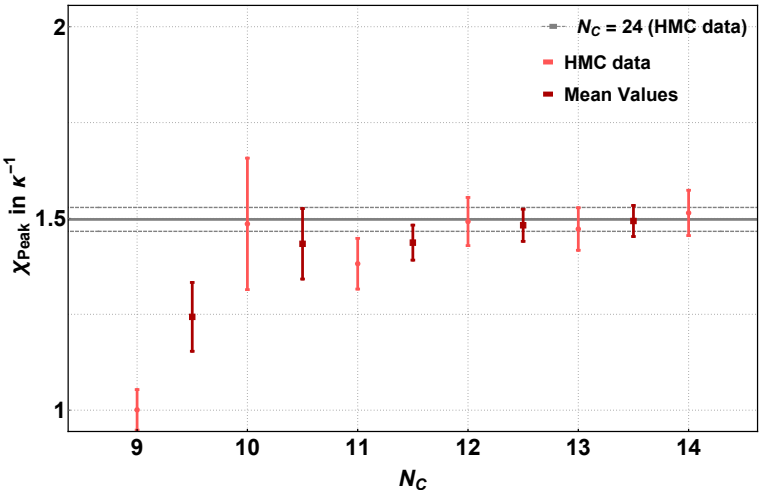

Figure 4.7.: Peak values of χ over different volumes for a $\beta = 10.8\,\kappa^{-1}$, $m_s = 0.185\,\kappa$ and $\lambda = 1.0$ system, exemplary.

In Figure 4.8 the infinite volume behavior of the susceptibility and the corresponding connected and disconnected part for different temperatures are shown. By fitting the data with

$$\chi_{peak}(T) = a \ln\left(\frac{\kappa}{T}\right) + b + c\frac{T}{\kappa} \tag{4.1}$$

in the interval $\beta \in \left[2.7\,\kappa^{-1}, 8.1\,\kappa^{-1}\right]$, we find that the logarithmic scaling which indicates the Lifshitz transition dominates the system within the interval. More explicitly, this can be shown by focusing on the connected part. Setting the fit parameter $a = \frac{3}{\pi^2\kappa}$ and doing this fit with two parameters again

$$\kappa\chi^{con}_{peak}(T) = \frac{3}{\pi^2} \ln\left(\frac{\kappa}{T}\right) + b + c\frac{T}{\kappa} \tag{4.2}$$

in the interval $\beta \in \left[2.7\,\kappa^{-1}, 6.75\,\kappa^{-1}\right]$ we find $b = 0.519(3)$ and $c = -0.472(8)$. This reproduces the pure tight-binding behavior from eq. 2.19 up to the constant shift coming from finite discretization $\delta = 2.7/6\,\kappa^{-1}$. Note that we find an agreement within 13% of the constant in eq. 2.19 and for the three-parameter fit an agreement within 1% with the constant $\frac{3}{\pi^2\kappa}$. The 2-parameter fit of χ_{con} is also shown in Fig. 4.8.

At lower temperatures $\beta > 6.75\,\kappa^{-1}$ the influence of the electron interaction becomes rapidly stronger and leads to a dominance of the disconnected part χ_{dis}, while the connected part χ_{con} becomes weaker and weaker. A description of the curves using logarithmic functions is no longer possible, here. Instead a power-law fit of the disconnected part is possible. We find χ_{dis} is well described by

$$\chi^{dis}_{peak}(\mu) = k\left|\frac{T - T_c}{T_c}\right|^{-\gamma} \tag{4.3}$$

for $\beta \geq 6.75\,\kappa^{-1}$. The fit parameter values can be taken from Table 4.1.

$\beta_c\ [\kappa^{-1}]$	$T_c\ [\kappa]$	γ	k $[\kappa^{-1}]$
16(2)	0.060(5)	0.52(6)	0.32(1)

Table 4.1.: Fit parameter values, corresponding to eq. 4.3

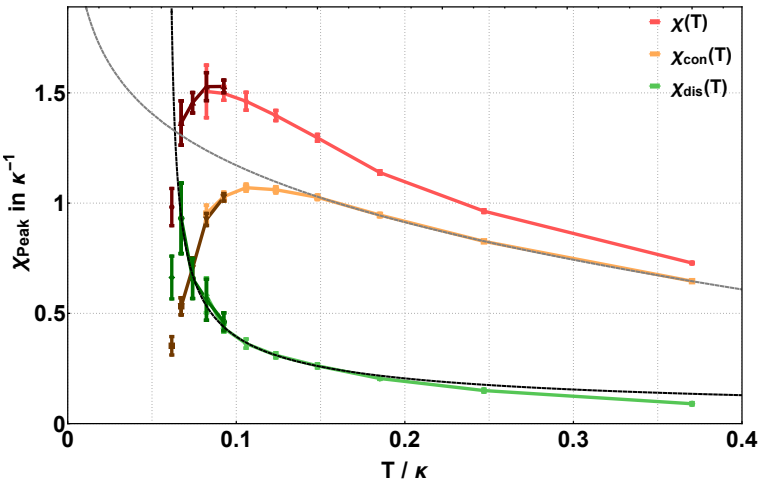

Figure 4.8.: Temperature dependence of χ_{max}. Shown are the full susceptibility, the connected and disconnected parts up to $\beta = 12.15\,\kappa^{-1}$ from simulations in the finite volume limit (*lighter color*) and from $\beta = 10.8\,\kappa^{-1}$ to $\beta = 16.2\,\kappa^{-1}$ obtained from average values of subsequent even and odd lattices (*darker color*). The gray line shows a 2-parameter fit from eq. 4.2 and the black line corresponds to the fit via eq. 4.3.

This fit indicates a thermodynamic phase transition driven by the disconnected susceptibility with a transition temperature of $T_c = 0.060(5)$. The value of the scaling exponent $\gamma = 0.52(6)$ is in good agreement with a theoretical consideration that finds $\gamma = 0.5$ for a single-particle band structure with a VHS, which is not point-like but extended. One finds this by writing the expansion eq. 2.13 the single-particle energy around a saddle point at $\epsilon_{\vec{k}} = \epsilon_0$ in a more general way

$$E(\vec{k})\Big|_{\mu=\kappa} = \kappa + \kappa\left(c_1\,(k_x a)^\alpha - c_2\,(k_y a)^\alpha\right) \tag{4.4}$$

which gives for $\alpha = 2$ and $\sqrt{c_1 c_2} = 3\sqrt{3}/4$ the tight-binding behavior and leads to the expected logarithmic scaling in the density of states (cf. sec. 2.2.2). If we set $\alpha = 4$ instead, the divergence of the peak turns into a square root divergence for $T \to 0$, meaning $\gamma = \frac{1}{2}$. So we can say in conclusion, that we found good evidence that the interactions turn the Lifshitz behavior occurring in pure tight-binding theory into a square root behavior with an extended VHS. This extended VHS was already found within an angle-resolved photoemission spectroscopy (ARPES) experiment with Ca-

doped graphene [41].

4.3. Summary

We have used a Hybrid-Monte-Carlo framework to study the hexagonal graphene lattice with long-range Coulomb interactions at finite spin-density as a possible circumvention of the fermion sign problem. Therefore, the nearest-neighbor tight-binding Hamiltonian was used, since it preserves the particle-hole symmetry and thereby enables the equivalence of spin and charge carrier density in the non-interacting theory. The many-body interactions were modeled by a partially screened Coulomb potential which reflects the screening from lower σ-bands for short distances and pure Coulomb interaction at long distances. As an observable the Thomas-Fermi susceptibility was used, which reflects the properties of the density of states, like linearity around the K-points and a logarithmic divergence which indicates a neck-disrupting Lifshitz transition at the M-Point. An analytical understanding of the non-interacting theory was given for using this as baseline for comparison with HMC results. We pointed out that the artificial parameters δ_τ and m_s, which arise due to path-integral formulation and Ergodicity issues of the HMC algorithm, can be controlled in a systematic way. Focusing on the results for changing interaction strength and temperature, we found qualitatively the same properties, like band-structure renormalization [120] or an extended van Hove singularity [41], as found by experimental studies with doped graphene. We showed that for the formation of the extended VHS the presence of many-body interactions is necessary in the chosen system. In detail this was confirmed by the observation of a peak-building at the VHS in the disconnected part of $\chi(\mu)$, which is a purely interaction driven part, and showing that this peak formation follows a square-root power-law for low temperatures. This also indicates that the topological transitions turn into a true quantum phase transition below T_c with chemical potential as control parameter. For high temperatures the logarithmic scaling of the neck disrupting Lifshitz transition was found in the connected part and reflects the single-particle behavior in this temperature range.
Additionally, a second peak formation could be observed at the Γ-point which indicates an interaction driven change of the topological void formation Lifshitz transition at the upper end of the conductance or the lower end of the valence band, respectively. This second peak was not analyzed in detail due to limited computational resources and can be object of further investigations. Looking at the results presented here, however, we guess that the point-like structure of the single-particle dispersion relation at the Γ-point may also change into a 2d-structure through many-body interactions and the formation of other phase might be observed.

5. Results for charge chemical potential

In this section we present the results for finite charge density in the on-site Hubbard model. We used the LLR algorithm to obtain the logarithmic slope of the generalized density of states as described in section 2.4 and then reconstruct the particle density via canonical ensembles. We show the results of the LLR simulations and discuss the implications of staggered mass m_s, time discretization N_t, finite Volume N_c and interaction strength U on the particle density $n(\mu)$ and compare the method to brute-force simulations. Furthermore, we improve the results by compressed sensing in two different ways for an exemplary set of parameters. But first, a general overview of the relation between the LLR method and the evaluation of the data by means of pseudo-canonical ensembles is given and important details are discussed.

5.1. General behavior

Here we discuss the general relationship between the gDOS generated by LLR and the resulting particle density using an exemplary data set. For this purpose we choose the results from $N_c = 6^2$, $N_t = 6$, $\beta = 2.7\,\kappa^{-1}$, $m_s = 0.185\,\kappa$ at interaction strength $U = 1.0\,\kappa$ which are shown in Figure 5.1. Shown are the obtained slopes $a(s)$, the resulting gDOS $\ln \rho(s)$ and their Fourier transforms $\ln \rho_k$ as well as the corresponding particle density $n(\mu)$. It can be seen very well there that despite the exponential error suppression in the obtained slope $a(s)$ we actually can use only a small part of the Fourier coefficients to determine the particle density. Nevertheless, the density can be obtained within acceptable error bars up to $\mu \approx 0.75\,\kappa$, whereas with brute force methods the signal is lost at about $\mu \approx 0.15\,\kappa$ for the same set of parameters. At first glance, this looks like an improvement by a factor of about 5, but this factor is reduced when the structure of the evaluation is examined more closely. Besides the difference of the logarithmic Fourier coefficients in eq. 2.63 there is a linear finite size term which can be obtained without any precision problems. Thus, the linear term must be subtracted from the particle density in order to determine the true gain from this method. Figure 5.2 shows the particle density for the chosen example with and without the linear term. We find that subtracting the term reduces the improvement factor by about half in the selected example. Since we only want to go into general behavior here, a more detailed comparison with brute-force follows in section 5.4 .

Here we want to discuss how this improvement comes about and where its limits are. For this purpose, the pure tight-binding formulation of the gDOS can be used to examine individual steps within the method in more detail.

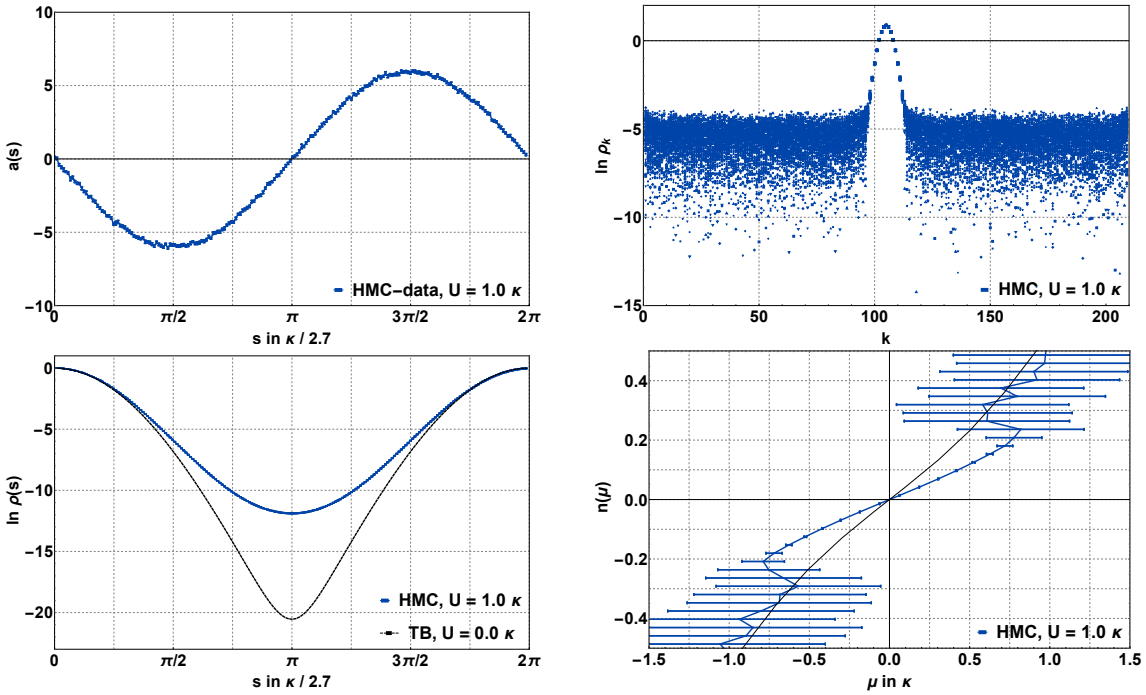

Figure 5.1.: The logarithmic slope $a(s)$ obtained via LLR *(left, top)*, the corresponding logarithmic gDOS $\ln \rho(s)$ *(left, bottom)*, their discrete Fourier transform $\ln \rho_k$ *(right, top)* and the particle density obtained via eq. 2.63 *(right, bottom)* for a $N_c = 6^2$, $N_t = 6$ lattice at $\beta = 2.7\,\kappa^{-1}$, $m_s = 0.185\,\kappa$ and $U = 1.0\,\kappa$. The black lines shows the analytical tight-binding case ($U = 0.0\,\kappa$).

One can derive the gDOS in pure tight-binding and find according to [121]

$$\ln \rho(s) = 2 \sum_{n,m} \ln \left[\cosh^2 \left(\frac{\tilde{\epsilon}_{mn}}{2T} \right) - \sin^2 \left(\frac{s}{2T} \right) \right] \tag{5.1}$$

Furthermore, the particle density normalized to the maximal number of electrons which can be added or removed in one unit cell is

$$n(\mu) = \frac{1}{N_c} \sum_{n,m} \left[\tanh^2 \left(\frac{\tilde{\epsilon}_{mn} - \mu}{2T} \right) - \tanh^2 \left(\frac{\tilde{\epsilon}_{mn} + \mu}{2T} \right) \right] \tag{5.2}$$

where we added the staggered mass to the energy $\tilde{\epsilon} = \sqrt{\epsilon^2 + m_s^2}$ as in previous sections, for a good comparison. We use eq. 5.1 to generate data sets for the chosen lattice for $U = 0.0\,\kappa$ with arbitrarily high precision in order to compare the method of approximating the particle density via canonical ensembles with the analytic formu-

lation of $n(\mu)$ in eq. 5.2. Therefore, we perform the discrete Fourier transformation without losing precision from the input data, using multi-precision libraries. Doing so, we can show that it is possible in principle to obtain the whole valence band within the method of obtaining the particle density via canonical ensembles. However, it is necessary to determine the Fourier coefficients very precisely which require a high precision of the input data, which is in shown in Figure 5.3. There we show how far one can get in the μ-range depending on the selected precision for the chosen example lattice at $U = 0.0\kappa$. Additionally, we show that the required number of digits increases linearly with rising temperature. Note that even at a very high temperature of $\beta = 2.7\,\kappa^{-1}$ one needs a precision of141 digits to obtain the whole band. Nevertheless, with input data in double precision we already reach the van Hove singularity within this example lattice. Unfortunately, the number of needed digits is also getting worse with increasing volume since the method is based on the fugacity expansion.
So the key question is how precise we can estimate the slope $a(s)$ with the LLR-framework and how results are influenced by the parameters of the system. Since the method of evaluation with canonical ensembles as well as HMC simulations break down at low temperatures and large volumes, we concentrate in the following on the area in which simulations are generally possible and feasible within reasonable times. Therefore we have set the inverse temperature $\beta = 2.7\,\kappa^{-1}$ and concentrate on $N_c \in \{6^2, 12^2\}$ lattices.

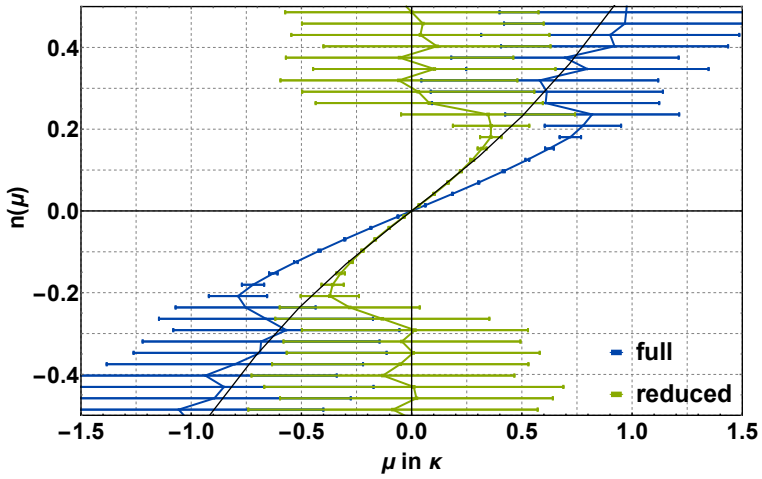

Figure 5.2.: Comparison of the full particle density and the one reduced by the linear term (see. eq. 2.63) for the chosen exemplary data set ($N_c = 6^2$, $N_t = 6$, $m_s = 0.185\,\kappa$, $U = 1.0\,\kappa$). The black line shows the pure tight-binding density.

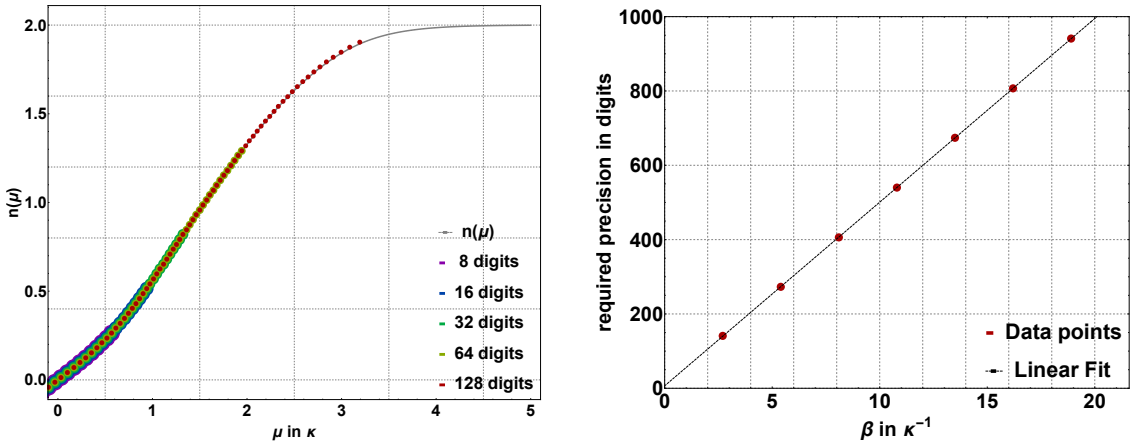

Figure 5.3.: Particle density $n(\mu)$ in tight-binding formulation $U = 0.0\,\kappa$, obtained via canonical ensembles for different precisions of input data in comparison to the density calculated via eq. 5.1 for $\beta = 2.7\,\kappa^{-1}$ *(left)* and the number of digits needed to obtain the whole valence band depending on the temperature for the chosen exemplary data set ($N_c = 6^2$, $N_t = 6$, $m_s = 0.185\,\kappa$).*(right)*

5.2. Influence of the system parameters

Here we give an overview of the influence of the staggered mass m_s, time discretization N_t, finite Volume N_c and the interaction strength U on both the generalized density of states and the corresponding particle density. We show in all sections only the particle densities without the linear term for the reason described in 5.1.

5.2.1. Staggered mass m_s

Since the staggered mass produces a gap already, we have set the on-site potential to a small value $U = 0.1\kappa$ and carried out simulations for three different values of m_s on a $N_c = 6^2$, $N_t = 6$ lattice. In order to save computing time we also chose a rough sampling of the slope $a(s_n)$ with $n \in \{1; 64\}$. Within this choice we find no significant influence of the staggered mass on the particle density as shown in Figure 5.4. However, decreasing the staggered mass m_s shifts the minimum of the $\ln \rho(s)$ to lower values but since we have a logarithmic scale here this influence is strongly suppressed in the gDOS. But this effect should become more relevant if $\ln \rho$ moves to smaller values overall, i.e. gDOS is less concentrated around zero s. As one would expect, such behavior can be achieved by reducing the temperature or increasing the interaction strength (as discussed in 5.1). Since we have found no influence of the staggered mass on the particle density for our chosen temperature, we use the highest mass $m_s = 0.185\,\kappa$ for further simulations.

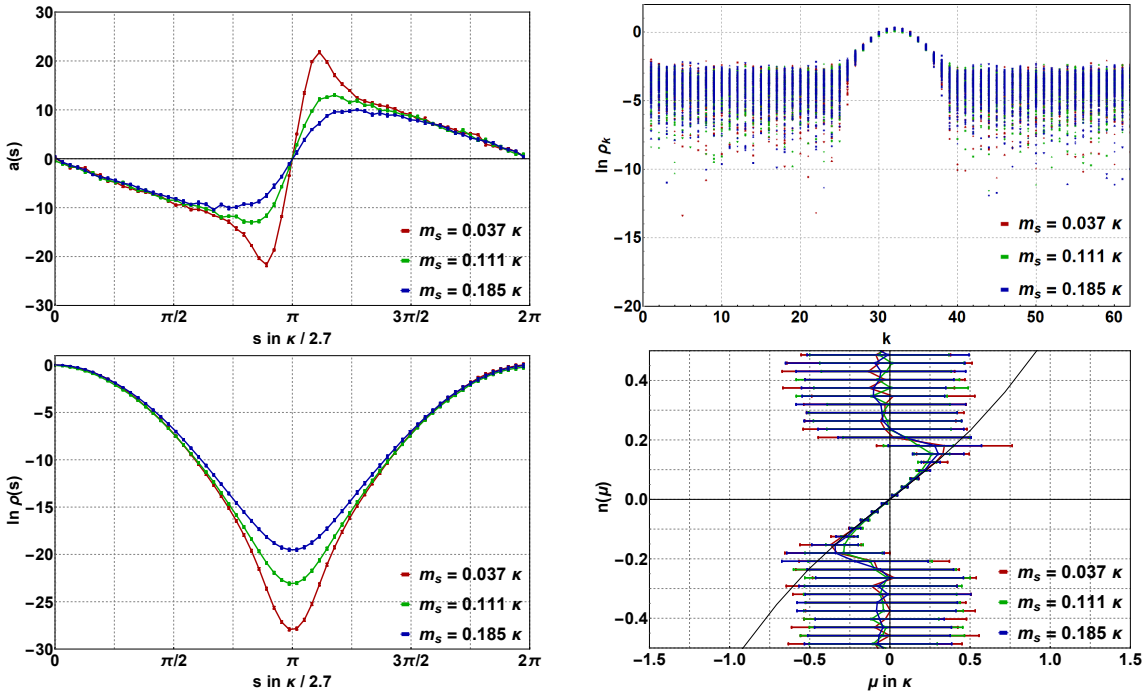

Figure 5.4.: The logarithmic slopes $a(s)$ obtained via LLR *(left, top)*, the corresponding logarithmic gDOS $\ln \rho(s)$ *(left, bottom)*, their discrete Fourier transform $\ln \rho_k$ *(right, top)* and the particle densities obtained via eq. 2.63 *(right, bottom)* for three different choices of staggered mass m_s on a $N_c = 6^2$, $N_t = 6$ lattice at $\beta = 2.7\kappa^{-1}$ and $U = 0.1\kappa$. The black line in the plot of the particle density $n(\mu)$ shows the pure tight-binding density.

5.2.2. Euclidean-time discretization δ_τ

For investigating the δ_τ-dependence we also carried out simulations for three different values of $N_t \in \{6, 12, 18\}$ in a fixed parameter set ($N_c = 6, m_s = 0.185\,\kappa, \beta = 2.7\,\kappa, U = 1.0\,\kappa$) with 120 sampling points. Figure 5.5 shows the results for these simulations and the corresponding $\ln \rho_(s), \ln \rho_k$ and $n(\mu)$. We find that the Euclidean-time discretization has only minor influence that vanishes within the error bars for $a(s)$. Only in $\ln \rho(s)$ we find small differences in the middle of the period, which are in the strongly suppressed area, as it is with the staggered mass. These differences can not be resolved in the corresponding Fourier coefficients and thus in the particle density $n(\mu)$. Additionally we find that the particle density for $U = 1.0\kappa$ fully agrees with the non-interacting theory within the resolvable area when the linear term is dropped. So, we can here also use a more rough discretization for further studies and save computational time, as we do with staggered mass.

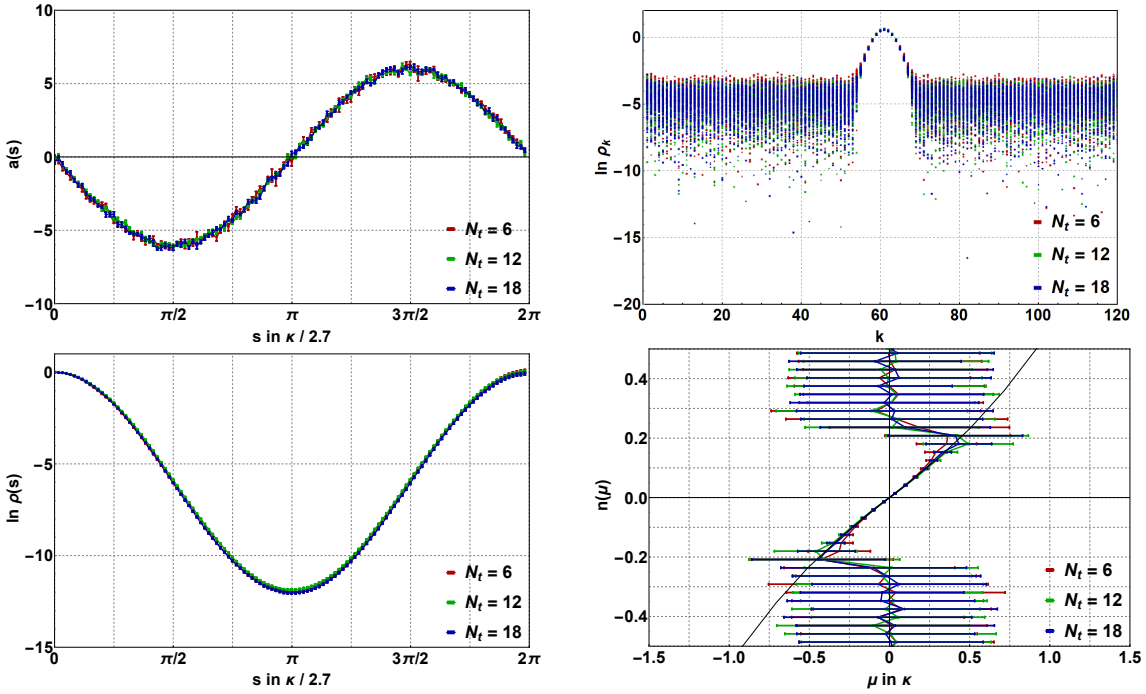

Figure 5.5.: The logarithmic slopes $a(s)$ obtained via LLR *(left, top)*, the corresponding logarithmic gDOS $\ln \rho(s)$ *(left, bottom)*, their discrete Fourier transform $\ln \rho_k$ *(right, top)* and the particle densities obtained via eq. 2.63 *(right, bottom)* for three different choices of N_t on a $N_c = 6^2$ lattice at $\beta = 2.7\kappa^{-1}, m_s = 0.185\kappa$ and $U = 1.0\kappa$. The black line in the plot of the particle density $n(\mu)$ shows the pure tight-binding density.

Furthermore, it should be mentioned that this weak dependance on the lattice discretization can be traced back to the structure of the fermion matrix, more specifically on the compact Hubbard field which was introduced in section 2.3.1. In testing

cases without compact Hubbard field we already found a strong dependance of the Euclidean-time Discretization up to $N_t = 768$ in Mean field calculations [122].

5.2.3. On-site potential and finite volume

Here we present results for five different on-site potential values for a $N_c = 6^2$, $N_t = 6$ lattice in Figure 5.6 and two different values for a $N_c = 12^2$, $N_t = 12$ lattice in Figure 5.7. As in previous sections we find the largest deviations in the middle of the period on the level of the logarithmic slope. Additionally, we can describe a general trend in the way that with increasing interaction strength the range of a(s) and therefore also $\ln \rho(s)$ becomes smaller and smaller. This behavior makes simulations for strong couplings more expensive, since one has to measure deviations from zero very precisely. This effect comes in addition to HMC behavior which also gets more expensive with increasing U. We have found that the logarithmic slope for $U = 5.0\kappa$ can no longer be distinguished from zero within the error bars for a simulation series with a total of around 15000 GPU hours.

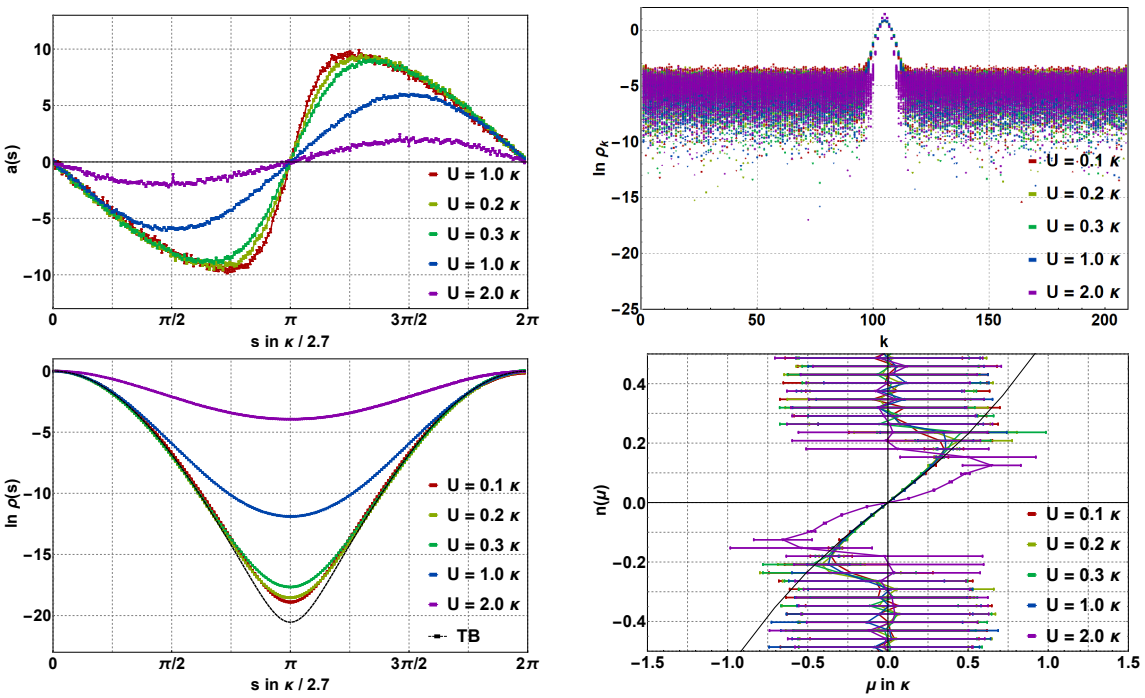

Figure 5.6.: The logarithmic slopes $a(s)$ obtained via LLR *(left, top)*, the corresponding logarithmic gDOS $\ln \rho(s)$ *(left, bottom)*, their discrete Fourier transform $\ln \rho_k$ *(right, top)* and the particle densities obtained via eq. 2.63 *(right, bottom)* for five different choices of One site potential U on a $N_c 6^2$, $N_t = 6$ lattice at $\beta = 2.7\kappa^{-1}$ and $m_s = 0.185\kappa$. The black line in the plot of the particle density $n(\mu)$ shows the pure tight-binding density.

As we show in Figures 5.6 and 5.7 we find that the Fourier modes and the particle density for $U \leq 1$ agrees with the pure tight-binding theory within the error bars

up to the linear term, whereas for $U = 2.0$ a deviation is visible. Furthermore, we find, as one would expect, that the sign problem sets in at much smaller μ for the larger system. For the $N_c = 6^2$, $N_t = 6$ we can compute $n(\mu)$ up to $\mu \approx 0.35\kappa$ for $U \leq 1.0\kappa$. In the larger lattice $N_c = 12^2$, $N_t = 12$ case we only reach $\mu \approx 0.1\kappa$ for the same potential. It should be mentioned, that the measured amplitudes of $a(s)$ are larger in the larger lattice for the same parameter set, which makes it easier to find a signal for stronger couplings. It can be concluded that we can still find a signal for larger lattices at higher potential values as long as we can perform HMC updates with reasonable acceptance rates. However, an exact measurement of this effect was not possible in this thesis due to the limited computing capacity.

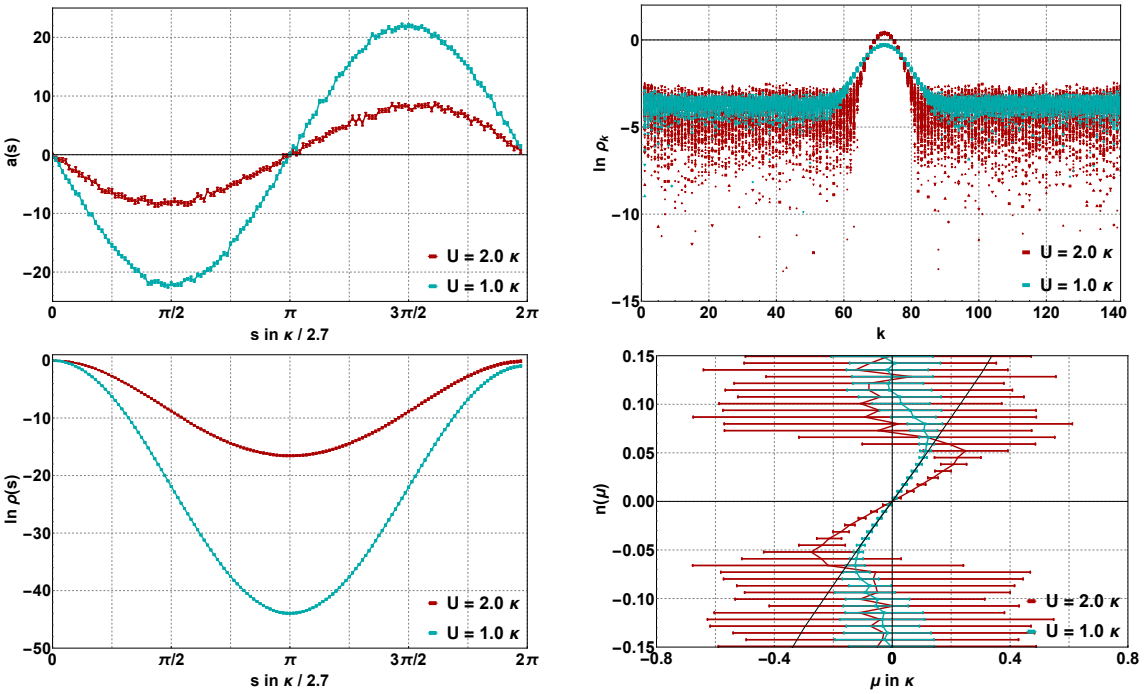

Figure 5.7.: The logarithmic slopes $a(s)$ obtained via LLR *(left, top)*, the corresponding logarithmic gDOS $\ln \rho(s)$ *(left, bottom)*, their discrete Fourier transform $\ln \rho_k$ *(right, top)* and the particle densities obtained via eq. 2.63 *(right, bottom)* for five different choices of on-site potential U on a $N_c = 12^2$, $N_t = 12$ lattice at $\beta = 2.7\kappa^{-1}$ and $m_s = 0.185\kappa$. The black line in the plot of the particle density $n(\mu)$ shows the pure tight-binding density.

5.3. Results from compressed sensing

As mentioned in section 2.4.3 an attempt to improve the results from LLR algorithm is to use fit functions for $\ln \rho(s)$ to generate further data points in between of two supporting points s_n. This method is called compressed sensing within the LLR literature. In order to get an impression of the amount of improvement of this method within our framework we have used compressed sensing for the data sets with varying one site potential. First, we present the simple attempt in which we fit the generalized density of states with a Fourier series to generate new and denser set of data and transform these set afterwards to obtain the particle density. For this purpose, we use the maximum number of fit parameters which are possible for each data set. The second attempt is to use Chebyshev polynomials of the first kind instead, where we add higher terms until the expansion converges to a final result and then use this fit for the further evaluation. In Figure 5.8 the results of this methodology are presented for the exemplary case ($N_c = 6^2$, $N_t = 6$, $\beta = 2.7\kappa^{-}1$, $m_s = 0.185\kappa$, $U = 1.0\kappa$) and compared with the results without compressed sensing for both mentioned sets of functions. In both cases, we generated data sets with factor 10 more data points as in the data set obtained from simulations. Since the results change not significantly for the other sets of parameters their plots can be found in the Appendix C. We find a very small improvement of about two data points for each data set before the results scatter in an uncontrolled way, whether we use Fourier or Chebychev fits. So we can conclude that the more detailed structure of the generalized density can only very roughly be reproduced in both cases and higher coefficients play a major role for advancing the higher μ-area.

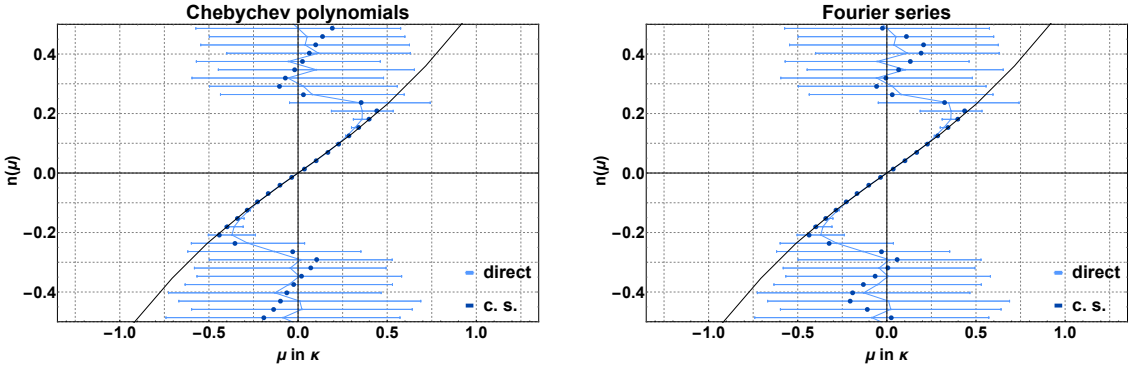

Figure 5.8.: Comparison of obtaining the particle density for an exemplary data set ($N_c = 6^2$, $N_t = 6$, $\beta = 2.7\kappa^{-}1$, $m_s = 0.185\kappa$, $U = 1.0\kappa$) direct with the HMC data and via compressed sensing by Fourier series with N_s coefficients [*right*] and by Chebychev polynomials of the first kind with $N_s/4$ coefficients [*left*]. In both variants the number of sample points were increased by factor 10 through compressed sensing.

5.4. Comparison to Brute-Force method

Here we present an overall comparison of the regions in which we can obtain results for the particle density via brute force reweighting with the results produced with the LLR-framework and and subsequent evaluation by canonical ensembles. Figure 5.9 shows this comparison of the results as a function of on-site potential U for the two chosen lattice sizes. In both cases, we plot the value where the signal is lost while spending roughly the same computer time for each pair of data. We have found an improvement over brute-force reweighting in all cases. However, the advantage of our framework becomes much smaller with larger lattices. But a principal advantage is that the improvement becomes better with increasing interaction strength. This advantage only holds as long as we can sample the logarithmic slope, of course. As already mentioned, the signal was lost at about $U = 5.0\,\kappa$

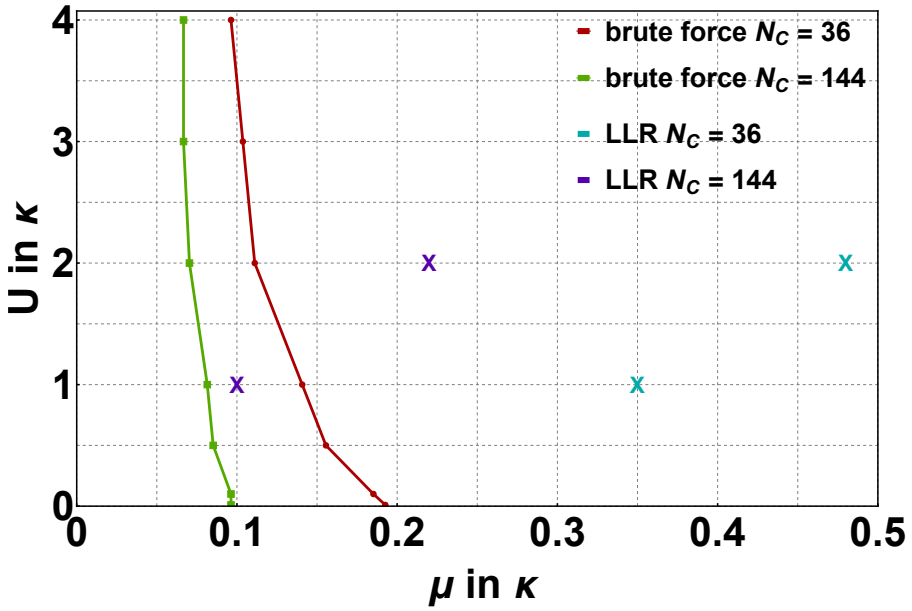

Figure 5.9.: Comparison of effective μ-range of brute-fore reweighting and LLR for $N_x = N_y = N_t = 6$ and 12 lattices at $\beta = 2.7\kappa^{-1}$ and $m_s = 0.185\kappa$. For each value of U the phase distribution was measured according to eq. 3.8 until the signal was lost. A roughly equal amount of computer time was spent for corresponding LLR calculations.

5.5. Summary

For simulating with charge chemical potential directly, we used the Linear Logarithmic Relaxation method in combination with the Hybrid-Monte-Carlo algorithm as update-mechanism to obtain a generalized density of states with very high precision in order to use this data to reconstruct the particle density by differences of pseudo-canonical ensembles. For the sake of simplicity we used the pure Hubbard model instead of the partially screened Coulomb interaction used in chapter 4. Similar to the spin-dependent part, we used the tight-binding theory as a baseline for comparison with the interacting theory. Introductory, we provided a first understanding of advantages and disadvantages of the method by discussing an example case. We showed that we can measure the periodic gDOS of the average Hubbard field very precise via integrating the obtained logarithmic slope, which was estimated at a chosen set of support points. However, our simple way of extracting the complex phase from the fermion determinant in the partition function is for the price of a highly oscillating contribution which we tried to handle by Fourier transformation. As shown in chapter 2 the partition function represented as Fourier coefficients of the gDOS can be seen as the fugacity expansion and therefore we can estimate the chemical potential as derivative of the identified pseudo-canonical ensembles with particle number modulo total of sample points. The particle density was then obtained by inversion of the differences of chemical potentials of these ensembles.
We showed that the Euclidean-time discretization and the staggered mass have no major influence for our chosen set of parameters. Furthermore, we find that our method reproduces the tight-binding case for small interaction strengths and reaches up factor 4 farther in μ than brute-force reweighting. This factor becomes smaller for larger lattice sizes and lower temperatures, but works in all considered cases better than the brute-force method. For increasing interaction strength the gain from the method gets better as long as the logarithmic slope is measurable. In order to improve the results we applied two different kinds of compressed sensing, but achieved only little enhancement of the available range by that.
In summary we can state that our approach works well for the chosen set of parameters, but there is space for improvements. Especially our way of shifting the chemical potential in the Hubbard field and by that generating a periodic gDOS with the average Hubbard field as an observable limits the improvements of the LLR method in which typically non-compact, so-called "extended" density of states should be considered. For further investigations there are two obvious ways which can lead to better results. The first is to find a formulation of the partition function which contains such an extended generalized density of states, the second is to improve the way of reconstructing the particle density out of the highly oscillating integral representation.

6. Conclusion and Outlook

In this work two possible options to deal with the fermion sign problem arising from complex contributions to probability weights in Quantum Monte-Carlo simulations were studied for the 2d-hexagonal graphene lattice with the Hybrid-Monte-Carlo framework. The first strategy was to use the analogy between the charge and spin-dependent chemical potential which arises from the particle-hole symmetry in the nearest-neighbor representation of tight-binding theory, which is applicable due to strong electron coupling in graphene. The major goal of this part was to study the implications of a realistic long-range potential, which accounts for the screening from lower σ-band electrons on the band structure. As an example for interesting physics away from the Dirac cone we focused on the neck disrupting Lifshitz transition, which is indicated by a logarithmic divergence in the density of states and corresponding quantities and takes place at the van Hove singularity located at the M-points in the band structure. Unlike other examples of analogue theories, the spin-dependent chemical potential in our formulation plays a physical role on its own as it describes an in-plane magnetic field which leads to a Zeeman splitting of the electron spins. Within this investigation we used the Thomas-Fermi susceptibility as an observable for HMC and outlined the connection between this measurable quantity and the density of states and derived necessary approximations for comparing pure tight-binding theory with interacting system in an adequate way. We showed that our simulations are in line with experimental results [41,120,123]. We have found a bandwidth renormalization through many-body interactions in a way that the whole band seems to get squeezed so that the valence band ends already at around $\mu \approx 2.25\kappa$. Furthermore, we found evidence that the neck-disrupting Lifshitz transition, indicated by a logarithmic divergence of the van Hove peak, turns into a true quantum phase transition at an inverse temperature $\beta_c = 16(2)\,\kappa$. Additionally, we showed that the scaling exponent $\gamma = 0.52(6)$ indicates an extended van Hove singularity around the M-point. Besides the peak building around the van Hove singularity we find another peak forming at the upper end of the valence band. This second peak could be subject of further investigations and since a second topological transition can be found at the Γ-point one might find a similar case to the one at the van Hove singularity.
The second approach was to remove the chemical potential from the fermion matrix by absorbing into Hubbard field and use the Linear-Logarithmic-Relaxation technique to sample the logarithmic derivative of generalized density of states, which then was

used to obtain the particle density directly via differences of pseudo-canonical ensembles which can be written as the Fourier coefficients of the generalized density of states. In order to keep the system simple we decided to use only an on-site Hubbard interaction instead of partially screened long-range interaction here. As in the first case we used the pure tight-binding formulation for comparison and showed that we find an overall gain from this method of about 4 for $N_c = 6^2$, $N_t = 6$ in comparison with brute-force reweighting in the weakly interacting area. Unfortunately, this gain becomes smaller when the spatial volume is increased or the temperature is lowered. Nevertheless, we found in all examples studied an improvement by the method against pure brute-force reweighting and we could show that the improvement gets better with increasing interaction strength. While the brute-force method becomes worse and worse, we find the our method is becoming better as long as a signal is measurable. We found for $U = 5.0\,\kappa$ no measurable signal anymore in a simulation with 15000 GPU hours. Since all the other results were done with a total amount of 26000 GPU hours on GTX 980ti GPUs, we can conclude on the one hand that without further developments this lost-signal limit will be hard to cross, but on the other hand the amount of computational time spent on the other results leaves much space for larger-scale projects. In our view, the precision of $ln(\rho)$ could be increased by at least an order of magnitude by using the most modern hardware and improved linear algebra libraries. Furthermore, the whole method could be more effective by using BSS Monte-Carlo which was found to be superior to the HMC in the pure Hubbard model. Overall, our investigations should be seen as a proof of principle study, which leaves also the space for further theoretical improvements for example in the area of compressed sensing, where advanced techniques was already proposed, for example in [72]. Another possible way for improvements could be a combination of Lefshetz thimble, which was applied recently on Hubbard models [124] and the LLR-framework. Such an hybrid attempt could be formulated in a way that the Lefshetz thimble decomposition is directly applied on eq. 2.54 in order to get rid of the reconstruction scheme and by this obtain a more precise signal for the particle density $n(\mu)$. Finally, it should be mentioned, that the transferability to other theories is rather limited, since the formulation used in this work is based on the possibility to separate the chemical potential from the fermion matrix via absorbing it in the Hubbard field. By this reformulation, one has to determine only one but unfortunately intensive generalized density of states via simulations and one can obtain results for each chosen chemical potential, afterwards.

A. Calculations within pure Tight-Binding theory

Here the detailed calculations within the pure tight-binding theory are presented according to [2].

Thomas-Fermi Susceptibility

Starting from the Lindhard function

$$\chi_\mu = \lim_{\vec{p}\to 0} \lim_{\vec{\omega}\to 0} \Pi(\omega, \vec{p}, \mu) \tag{A.1}$$

with

$$\begin{aligned}\Pi(\omega, \vec{p}, \mu) = -2 \int_{1.BZ} \frac{d^2k}{4\pi^2} \sum_{s,s'=\pm 1} \left(1 + ss' \frac{\vec{b}_k \cdot \vec{b}_{k+p} + m^2}{\epsilon_{\vec{k}} \epsilon_{\vec{k}+\vec{p}}}\right) \\ \cdot \frac{f\left(\frac{s'\epsilon_{\vec{k}+\vec{p}} - \mu}{T}\right) - f\left(\frac{s\epsilon_{\vec{k}} - \mu}{T}\right)}{s'\epsilon_{\vec{k}+\vec{p}} - s\epsilon_{\vec{k}} - \omega - i\epsilon}\end{aligned} \tag{A.2}$$

and taking the limits, only $s = s'$ terms are left, which can be interpreted as derivatives of ϵ. With the Fermi function

$$f(x) = \frac{1}{1 + e^x} \tag{A.3}$$

we find

$$\begin{aligned}\chi(\mu) &= -2A_c \int_{1.BZ} \frac{d^2k}{4\pi^2} \frac{d}{d\epsilon} \left[\frac{1}{1 + \exp\left\{\frac{-\epsilon_{\vec{k}} - \mu}{T}\right\}} + \frac{1}{1 + \exp\left\{\frac{\epsilon_{\vec{k}} - \mu}{T}\right\}}\right] \\ &= -\frac{2A_c}{T} \int_{1.BZ} \frac{d^2k}{4\pi^2} \left[\frac{\exp\left\{\frac{-\epsilon_{\vec{k}} - \mu}{T}\right\}}{\left(1 + \exp\left\{\frac{-\epsilon_{\vec{k}} - \mu}{T}\right\}\right)^2} - \frac{\exp\left\{\frac{\epsilon_{\vec{k}} - \mu}{T}\right\}}{\left(1 + \exp\left\{\frac{\epsilon_{\vec{k}} - \mu}{T}\right\}\right)^2}\right]\end{aligned} \tag{A.4}$$

with

$$\operatorname{sech}(x) = \frac{1}{\cosh(x)} = \frac{2}{e^x + e^{-x}} \tag{A.5}$$

follows

$$\chi(\mu) = \frac{A_c}{2T} \int_{1.BZ} \frac{d^2k}{4\pi^2} \left[\operatorname{sech}^2 \left(\frac{\mu - \epsilon_{\vec{k}}}{2T} \right) + \operatorname{sech}^2 \left(\frac{\mu + \epsilon_{\vec{k}}}{2T} \right) \right] . \tag{A.6}$$

Behavior at the VHS

Starting from eq. A.6, we find via inserting unity as an integral over a delta distribution

$$\chi(\mu) = \frac{A_c}{2T} \int_{1.BZ} \frac{d^2k}{4\pi^2} \int_0^{3\kappa} d\epsilon \, \delta(\epsilon - E_{\vec{k}}) \left[\operatorname{sech}^2 \left(\frac{\mu - \epsilon}{2T} \right) + \operatorname{sech}^2 \left(\frac{\mu + \epsilon}{2T} \right) \right] \tag{A.7}$$

By solving the integral in momentum space we find with

$$g_c A_c \int_{1.BZ} \frac{d^2k}{4\pi^2} \delta(\epsilon - E_{\vec{k}}) = \rho(\epsilon) \tag{A.8}$$

a relation between $\chi(\mu)$ and the density of states $\rho(\epsilon)$ (see eq. 2.10)

$$\chi(\mu) = \frac{1}{4T} \int_0^{3\kappa} d\epsilon \, \rho(\epsilon) \left[\operatorname{sech}^2 \left(\frac{\mu - \epsilon}{2T} \right) + \operatorname{sech}^2 \left(\frac{\mu + \epsilon}{2T} \right) \right] . \tag{A.9}$$

By writing $x = \frac{\epsilon}{\kappa}$ and therefore $d\epsilon = \frac{1}{\kappa} dx$ we find

$$\begin{aligned} \chi(\mu) = \frac{1}{\pi^2 T} \int_0^3 dx \, \frac{x}{\sqrt{Z_0}} F \left(\frac{\pi}{2}, \frac{Z1}{Z0} \right) \\ \left[\operatorname{sech}^2 \left(\frac{\kappa \left(\frac{\mu}{\kappa} - x \right)}{2T} \right) + \operatorname{sech}^2 \left(\frac{\kappa \left(\frac{\mu}{\kappa} + x \right)}{2T} \right) \right] \end{aligned} \tag{A.10}$$

By taking Taylor series of $F\left(\frac{\pi}{2}, a\right)$ and Z_0 of zero order and $a = \frac{Z1}{Z0}$ up to third order around $a = 1$ or rather $x = 1$ we find

$$\begin{aligned} F\left(\frac{\pi}{2}, a\right) &\approx 2\ln 2 - \frac{1}{2} \ln (a - 1) \\ \frac{Z_1}{Z_0} &\approx 1 - \frac{1}{4} (x - 1)^3 \\ Z_0 &\approx 4 \end{aligned} \tag{A.11}$$

and $\operatorname{sech}^2 \left(\frac{\kappa \left(\frac{\mu}{\kappa} + x \right)}{2T} \right)$ vanishes. So the susceptibility can be written as

$$\chi(\mu) = \frac{1}{2\pi^2 T} \int_0^3 dx \, \left(2\ln 2 - \frac{1}{2} \ln \left(\frac{1}{4} (x - 1)^3 \right) \right) \operatorname{sech}^2 \left(\frac{\kappa \left(\frac{\mu}{\kappa} - x \right)}{2T} \right) . \tag{A.12}$$

Now we set $\mu = \kappa$ and extend the integration limits to infinity, what is possible since

$\mathrm{sech}(x)$ is highly localized. Thus we find

$$\chi_{max} = \frac{3}{2\pi^2 T} \int_{-\infty}^{\infty} dx \left(\ln 2 - \frac{1}{2} \ln (x-1) \right) \mathrm{sech}^2 \left(\frac{\kappa}{2T} (x-1) \right) \tag{A.13}$$

and by carrying out the integration we finally find

$$\chi_{max} = \frac{3}{\kappa \pi^2} \left(3 \ln 2 + \gamma_E + \ln \frac{\kappa}{\pi} - \ln T + \mathcal{O}(T) \right) \tag{A.14}$$

with γ_E as Euler-Mascheroni constant.

B. Calculations within the LLR formulation

Here we present the detailed calculations done within the LLR-framework.

Generalized density of states

Starting with

$$Z = \int \mathcal{D}\phi \ \det M(\phi,\mu) \det M^\dagger(\phi,-\mu) \exp\left\{-\frac{\delta}{2U}\sum_{x,t}\phi_{x,t}^2\right\} \tag{B.1}$$

and by shifting $\phi_{x,t} \to \phi_{x,t} - i\mu$ we find

$$Z = \int \mathcal{D}\phi \ \det M(\phi) \det M^\dagger(\phi) \exp\left\{-\frac{\delta}{2U}\sum_{x,t}(\phi_{x,t} - i\mu)^2\right\} \tag{B.2}$$

and thus

$$Z = \int \mathcal{D}\phi \ \det M(\phi) \det M^\dagger(\phi) \exp\left\{-\frac{\delta}{2U}\sum_{x,t}\phi_{x,t}^2 + i\frac{\mu\delta}{U}\sum_{x,t}\phi_{x,t} + i\frac{V\delta}{2U}\mu^2\right\} . \tag{B.3}$$

By completing the square

$$Z = \int \mathcal{D}\phi \ \det M(\phi) \det M^\dagger(\phi) \exp\left\{-\frac{\delta}{2U}\sum_{x,t}\phi_{x,t}^2 + i\frac{\mu\delta}{U}\sum_{x,t}\phi_{x,t} + \frac{\delta}{2UV}\left[\sum_{x,t}\phi_{x,t}\right]^2 - \frac{\delta}{2UV}\left[\sum_{x,t}\phi_{x,t}\right]^2 + i\frac{V\delta}{2U}\mu^2\right\}$$

we can write

$$Z = \int \mathcal{D}\phi \ \det M(\phi) \det M^\dagger(\phi) \exp\left\{-\frac{\delta}{2U}\left(\sum_{x,t}\phi_{x,t}^2 - \frac{1}{V}\left[\sum_{x,t}\phi_{x,t}\right]^2\right) - \frac{\delta}{2UV}\left[\sum_{x,t}\phi_{x,t}\right]^2 + i\frac{\mu\delta}{U}\sum_{x,t}\phi_{x,t} + i\frac{V\delta}{2U}\mu^2\right\} .$$

Then we introduce the average Hubbard field

$$\Phi = \frac{1}{V}\sum_{x,t}\phi_{x,t} \tag{B.4}$$

and get

$$Z = \int \mathcal{D}\phi \ \det M(\phi)\det M^{\dagger}(\phi)\exp\left\{-\frac{\delta}{2U}\left(\sum_{x,t}\phi_{x,t}^2 - V\Phi^2\right)\right. \\ \left. -\left(\frac{\delta V}{2U}\Phi^2 - i\frac{\mu\delta V}{U}\Phi - i\frac{V\delta}{2U}\mu^2\right)\right\} \ ,$$

again we complete the square

$$Z = \int \mathcal{D}\phi \ \det M(\phi)\det M^{\dagger}(\phi)\exp\left\{-\frac{\delta}{2U}\left(\sum_{x,t}\phi_{x,t}^2 - 2V\Phi^2 + V\Phi^2\right)\right. \\ \left. -\frac{\delta V}{2U}\left(\Phi - i\mu\right)^2\right\}$$

and use eq. B.4 we find

$$Z = \int \mathcal{D}\phi \ \det M(\phi)\det M^{\dagger}(\phi)\exp\left\{-\frac{\delta}{2U}\left(\sum_{x,t}\phi_{x,t}^2 - 2\Phi\sum_{x,t}\phi_{x,t} + \Phi^2\sum_{x,t}1\right)\right. \\ \left. -\frac{\delta V}{2U}\left(\Phi - i\mu\right)^2\right\} \ ,$$

and finally

$$Z = \int \mathcal{D}\phi \ \det M(\phi)\det M^{\dagger}(\phi)\exp\left\{-\frac{\delta}{2U}\sum_{x,t}\left(\phi_{x,t} - \Phi\right)^2 - \frac{\delta V}{2U}\left(\Phi - i\mu\right)^2\right\} \ . \tag{B.5}$$

Now we can introduce the generalized density of states $\rho(s)$ as

$$\rho(s) = \int D\phi \left|\det M(\phi,0)\right|^2 \delta(\Phi - s)\exp\left\{-\frac{\delta_\tau}{2U}\sum_{x,t}\left(\phi_{x,t} - s\right)^2\right\} \tag{B.6}$$

and by that write the partition function as

$$Z(\mu) = \int ds\rho(s)\exp\left\{-\frac{\delta_\tau V}{2U}\left(s - i\mu\right)^2\right\} \ . \tag{B.7}$$

Periodicity of $\rho(s)$

The periodicity of the gDOS is determined by the periodicity of the fermion determinant. Here we explicitly calculate the fermion determinant for a system with no tight-binding interactions. We start with writing the fermion operator as

$$\begin{aligned} M(\phi)_{(x,t),(x',t')} =& \delta_{x,x'} \left[\delta_{t,t'} \exp\left(i \, \frac{\beta}{N_t} \, \phi_{x,t} \right) - \delta_{t+1,t'} \left(1 + \frac{m_s \, \beta}{N_t} \right) \right] \\ & - \kappa \frac{\beta}{N_t} \sum_{\vec{n}} \delta_{x+\vec{n},x'} \, \delta_{t+1,t'} \end{aligned} \tag{B.8}$$

respectively

$$\begin{aligned} M^\dagger(\phi)_{(x,t),(x',t')} =& \delta_{x,x'} \left[\delta_{t,t'} \exp\left(-i \, \frac{\beta}{N_t} \, \phi_{x,t} \right) - \delta_{t-1,t'} \left(1 + \frac{m_s \, \beta}{N_t} \right) \right] \\ & - \kappa \frac{\beta}{N_t} \sum_{\vec{n}} \delta_{x+\vec{n},x'} \, \delta_{t-1,t'} \end{aligned} \tag{B.9}$$

which are also a possible representations of M.The periodicity of $|MM^\dagger|$ is then determined by the main-diagonal of the matrix. We now set, $\delta = \frac{\beta}{N_t}$ and $\delta_{m_s} = \delta \, m_s$ and ignoring the tight-binding part ($\kappa = 0$). By this we get for every $x = x'$ the following time-matrix

$$N_x = \begin{pmatrix} e^{i\,\delta\,\phi_{x,1}} & -1-\delta_{m_s} & 0 & 0 & 0 & 0 \\ 0 & e^{i\,\delta\,\phi_{x,2}} & -1-\delta_{m_s} & 0 & 0 & 0 \\ 0 & 0 & \ddots & \ddots & 0 & 0 \\ 0 & 0 & 0 & \ddots & \ddots & 0 \\ 0 & 0 & 0 & 0 & e^{i\,\delta\,\phi_{x,N_t-1}} & -1-\delta_{m_s} \\ 1+\delta_{m_s} & 0 & 0 & 0 & 0 & e^{i\,\delta\,\phi_{x,N_t}} \end{pmatrix} \tag{B.10}$$

and thus

$$\begin{aligned} \det NN^\dagger =& 1 + (1+\delta_{m_s})^{2\,N_t} + (1+\delta_{m_s})^{N_t} \left(e^{-i\,\delta\,\sum_{t=1}^{N_t} \phi_{x,t}} + e^{i\,\delta\,\sum_{t=1}^{N_t} \phi_{x,t}} \right) \\ =& 1 + (1+\delta_{m_s})^{2\,N_t} + (1+\delta_{m_s})^{N_t} \left(e^{-i\,\beta\bar{\phi}_x} + e^{i\,\beta\bar{\phi}_x} \right) \end{aligned} \tag{B.11}$$

Assuming $N_t \gg 1$ and using

$$\lim_{x\to\infty} \left(1 + \frac{a}{x} \right)^x = e^a \tag{B.12}$$

we get the following approximation:

$$\det NN^\dagger \approx \; 1 + e^{2\,\beta\,m_s} + 2\,e^{\beta\,m_s} \cos\beta\bar{\phi} \tag{B.13}$$

Setting $m_s \to 0$

$$\det NN^\dagger \approx\ 2 + 2\cos\beta\bar{\phi} \tag{B.14}$$

and $V_{sp} = 2\,N_x\,N_y$, the matrix M can be written as

$$M = \begin{pmatrix} N_1 & 0 & 0 & 0 & 0 & 0 \\ 0 & N_2 & 0 & 0 & 0 & 0 \\ 0 & 0 & \ddots & 0 & 0 & 0 \\ 0 & 0 & 0 & \ddots & 0 & 0 \\ 0 & 0 & 0 & 0 & \ddots & 0 \\ 0 & 0 & 0 & 0 & 0 & N_{V_{sp}} \end{pmatrix} \tag{B.15}$$

by that the related determinant is

$$\det MM^\dagger = \prod_x^{V_{sp}} \det NN^\dagger(\bar{\phi}_x) = 2^{V_{sp}} \prod_x^{V_{sp}} (\cos\beta\,\bar{\phi}_x + 1) \tag{B.16}$$

C. Additional plots from compressed sensing

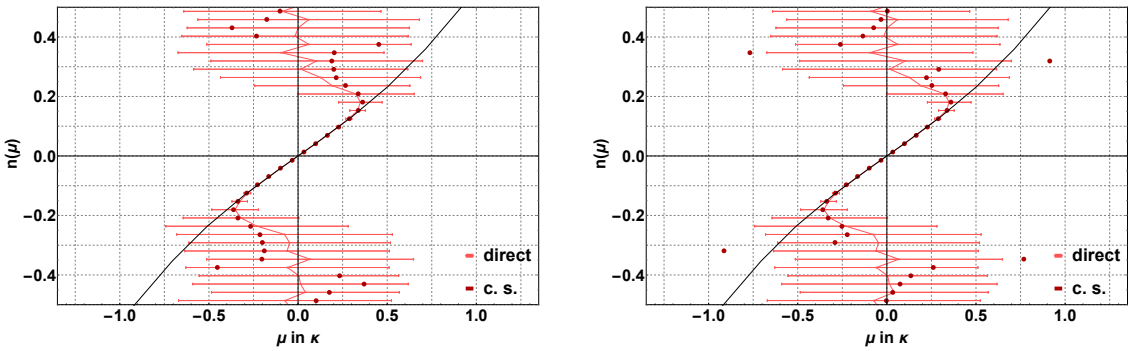

Figure C.1.: Comparison of obtaining the particle density for the data set $N_c = 6^2$, $N_t = 6$, $\beta = 2.7\kappa^{-}1$, $m_s = 0.185\kappa$, $U = 0.1\kappa$ direct with the HMC data and via compressed sensing by Fourier series with N_s coefficients [*right*] and by Chebychev polynomials of the first kind with $N_s/4$ coefficients [*left*]. In both variants the number of sample points were increased by factor 10 through compressed sensing.

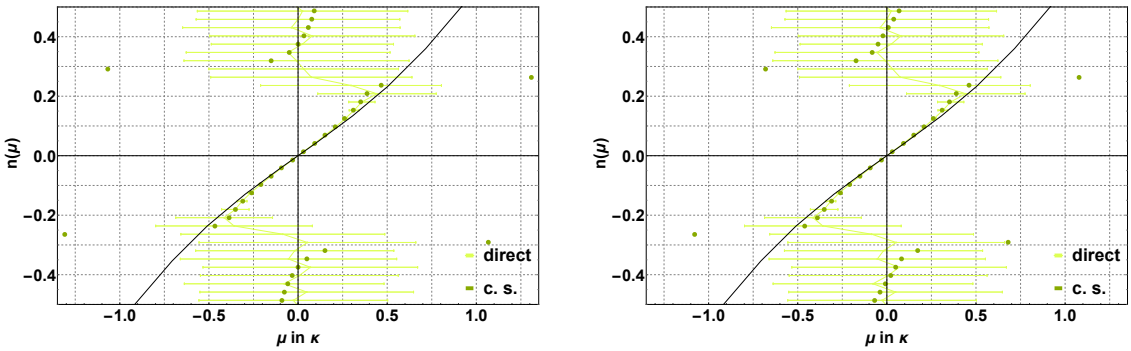

Figure C.2.: Comparison of obtaining the particle density for the data set $N_c = 6^2$, $N_t = 6$, $\beta = 2.7\kappa^{-}1$, $m_s = 0.185\kappa$, $U = 0.2\kappa$ direct with the HMC data and via compressed sensing by Fourier series with N_s coefficients [*right*] and by Chebychev polynomials of the first kind with $N_s/4$ coefficients [*left*]. In both variants the number of sample points were increased by factor 10 through compressed sensing.

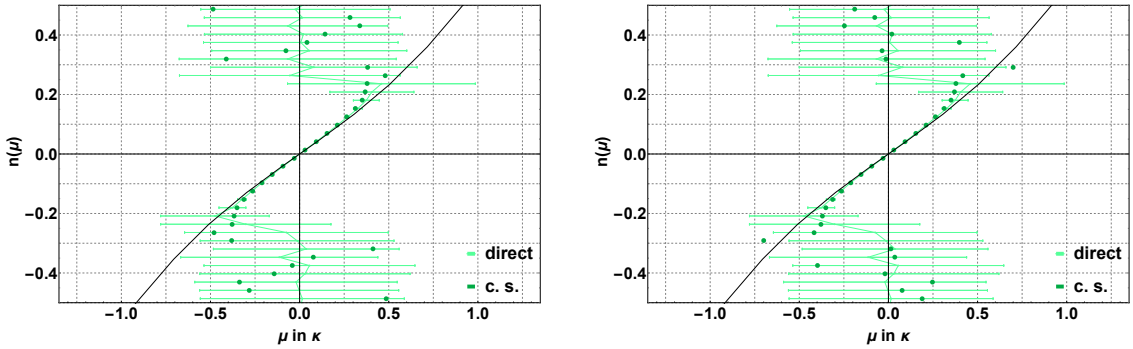

Figure C.3.: Comparison of obtaining the particle density for the data set $N_c = 6^2$, $N_t = 6$, $\beta = 2.7\kappa^{-}1$, $m_s = 0.185\kappa$, $U = 0.3\kappa$ direct with the HMC data and via compressed sensing by Fourier series with N_s coefficients [*right*] and by Chebychev polynomials of the first kind with $N_s/4$ coefficients [*left*]. In both variants the number of sample points were increased by factor 10 through compressed sensing.

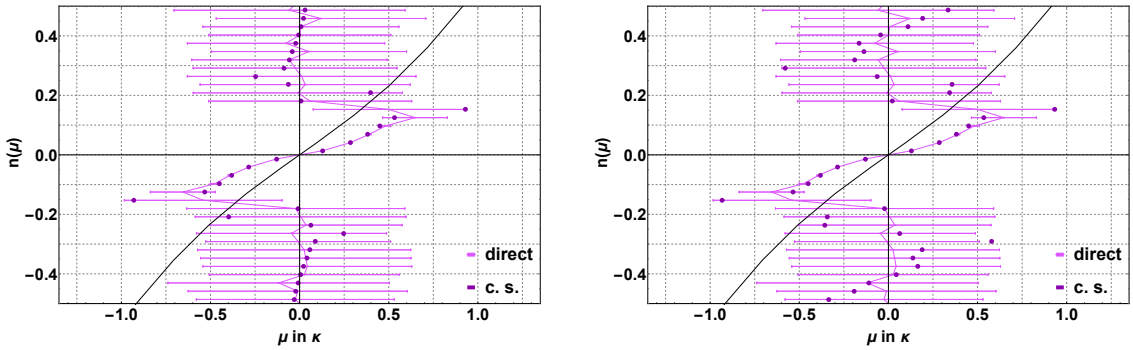

Figure C.4.: Comparison of obtaining the particle density for the data set $N_c = 6^2$, $N_t = 6$, $\beta = 2.7\kappa^{-}1$, $m_s = 0.185\kappa$, $U = 2.0\kappa$ direct with the HMC data and via compressed sensing by Fourier series with N_s coefficients [*right*] and by Chebychev polynomials of the first kind with $N_s/4$ coefficients [*left*]. In both variants the number of sample points were increased by factor 10 through compressed sensing.

D. Simulation parameters - spin-dependent chemical potential

Here we list the sets of parameters which were used for simulations in context of spin-dependent chemical potential. The number of termalization steps was ≤ 10 in all simulations and we used 500 noisy estimator sources for measuring the observable. Besides the physical parameters one can also find the important simulation parameters in the respective tables. These parameters are the total number of updates, the measure frequency (meaning that at every x step a measurement was done), the number of Leapfrog steps and the size of one step. The parameters for simulations dealing with different staggered mass is shown in Table D.1, for different temperatures in Table D.2, for different lattice discretizations and interaction strengths in Table D.3. The simulation parameters for investigations around the VHS are shown in Table D.4 for infinite volume limits and the executed simulations for the summation method in Table D.5.

β in κ^{-1}	N_c, N_t	m_s in κ	μ-range in κ	no. up.	m. freq.	step n.	stepsize
5.40	12^2, 12	0.185	$0.0 - 3.0$	600	3	600	0.5
5.40	12^2, 12	0.111	$0.0 - 3.0$	300	3	1000	0.3
5.40	12^2, 12	0.037	$0.0 - 3.0$	300	3	1500	0.2

Table D.1.: Parameter overview of executed simulations for section 4.1.1.

β in κ^{-1}	N_c, N_t	m_s in κ	μ-range in κ	no. up.	m. freq.	step n.	stepsize
5.40	12^2, 12	0.185	$0.0 - 3.0$	600	3	600	0.5
8.10	18^2, 18	0.185	$0.0 - 3.0$	300	3	2500	0.12
10.80	24^2, 24	0.185	$0.0 - 3.0$	500	2	6000	0.05

Table D.2.: Parameter overview of executed simulations for section 4.1.3.

λ	β in κ^{-1}	N_c, N_t	m_s in κ	μ-range in κ	no. up.	m. freq.	step n.	stepsize
0.1	5.40	12^2, 12	0.185	$0.0 - 3.0$	300	3	300	1.0
0.1	5.40	12^2, 24	0.185	$0.0 - 3.0$	300	3	600	0.5
0.1	5.40	12^2, 36	0.185	$0.0 - 3.0$	300	3	600	0.5
0.1	5.40	12^2, 48	0.185	$0.0 - 3.0$	300	3	600	0.5
0.1	5.40	12^2, 60	0.185	$0.0 - 3.0$	300	3	600	0.5
0.1	5.40	12^2, 72	0.185	$0.0 - 3.0$	300	3	600	0.5
0.4	5.40	12^2, 12	0.185	$0.0 - 3.0$	300	3	300	1.0
0.4	5.40	12^2, 24	0.185	$0.0 - 3.0$	300	3	1000	0.3
0.4	5.40	12^2, 36	0.185	$0.0 - 3.0$	300	3	1000	0.3
0.4	5.40	12^2, 48	0.185	$0.0 - 3.0$	300	3	1000	0.3
0.4	5.40	12^2, 60	0.185	$0.0 - 3.0$	300	3	1000	0.3
0.4	5.40	12^2, 72	0.185	$0.0 - 3.0$	300	3	1000	0.3
0.8	5.40	12^2, 12	0.185	$0.0 - 3.0$	300	3	300	1.0
0.8	5.40	12^2, 24	0.185	$0.0 - 3.0$	300	3	1000	0.3
0.8	5.40	12^2, 36	0.185	$0.0 - 3.0$	300	3	1000	0.3
0.8	5.40	12^2, 48	0.185	$0.0 - 3.0$	300	3	3000	0.1
0.8	5.40	12^2, 60	0.185	$0.0 - 3.0$	300	3	3000	0.1
0.8	5.40	12^2, 72	0.185	$0.0 - 3.0$	300	3	3000	0.1
0.8	5.40	12^2, 96	0.185	$0.0 - 3.0$	300	3	6000	0.05
1.0	5.40	12^2, 12	0.185	$0.0 - 3.0$	600	2	600	0.5
1.0	5.40	12^2, 24	0.185	$0.0 - 3.0$	300	3	1000	0.3
1.0	5.40	12^2, 36	0.185	$0.0 - 3.0$	300	3	1000	0.3
1.0	5.40	12^2, 48	0.185	$0.0 - 3.0$	300	3	3000	0.1
1.0	5.40	12^2, 60	0.185	$0.0 - 3.0$	300	3	3000	0.1
1.0	5.40	12^2, 72	0.185	$0.0 - 3.0$	300	3	6000	0.05
1.0	5.40	12^2, 96	0.185	$0.0 - 3.0$	300	3	10000	0.03

Table D.3.: Parameter overview of executed simulations for section 4.1.2 and 4.1.4.

β in κ^{-1}	N_c, N_t	m_s in κ	μ-range in κ	no. up.	m. freq.	step n.	stepsize
2.70	12^2, 6	0.185	$0.74 - 1.15$	400	2	1000	0.3
4.05	12^2, 9	0.185	$0.74 - 1.15$	400	2	1000	0.3
5.40	12^2, 12	0.185	$0.74 - 1.15$	1200	2	750	0.4
6.75	16^2, 15	0.185	$0.74 - 1.15$	400	2	1500	0.2
8.10	18^2, 19	0.185	$0.74 - 1.15$	400	2	3000	0.1
9.45	24^2, 21	0.185	$0.74 - 1.15$	400	2	8000	0.0375
10.80	24^2, 24	0.185	$0.74 - 1.15$	500	2	5000	0.06
12.15	30^2, 27	0.185	$0.74 - 1.15$	400	2	15000	0.02
10.80	30^2, 30	0.185	$0.74 - 1.15$	400	2	15000	0.02

Table D.4.: Parameter overview of executed simulations for section 4.2. Here the volumes were chosen in a way that the Susceptibility has reached the infinite volume limit.

β in κ^{-1}	N_c, N_t	m_s in κ	μ-range in κ	no. up.	m. freq.	step n.	stepsize
5.40	9^2, 24	$0.185\,\kappa$	$0.74 - 1.15$	300	3	3000	0.1
5.40	10^2, 24	$0.185\,\kappa$	$0.74 - 1.15$	300	3	3000	0.1
5.40	11^2, 24	$0.185\,\kappa$	$0.74 - 1.15$	300	3	3000	0.1
5.40	12^2, 24	$0.185\,\kappa$	$0.74 - 1.15$	300	3	3000	0.1
5.40	13^2, 24	$0.185\,\kappa$	$0.74 - 1.15$	300	3	3000	0.1
5.40	14^2, 24	$0.185\,\kappa$	$0.74 - 1.15$	300	3	3000	0.1
6.75	12^2, 27	$0.185\,\kappa$	$0.74 - 1.15$	300	3	7500	0.04
6.75	13^2, 27	$0.185\,\kappa$	$0.74 - 1.15$	300	3	7500	0.04
13.50	13^2, 30	$0.185\,\kappa$	$0.74 - 1.15$	300	3	10000	0.03
13.50	14^2, 30	$0.185\,\kappa$	$0.74 - 1.15$	300	3	10000	0.05
14.85	11^2, 33	$0.185\,\kappa$	$0.77 - 1.11$	300	3	10000	0.03
14.85	12^2, 33	$0.185\,\kappa$	$0.77 - 1.11$	300	3	10000	0.03
16.20	12^2, 36	$0.185\,\kappa$	$0.74 - 1.26$	200	2	10000	0.03
16.20	13^2, 36	$0.185\,\kappa$	$0.74 - 1.26$	200	2	10000	0.03

Table D.5.: Parameter overview of executed simulations for section 4.2. Here are all sets of parameters of executed simulation shown. In the analysis only the volumes in section 4.2 mentioned were used.

E. Simulation parameters - LLR-framework

Here we list the sets of parameters which were used for simulations in context of LLR method. Besides the physical and relevant HMC parameters we additionally list the necessary LLR-parameters in separate Tables. The relevant HMC parameters are step number and step size. For LLR we show the number of supporting points in one period N_s, the width of the window δ_s, the number of independent a_{j_cut}per supporting point N_a, the length of one a_j-series j_{cut}, the number of a_j-thermalization steps j_term, the number of HMC updates done after updating a_j (re-term.), the number of measurements contributing in the estimation of one a_j and the measure frequency of them. The parameters for simulations dealing with different staggered mass is shown in Tables E.1 and E.2, for different lattice discretizations in Tables E.3 and E.4 and for different on-site potential and volume in Tables E.5 and E.6

β in κ^{-1}	N_c, N_t	m_s in κ	U in κ	step n.	stepsize
2.70	6^2, 6	0.185	0.1	20	0.3
2.70	6^2, 6	0.111	0.1	30	0.2
2.70	6^2, 6	0.037	0.1	60	0.1

Table E.1.: Overview of physical and HMC parameters for executed simulations for section 5.2.1. The corresponding LLR parameters can be found in Table E.2.

m_s in κ	N_s	δ_s	N_a	j_{cut}	j_{term}	re-term.	N_{tev}	meas freq
0.185	63	0.1	10	90	30	20	10	10
0.111	63	0.1	10	90	30	20	10	10
0.037	63	0.1	10	90	30	20	10	10

Table E.2.: Overview of LLR parameters for executed simulations for section 5.2.1. The corresponding physical and HMC parameters can be found in Table E.1.

β in κ^{-1}	N_c, N_t	m_s in κ	U in κ	step n.	stepsize
2.70	6^2, 6	0.185	0.1	8	0.6
2.70	6^2, 12	0.185	0.1	10	0.5
2.70	6^2, 18	0.185	0.1	10	0.5

Table E.3.: Overview of physical and HMC parameters for executed simulations for section 5.2.2. The corresponding LLR parameters can be found in Table E.4.

.

m_s in κ	N_s	δ_s	N_a	j_{cut}	j_{term}	re-term.	N_{tev}	meas freq
6	120	0.1046	15	80	10	20	7	4
12	120	0.1046	15	80	10	20	7	4
18	120	0.1046	15	80	10	20	7	4

Table E.4.: Overview of LLR parameters for executed simulations for section 5.2.2. The corresponding physical and HMC parameters can be found in Table E.3.

β in κ^{-1}	N_c, N_t	m_s in κ	U in κ	step n.	stepsize
2.70	6^2, 6	0.185	0.1	5	0.4
2.70	6^2, 6	0.185	0.2	5	0.4
2.70	6^2, 6	0.185	0.3	5	0.4
2.70	6^2, 6	0.185	1.0	5	0.4
2.70	6^2, 6	0.185	2.0	6	0.3
2.70	12^2, 12	0.185	1.0	5	0.4
2.70	12^2, 12	0.185	2.0	6	0.3

Table E.5.: Overview of physical and HMC parameters for executed simulations for section 5.2.3. The corresponding LLR parameters can be found in Table E.6.

N_c	U in κ	N_s	δ_s	N_a	j_{cut}	j_{term}	re-term.	N_{tev}	meas freq
6^2	0.1	210	0.2	20	105	15	15	7	7
6^2	0.2	210	0.2	20	105	15	20	7	7
6^2	0.3	210	0.2	20	105	15	20	7	7
6^2	1.0	210	0.2	20	105	15	20	7	7
6^2	2.0	210	0.2	20	105	15	20	7	7
12^2	1.0	144	0.3	20	105	15	20	7	7
12^2	2.0	144	0.3	20	105	15	20	7	7

Table E.6.: Overview of LLR parameters for executed simulations for section 5.2.3. The corresponding physical and HMC-parameters can be found in Table E.5.

F. Soft- and Hardware

The Hybrid-Monte-Carlo code was written in C++ and CUDA and the simulations were done on a group intern GPU-Cluster equipped with nvidia chipsets according to Table F.1. The plots and parts of data evaluation was done with Mathematica 10 - 12. Codes for data evaluation were written in Phyton and Bash.

Chipset	GTX 680	GTX 780	GTX Titan	GTX 980 ti	RTX 2080
CUDA Cores	1536	2304	2688	2816	2944
Base Clock (MHz)	1006	863	837	1075	1710
Memory Speed Gb/s	6.0	6.0	6.0	7.9	14.0
Memory GB	2	3	6	6	8
Bandwidth GB/s	192	288	288	336	448

Table F.1.: Specifications of used GPUs [125].

Bibliography

[1] D. Smith, M. Körner, and L. Von Smekal. On the semimetal-insulator transition and lifshitztransition in simulations of mono-layer graphene. *PoS LATTICE2014*, 055, 2014.

[2] M. Körner. Investigation of topological phase transitions in Graphene by Monte-Carlo Simulations. Master's thesis, TU Darmstadt, August 2015.

[3] M. Körner, D. Smith, P. Buividovich, M. Ulybyshev, and L. Von Smekal. A hybrid-monte-carlo study of monolayer graphene with partially screened coulomb interactions at finite spin density. *Physical Review B*, 96, 04 2017.

[4] Dominik Smith, Pavel Buividovich, Michael Körner, Maksim Ulybyshev, and Lorenz von Smekal. Quantum phase transitions on the hexagonal lattice, 2019.

[5] Michael Körner, Kurt Langfeld, Dominik Smith, and Lorenz von Smekal. A density of states approach to the hexagonal hubbard model at finite density, 2020.

[6] K. S. Novoselov, A. K. Geim, S. V. Morozov, D. Jiang, Y. Zhang, S. V. Dubonos, I. V. Grigorieva, and A. A. Firsov. Electric field effect in atomically thin carbon films. *Science*, 306:666–669, 2004.

[7] H. P. Boehm, A. Clauss, G. O. Fischer, and U. Hofmann. Dünnste kohlenstoff-folien. *Z. Naturforschg.*, 17 b:150 – 153, 1962.

[8] L. D. Landau. Zur Theorie der Phasenumwandlungen II. *Phys. Z. Sowjetunion*, 11:26–35, 1937.

[9] R. E. Peierls. Quelques proprietes typiques des corpses solides. *Ann. I. H. Poincare*, 5:177–222, 1935.

[10] N. D. Mermin. Crystalline Order in Two Dimensions. *Physical Review*, 176:250–254, December 1968.

[11] A. K. Geim and K. S. Novoselov. The rise of graphene. *Nature materials*, 6:183–191, 2007.

[12] Daniel R. Cooper, Benjamin D'Anjou, Nageswara Ghattamaneni, Benjamin Harack, Michael Hilke, Alexandre Horth, Norberto Majlis, Mathieu Massicotte, Leron Vandsburger, Eric Whiteway, and Victor Yu. Experimental review of graphene, 2011.

[13] Matthew J. Allen, Vincent C. Tung, and Richard B. Kaner. Honeycomb carbon: A review of graphene. *Chemical Reviews*, 110(1):132–145, 2010. PMID: 19610631.

[14] A. K. Geim and I. V. Grigorieva. Van der waals heterostructures. *Nature*, 499, 07 2013.

[15] A. H. Castro Neto, F. Guinea, N. M. R. Peres, K. S. Novoselov, and A. K. Geim. The electronic properties of graphene. *Reviews of modern Physics*, 81:110–162, 2009.

[16] V. N. Kotov, B. Uchoa, V. M. Pereira, F. Guinea, and A. H. Castro Neto. Electron-electron interactions in graphene: Current status and perspectives. *Rev. Mod. Phys.*, 84:1067–1125, Jul 2012.

[17] A. S. Mayorov, D. C. Elias, I. S. Mukhin, S. V. Morozov, L. A. Ponomarenko, K. S. Novoselov, A. K. Geim, and R. V. Gorbachev. How close can one approach the dirac point in graphene experimentally? *Nano Lett.*, 12:4629–4634, Aug 2012.

[18] Y.-W. Tan, Y. Zhang, K. Bolotin, Y. Zhao, S. Adam, E. H. Hwang, S. Das Sarma, H. L. Stormer, and P. Kim. Measurement of scattering rate and minimum conductivity in graphene. *Phys. Rev. Lett.*, 99:246803, Dec 2007.

[19] D. C. Elias, R. V. Gorbachev, A. S. Mayorov, S. V. Morozov, A. A. Zhukov, P. Blake, L. A. Ponomarenko, I. V. Grigorieva, K. S. Novoselov, F. Guinea, and A. K. Geim. Dirac cones reshaped by interaction effects in suspended graphene. *Nature Physics*, 7:701–704, July 2011.

[20] D. Smith and L. von Smekal. Monte carlo simulation of the tight-binding model of graphene with partially screened coulomb interactions. *Phys. Rev. B*, 89:195429, May 2014.

[21] M.V. Ulybyshev, P. V. Buividovich, M. I. Katsnelson, F. Guinea, and M. I. Polikarpov. Monte-carlo study of the semimetal-insulator phase transition in monolayer graphene with realistic inter-electron interaction potential. *Phys. Rev. Lett.*, 111:056801, 2013.

[22] Fakher F. Assaad and Igor F. Herbut. Pinning the order: The nature of quantum criticality in the hubbard model on honeycomb lattice. *Phys. Rev. X*, 3:031010, Aug 2013.

[23] Francesco Parisen Toldin, Martin Hohenadler, Fakher F. Assaad, and Igor F. Herbut. Fermionic quantum criticality in honeycomb and π-flux hubbard models: Finite-size scaling of renormalization-group-invariant observables from quantum monte carlo. *Phys. Rev. B*, 91:165108, Apr 2015.

[24] Katja Kleeberg. *Dyson-Schwinger equations for strongly interacting Fermions on the Hexagonal Graphene lattice*. PhD thesis, Justus-Liebig-Universität, 2019.

[25] Alexander A. Balandin, Suchismita Ghosh, Wenzhong Bao, Irene Calizo, Desalegne Teweldebrhan, Feng Miao, and Chun Ning Lau. Superior thermal conductivity of single-layer graphene. *Nano Letters*, 8(3):902–907, 2008. PMID: 18284217.

[26] Shanshan Chen, Arden L. Moore, Weiwei Cai, Ji Won Suk, Jinho An, Columbia Mishra, Charles Amos, Carl W. Magnuson, Junyong Kang, Li Shi, and Rodney S. Ruoff. Raman measurements of thermal transport in suspended monolayer graphene of variable sizes in vacuum and gaseous environments. *ACS Nano*, 5(1):321–328, 2011. PMID: 21162551.

[27] A. K. Geim. Graphene: Status and prospects. *Science*, 324(5934):1530–1534, 2009.

[28] Changgu Lee, Xiaoding Wei, Jeffrey W. Kysar, and James Hone. Measurement of the elastic properties and intrinsic strength of monolayer graphene. *Science*, 321(5887):385–388, 2008.

[29] K. S. Novoselov, Z. Jiang, Y. Zhang, S. V. Morozov, H. L. Stormer, U. Zeitler, J. C. Maan, G. S. Boebinger, P. Kim, and A. K. Geim. Room-temperature quantum hall effect in graphene. *Science*, 315(5817):1379–1379, 2007.

[30] J. Chapman, Y. Su, C. A. Howard, D. Kundys, A. N. Grigorenko, F. Guinea, A. K. Geim, I. V. Grigorieva, and R. R. Nair. Superconductivity in ca-doped graphene laminates. *Scientific Reports*, 6, 03 2016.

[31] T. Foley, R. Waters, F. Gomollón-Bel, and L. Diamante. Graphene flagship annual report 2019. Technical report, Graphene Flagship, 2019.

[32] Azlan Hamzah, Reena Sri Selvarajan, and Burhanuddin Majlis. Graphene for biomedical applications: A review. *Sains Malaysiana*, 46:1125–1139, 07 2017.

[33] P. R. Wallace. The band theory of graphite. *Phys. Rev.*, 71:622–634, 1947.

[34] K. S. Novoselov, A. K. Geim, S. V. Morozov, D. Jiang, Katsnelson M. I., I. V. Grigorieva, S. V. Dubonos, and A. A. Firsov. Two-dimensional gas of massless dirac fermions in graphene. *Nature*, 438, 11 2005.

[35] V. P. Gusynin, S. G. Sharapov, and J. P. Carbotte. Ac conductivity of graphene: From tight-binding model to 2 + 1-dimensional quantum electrodynamics. *International Journal of Modern Physics B*, 21(27):4611–4658, 2007.

[36] Y. Zhang, Y.-W. Tan, H. L. Stormer, and P. Kim. Experimental observation of the quantum hall effect and berry's phase in graphene. *Nature*, 438, 11 2005.

[37] C. L. Kane and E. J. Mele. Quantum spin hall effect in graphene. *Phys. Rev. Lett.*, 95:226801, Nov 2005.

[38] Csaba Toke, Paul Lammert, Jainendra Jain, and Vincent Crespi. Fractional quantum hall effect in graphene. *Physical Review B*, 74, 06 2006.

[39] Y. Liu, G. Bian, T. Miller, and T.-C. Chiang. Visualizing electronic chirality and berry phases in graphene systems using photoemission with circularly polarized light. *Phys. Rev. Lett.*, 107:166803, Oct 2011.

[40] M.I. Katsnelson and K.S. Novoselov. Graphene: New bridge between condensed matter physics and quantum electrodynamics. *Solid State Communications*, 143(1):3 – 13, 2007. Exploring graphene.

[41] J. L. McChesney, Aaron Bostwick, Taisuke Ohta, Thomas Seyller, Karsten Horn, J. González, and Eli Rotenberg. Extended van hove singularity and superconducting instability in doped graphene. *Phys. Rev. Lett.*, 104:136803, Apr 2010.

[42] J. González. Kohn-luttinger superconductivity in graphene. *Phys. Rev. B*, 78:205431, Nov 2008.

[43] Maximilian L. Kiesel, Christian Platt, Werner Hanke, Dmitry A. Abanin, and Ronny Thomale. Competing many-body instabilities and unconventional superconductivity in graphene. *Phys. Rev. B*, 86:020507, Jul 2012.

[44] M.Yu. Kagan, V.V. Valkov, V.A. Mitskan, and M.M. Korovushkin. The kohn–luttinger superconductivity in idealized doped graphene. *Solid State Communications*, 188:61 – 66, 2014.

[45] R Nandkishore, L. S. Levitov, and A. V. Chubukov. Chiral superconductivity from repulsive interactions in doped graphene. *Nature Physics*, 8:158 – 163, Feb 2012.

[46] R.S Markiewicz. A survey of the van hove scenario for high-tc superconductivity with special emphasis on pseudogaps and striped phases. *Journal of Physics and Chemistry of Solids*, 58(8):1179 – 1310, 1997.

[47] C. Popovici, C.S. Fischer, and L. von Smekal. Effects of electron-electron interactions in suspended graphene. *PoS*, ConfinementX:269, 2012.

[48] C. Popovici, C. S. Fischer, and L. von Smekal. Fermi velocity renormalization and dynamical gap generation in graphene. *Phys. Rev. B*, 88:205429, Nov 2013.

[49] M. E. Carrington, C. S. Fischer, L. von Smekal, and M. H. Thoma. Dynamical gap generation in graphene with frequency-dependent renormalization effects. *Phys. Rev. B*, 94:125102, Sep 2016.

[50] M. E. Carrington, C. S. Fischer, L. von Smekal, and M. H. Thoma. Role of frequency dependence in dynamical gap generation in graphene. *Phys. Rev. B*, 97:115411, Mar 2018.

[51] M. E. Carrington. Effect of a chern-simons term on dynamical gap generation in graphene. *Phys. Rev. B*, 99:115432, Mar 2019.

[52] J. González, F. Guinea, and M.A.H. Vozmediano. Non-fermi liquid behavior of electrons in the half-filled honeycomb lattice (a renormalization group approach). *Nuclear Physics B*, 424(3):595 – 618, 1994.

[53] Lukas Janssen and Igor F. Herbut. Antiferromagnetic critical point on graphene's honeycomb lattice: A functional renormalization group approach. *Phys. Rev. B*, 89:205403, May 2014.

[54] Laura Classen, Igor F. Herbut, Lukas Janssen, and Michael M. Scherer. Competition of density waves and quantum multicritical behavior in dirac materials from functional renormalization. *Phys. Rev. B*, 93:125119, Mar 2016.

[55] R. Blankenbecler, D. J. Scalapino, and R. L. Sugar. Monte carlo calculations of coupled boson-fermion systems. i. *Phys. Rev. D*, 24:2278–2286, Oct 1981.

[56] S. R. White, D. J. Scalapino, R. L. Sugar, E. Y. Loh, J. E. Gubernatis, and R. T. Scalettar. Numerical study of the two-dimensional hubbard model. *Phys. Rev. B*, 40:506–516, Jul 1989.

[57] Yuichi Otsuka, Seiji Yunoki, and Sandro Sorella. Universal quantum criticality in the metal-insulator transition of two-dimensional interacting dirac electrons. *Phys. Rev. X*, 6:011029, Mar 2016.

[58] Pavel Buividovich, Dominik Smith, Maksim Ulybyshev, and Lorenz von Smekal. Hybrid monte carlo study of competing order in the extended fermionic hubbard model on the hexagonal lattice. *Phys. Rev. B*, 98:235129, Dec 2018.

[59] P. Buividovich, D. Smith, M. Ulybyshev, and L. von Smekal. Numerical evidence of conformal phase transition in graphene with long-range interactions. *Phys. Rev. B*, 99:205434, May 2019.

[60] Stefan Beyl, Florian Goth, and Fakher F. Assaad. Revisiting the hybrid quantum monte carlo method for hubbard and electron-phonon models. *Phys. Rev. B*, 97:085144, Feb 2018.

[61] Stefan Krieg, Thomas Luu, Johann Ostmeyer, Philippos Papaphilippou, and Carsten Urbach. Accelerating hybrid monte carlo simulations of the hubbard model on the hexagonal lattice. *Computer Physics Communications*, 236:15 – 25, 2019.

[62] E. Y. Loh, J. E. Gubernatis, R. T. Scalettar, S. R. White, D. J. Scalapino, and R. L. Sugar. Sign problem in the numerical simulation of many-electron systems. *Phys. Rev. B*, 41:9301–9307, May 1990.

[63] Matthias Troyer and Uwe-Jens Wiese. Computational complexity and fundamental limitations to fermionic quantum monte carlo simulations. *Phys. Rev. Lett.*, 94:170201, May 2005.

[64] K. Langfeld, B. Lucini, and A. Rago. The density of states in gauge theories. *Phys. Rev. Lett.*, 109:111601, 2012.

[65] F. Wang and D. P. Landau. Efficient, multiple-range random walk algorithm to calculate the density of states. *Phys. Rev. Lett.*, 86:2050–2053, Mar 2001.

[66] K. Langfeld and J. M. Pawlowski. Two-color QCD with heavy quarks at finite densities. *Phys. Rev.*, D88(7):071502, 2013.

[67] K. Langfeld and B. Lucini. Density of states approach to dense quantum systems. *Phys. Rev.*, D90(9):094502, 2014.

[68] K. Langfeld, B. Lucini, R. Pellegrini, and A. Rago. An efficient algorithm for numerical computations of continuous densities of states. *Eur. Phys. J.*, C76(6):306, 2016.

[69] C. Gattringer and K. Langfeld. Approaches to the sign problem in lattice field theory. *Int. J. Mod. Phys.*, A31(22):1643007, 2016.

[70] N. Garron and K. Langfeld. Anatomy of the sign-problem in heavy-dense QCD. *Eur. Phys. J.*, C76(10):569, 2016.

[71] K. Langfeld. Density-of-states. *PoS Lattice2016*, page 010, 2017.

[72] N. Garron and K. Langfeld. Controlling the Sign Problem in Finite Density Quantum Field Theory. *Eur. Phys. J.*, C77(7):470, 2017.

[73] M. I. Katsnelson. *Graphene - Carbon in two dimensions.* Cambridge University Press, 2012.

[74] S. Reich, J. Maultzsch, C. Thomsen, and P. Ordejón. Tight-binding description of graphene. *Phys. Rev. B*, 66:035412, Jul 2002.

[75] J. P. Hobson and W. A. Nierenberg. The statistics of a two-dimensional, hexagonal net. *Phys. Rev.*, 89:662–662, Feb 1953.

[76] I. M. Lifshitz. Anomalies of electron characteristics of a metal in the high pressure region. *Sov. Phys. JETP*, 11:1130, Nov 1960.

[77] M. R. Norman, Jie Lin, and A. J. Millis. Lifshitz transition in underdoped cuprates. *Phys. Rev. B*, 81:180513, May 2010.

[78] N. Xu, P. Richard, X. Shi, A. van Roekeghem, T. Qian, E. Razzoli, E. Rienks, G.-F. Chen, E. Ieki, K. Nakayama, T. Sato, T. Takahashi, M. Shi, and H. Ding. Possible nodal superconducting gap and lifshitz transition in heavily hole-doped $\mathrm{ba}_{0.1}\mathrm{k}_{0.9}\mathrm{fe}_2\mathrm{as}_2$. *Phys. Rev. B*, 88:220508, Dec 2013.

[79] S. N. Khan and D. D. Johnson. Lifshitz transition and chemical instabilities in $\mathrm{ba}_{1-x}\mathrm{k}_x\mathrm{fe}_2\mathrm{as}_2$ superconductors. *Phys. Rev. Lett.*, 112:156401, Apr 2014.

[80] Y. Wang, Z-Q Han, X. Peng, P. Richard, T. Qian, X. Wu, M-W Qiu, S. C. Wang, J. Hu, Y-J Sun, and H. Ding. Enhanced superconductivity accompanying a lifshitz transition in electron-doped fese monolayer. *Nature Communications*, 8, Jun 2016.

[81] Z. J. Xiang, G. J. Ye, C. Shang, B. Lei, N. Z. Wang, K. S. Yang, D. Y. Liu, F. B. Meng, X. G. Luo, L. J. Zou, Z. Sun, Y. Zhang, and X. H. Chen. Pressure-induced electronic transition in black phosphorus. *Phys. Rev. Lett.*, 115:186403, Oct 2015.

[82] Y. Lemonik, I. L. Aleiner, C. Toke, and V. I. Fal'ko. Spontaneous symmetry breaking and lifshitz transition in bilayer graphene. *Phys. Rev. B*, 82:201408, Nov 2010.

[83] D. A. Gradinar, H. Schomerus, and V. I. Fal'ko. Conductance anomaly near the lifshitz transition in strained bilayer graphene. *Phys. Rev. B*, 85:165429, Apr 2012.

[84] Y.M. Blanter, M.I. Kaganov, A.V. Pantsulaya, and A.A. Varlamov. The theory of electronic topological transitions. *Physics Reports*, 245(4):159 – 257, 1994.

[85] B. Dietz, F. Iachello, M. Miski-Oglu, N. Pietralla, A. Richter, L. von Smekal, and J. Wambach. Lifshitz and excited-state quantum phase transitions in microwave dirac billiards. *Phys. Rev. B*, 88:104101, Sep 2013.

[86] R. Brower, C. Rebbi, and D. Schaich. Hybrid monte carlo simulation on the graphene hexagonal lattice. *PoS LATTICE 2011*, 056, 2012.

[87] J. W. Negele and H. Orland. *Quantum Many-Particle Systems*. Westview Press, 1998.

[88] C.B. Gattringer, C. Lang. *Quantum Chromodynamics on the Lattice: An Introductory Presentation*. Springer, 2010.

[89] D. Smith and L. von Smekal. Hybrid monte-carlo simulation of interacting tight-binding model of graphene. *PoS LATTICE 2013*, 048, 2013.

[90] J. Hubbard. Electron correlations in narrow energy bands. *Proc. R. Soc. Lond. A*, 276, Nov 1963.

[91] Junjiro Kanamori. Electron Correlation and Ferromagnetism of Transition Metals. *Progress of Theoretical Physics*, 30(3):275–289, 09 1963.

[92] Martin C. Gutzwiller. Effect of correlation on the ferromagnetism of transition metals. *Phys. Rev. Lett.*, 10:159–162, Mar 1963.

[93] Editorial. The hubbard model at half a century. *Nature Physics*, 9, Sep 2013.

[94] S. Sorella, Y. Otsuka, and S. Yunoki. Absence of a spin liquid phase in the hubbard model on the honeycomb lattice. *Scientific Reports*, 2, Dec 2012.

[95] Igor F. Herbut, Vladimir Juričić, and Oskar Vafek. Relativistic mott criticality in graphene. *Phys. Rev. B*, 80:075432, Aug 2009.

[96] Bitan Roy. Multicritical behavior of $\digamma_2 \times o(2)$ gross-neveu-yukawa theory in graphene. *Phys. Rev. B*, 84:113404, Sep 2011.

[97] M. Hohenadler, F. Parisen Toldin, I. F. Herbut, and F. F. Assaad. Phase diagram of the kane-mele-coulomb model. *Phys. Rev. B*, 90:085146, Aug 2014.

[98] Laura Classen, Igor F. Herbut, Lukas Janssen, and Michael M. Scherer. Competition of density waves and quantum multicritical behavior in dirac materials from functional renormalization. *Phys. Rev. B*, 93:125119, Mar 2016.

[99] T. O. Wehling, A. I. Lichtenstein, and M. I. Katsnelson. Transition-metal adatoms on graphene: Influence of local coulomb interactions on chemical bonding and magnetic moments. *Phys. Rev. B*, 84:235110, Dec 2011.

[100] E. V. Gorbar, V. P. Gusynin, V. A. Miransky, and I. A. Shovkovy. Magnetic field driven metal-insulator phase transition in planar systems. *Phys. Rev. B*, 66:045108, Jul 2002.

[101] Igor F. Herbut. Interactions and phase transitions on graphene's honeycomb lattice. *Phys. Rev. Lett.*, 97:146401, Oct 2006.

[102] Vladimir Juričić, Igor F. Herbut, and Gordon W. Semenoff. Coulomb interaction at the metal-insulator critical point in graphene. *Phys. Rev. B*, 80:081405, Aug 2009.

[103] Kurt Langfeld. Private communications. University of Liverpool, 2018.

[104] Emmanuel J. Candès, Justin K. Romberg, and Terence Tao. Stable signal recovery from incomplete and inaccurate measurements. *Communications on Pure and Applied Mathematics*, 59(8):1207–1223, 2006.

[105] Simon Duane, A.D. Kennedy, Brian J. Pendleton, and Duncan Roweth. Hybrid monte carlo. *Physics Letters B*, 195(2):216 – 222, 1987.

[106] Thomas Luu and Timo A. Lähde. Quantum monte carlo calculations for carbon nanotubes. *Phys. Rev. B*, 93:155106, Apr 2016.

[107] Bernd A. Berg. *Markov Chain Monte Carlo Simulations and their Statistical Analysis*. World Scientific Publishing Co. Pte. Ltd., 2004.

[108] W.H. Press, S. A. Teukolsky, W. T. Vetterling, and B. P. Flannery. *Numerical Recipes - The Art of Scientific Computing*. Cambridge University Press, 3 edition, 2007.

[109] J. R. Shewchuck. An introduction to the conjugate gradient method without the agonizing pain. Technical report, Carnegie Mellon University, 1994. https://www.cs.cmu.edu/ quake-papers/painless-conjugate-gradient.pdf.

[110] N. Metropolis, A. W. Rosenbluth, M. N. Rosenbluth, A. H. Teller, and E. Teller. Equation of state calculations by fast computing machines. *Journal of Chemical Physics*, 21(6):1087 – 1092, 1953.

[111] R. T. Scalettar, D. J. Scalapino, R. L. Sugar, and D. Toussaint. Hybrid molecular-dynamics algorithm for the numerical simulation of many-electron systems. *Phys. Rev. B*, 36:8632–8641, Dec 1987.

[112] Steven R. White and John W. Wilkins. Fermion simulations in systems with negative weights. *Phys. Rev. B*, 37:5024–5031, Apr 1988.

[113] Jan-Lukas Wynen, Evan Berkowitz, Christopher Körber, Timo A. Lähde, and Thomas Luu. Avoiding ergodicity problems in lattice discretizations of the hubbard model. *Phys. Rev. B*, 100:075141, Aug 2019.

[114] Marco Cristoforetti, Francesco Di Renzo, and Luigi Scorzato. New approach to the sign problem in quantum field theories: High density qcd on a lefschetz thimble. *Phys. Rev. D*, 86:074506, Oct 2012.

[115] Marco Cristoforetti, Francesco Di Renzo, Abhishek Mukherjee, and Luigi Scorzato. Monte carlo simulations on the lefschetz thimble: Taming the sign problem. *Phys. Rev. D*, 88:051501, Sep 2013.

[116] Andrei Alexandru, Gök çe Başar, and Paulo Bedaque. Monte carlo algorithm for simulating fermions on lefschetz thimbles. *Phys. Rev. D*, 93:014504, Jan 2016.

[117] A. Bazavov, H.-T. Ding, P. Hegde, O. Kaczmarek, F. Karsch, E. Laermann, Y. Maezawa, Swagato Mukherjee, H. Ohno, P. Petreczky, H. Sandmeyer, P. Steinbrecher, C. Schmidt, S. Sharma, W. Soeldner, and M. Wagner. Qcd equation of state to $\mathcal{O}(\mu_B^6)$ from lattice qcd. *Phys. Rev. D*, 95:054504, Mar 2017.

[118] Herbert Robbins and Sutton Monro. A stochastic approximation method. *Ann. Math. Statist.*, 22(3):400–407, 09 1951.

[119] B. Efron. Bootstrap methods: Another look at the jackknife. *Ann. Statist.*, 7(1):1–26, 01 1979.

[120] Søren Ulstrup, Malte Schüler, Marco Bianchi, Felix Fromm, Christian Raidel, Thomas Seyller, Tim Wehling, and Philip Hofmann. Manifestation of nonlocal electron-electron interaction in graphene. *Phys. Rev. B*, 94:081403, Aug 2016.

[121] Lorenz von Smekal. Private communications. Justus Liebig Universität Gießen, 2019.

[122] Kurt Langfeld. Private communications. University of Liverpool, 2019.

[123] Aaron Bostwick, Taisuke Ohta, Jessica L McChesney, Konstantin V Emtsev, Thomas Seyller, Karsten Horn, and Eli Rotenberg. Symmetry breaking in few layer graphene films. *New Journal of Physics*, 9(10):385–385, Oct 2007.

[124] M. V. Ulybyshev and S. N. Valgushev. Path integral representation for the hubbard model with reduced number of lefschetz thimbles, 2017.

[125] Nvidia-Corporation. Geforce chipset specifications. http://www.nvidia.de. 11.05.2020.

Danksagung

An dieser Stelle möchte ich mich zunächst bei Prof. Lorenz von Smekal, der mir die Möglichkeit eröffnete an diesem Projekt zu arbeiten und sich dabei stets für Fragen, Diskussionen und Wünsche meinerseits Zeit nahm, bedanken. Mein Dank gilt ebenfalls Prof. Kurt Langfeld für regelmäßige gute Gespräche im Kontext der LLR Methode und die produktive und lehrreiche Zeit die ich auf seine Einladung hin in Liverpool hatte. Prof. Christian Fischer möchte ich für die Übernahme des Zweitgutachtens danken. Darüber hinaus danke ich Dominik Smith für das Korrekturlesen der Arbeit und die jahrelange gute Zusammenarbeit sowie die angenehme Atmosphäre in unserem gemeinsamen Büro. Ebenso danke ich Christopher Jung, Dominik Schweitzer, Katja Kleeberg, Lukas Holicki und Milad Ghanbarpour sowie den weiteren Kollegen für die vielen guten und erheiternden Gespräche bei Mittagessen, Tee- und Kaffeepausen.
Des Weiteren sollten hier meine Familie und meine Freunde erwähnt werden, die mich stets unterstützten und mir in den letzten Jahren immer wieder die Möglichkeit gaben auch mal auf andere Gedanken zu kommen. Besonders zu erwähnen sind hierbei Daniel Fecher, Daniel Scharf, Helge Schäfer, Jonas Müller und Thorsten Bitsch. Abschließend danke ich ganz besonders meiner Lebensgefährtin Elisabeth Rossellit für all die kleinen und großen Dinge mit denen sie mich stets ermutigt hat und mein Leben weiterhin bereichert.